Western Graduate&PostdoctoralStudies

Western University
Scholarship@Western

Electronic Thesis and Dissertation Repository

4-21-2023 1:45 PM

MODELLING CELL POPULATION GROWTH

Mahmood Mazarei, *The University of Western Ontario*

Supervisor: Karttunen, Mikko, *The University of Western Ontario*
A thesis submitted in partial fulfillment of the requirements for the Doctor of Philosophy degree in Physics
© Mahmood Mazarei 2023

Follow this and additional works at: https://ir.lib.uwo.ca/etd

Part of the Biological and Chemical Physics Commons, Condensed Matter Physics Commons, and the Statistical, Nonlinear, and Soft Matter Physics Commons

Recommended Citation

Mazarei, Mahmood, "MODELLING CELL POPULATION GROWTH" (2023). *Electronic Thesis and Dissertation Repository*. 9239.
https://ir.lib.uwo.ca/etd/9239

This Dissertation/Thesis is brought to you for free and open access by Scholarship@Western. It has been accepted for inclusion in Electronic Thesis and Dissertation Repository by an authorized administrator of Scholarship@Western. For more information, please contact wlswadmin@uwo.ca.

Abstract

The growth of biological matter, e.g., tumor invasion, depends on various factors, including the tissue's mechanical properties, implying elasticity, stiffness, or apparent viscosity. These properties are impacted by the characteristics of the tissue's extracellular matrix and constituent cells, including, but not limited to, cell membrane stiffness, cell cytoskeleton mechanical properties, and the intensity and distribution of focal adhesions over the cell membrane. To compute and study the mechanical properties of tissues during growth and confluency, a theoretical and computational framework, called *CellSim3D*, was developed in our group based on a three-dimensional kinetic division model.

In this work, *CellSim3D* is updated with a new set of cell mechanical parameters and force fields such as the asymmetric division rule, shape diversity, apoptosis process, and boundary conditions, e.g., periodic and Lees-Edwards boundary conditions. The package is upgraded to operate on multiple GPUs to further accelerate computations. This enables the inclusion of more complexity in the system. For instance, the simulation of macroscopic scale bicellular tissue growth with precise control over the mechanical properties of cells is now more feasible than before.

The effects of cell-cell adhesion strength and intermembrane friction on growth kinetics and interface roughness dynamics of epithelial tissue were studied. It is reported that with fine alterations of the mechanical parameters such as the cell-cell adhesion strength, one could reliably reproduce different interface roughness scaling behaviors such as Kardar–Parisi–Zhang (KPZ)-like and Molecular Beam Epitaxy (MBE)-like scaling. In addition, it was observed that substrate heterogeneity and geometry have significant impacts on the morphology and interface roughness scaling of epithelial tissue. The results suggest that the interface roughness scaling of epithelial tissues cannot be classified by any well-known scaling universality class. Instead, it strongly depends on several other factors, such as the cell-cell adhesion strength. This explains the controversies observed in earlier experimental works over the interface roughness scaling of expanding epithelial tissue.

Keywords: Mechanical cell modelling, Interface roughness scaling, Cell Population Dynamics, Epithelial Tissue Growth

Summary for Lay Audience

The development and progression of human diseases such as asthma and cancer depend on various factors, including the mechanical properties of the tissue or tumor. These mechanical properties are dependent on the mechanical properties of the cells that comprise the tissue and tissue substrate. Due to rapid advances in experimental techniques and computational capacity, the scientific community has made progress in modeling tissue growth and dynamics over the past few decades. *CellSim3D* is a theoretical and computational framework that models cells in three-dimensions with functional mechanical properties such as cell membrane stiffness and cell-cell adhesion in order to study tissue growth and dynamics. We upgraded *CellSim3D* to simulate tissue growth with new features such as cell shape diversity, the cell apoptosis process, and bicellular tissue growth. The current version of the software has also been upgraded to simulate tissue growth and dynamics with millions of cells. We used *CellSim3D* to study the impact of cell mechanical properties on tissue interface roughness. We showed that cell mechanical properties, such as cell-cell adhesion strength, have a substantial effect on the colonies' interface roughness, from a jagged to a smooth interface. In addition, we also demonstrated the extent to which substrate geometry and heterogeneity influence the interface roughness and morphology of cell tissues. These findings emphasize the important impact of parameters such as cell mechanical properties and substrate heterogeneity on the roughness of tissue interfaces, which also explains the differing interface roughness observed in the tissue growth experiments. Studying the interface roughness of biological substances can aid in disease diagnosis and prognosis. For example, tumors with a coarser surface are frequently more aggressive and susceptible to metastasis.

Acknowledgements

I would like to express my deep and sincere gratitude to my supervisor, Dr. Mikko Karttunen, for giving me the opportunity to conduct research under his supervision and providing invaluable guidance, encouragement, and support throughout my PhD. I really enjoyed working on my PhD with him because he is very pleasant to work with.

I appreciate my parents for their dedication to me when I was not in their presence as I pursued my goals in another country. I am deeply thankful that they supported my passion all along and inspired me to pursue my dreams. A special thanks to my beloved girlfriend, Chiara, for her heartwarming companionship and positive affirmations as I worked on my PhD. I would also like to express my gratitude to my brothers Mohammad Reza and Alireza, who motivated me to persevere in the face of challenges.

I would like to thank Dr. Jan Westerholm and Dr. Jan Åström who guided and supported me during and after my research visit to Finland.

Lastly, I would like to acknowledge Dr. Artem Glova, Steven Silber, Alireza Fazeli, Farshad Esmaelian, Sepideh Soltani, Michael Thompson, and Mohammad Noorchenarboo who read over my thesis and gave me constructive feedback. They kindly took the time to help me.

Co-Authorship Statement

This thesis contains the following manuscripts that have been published or submitted:

Chapter 4 has been published in Physical Review E.

> Mahmood Mazarei, Jan Åström, Jan Westerholm, and Mikko Karttunen. *In silico testing of the universality of epithelial tissue growth*. Physical Review E, 106, L062402, 2022.

Chapter 5 has been submitted to Physical Review E.

> Mahmood Mazarei, Jan Åström, Jan Westerholm, and Mikko Karttunen. *Effect of substrate heterogeneity and topology on epithelial tissue growth dynamics*. Physical Review E, EC12566, 2023, Submitted.

All authors conceived the research project and wrote the manuscript, and Mahmood Mazarei performed the simulations, data analysis and wrote the first versions of the manuscripts.

American Physical Society, the publisher of our article, allows for the inclusion of the published article within this thesis.

Contents

Abstract ii

Summary for Lay Audience iv

Acknowledgements v

Co-Authorship Statement vi

List of Figures xi

List of Tables xx

List of Abbreviations, Symbols, and Nomenclature xxiv

1 Introduction 1

1.1 Mechanical Cell Models 1

1.2 Epithelial Tissue Growth Dynamics 9

1.3 Thesis Outline 14

2 Surface Growth in Nature 15

2.1 Continuum Theory 17

2.1.1 Symmetry Principle 17

2.1.2 Kardar-Parisi-Zhang Equation 20

2.1.3 Quenched Kardar-Parisi-Zhang Equation 23

2.1.4 Molecular Beam Epitaxy Equation 25

2.2 Scaling Arguments 28
    2.2.1 Kardar-Parisi-Zhang Scaling 31
    2.2.2 Molecular Beam Epitaxy Scaling 32
2.3 Renormalization Group Method 33
    2.3.1 Dynamic Janssen–De Dominicis Response Functional 33
    2.3.2 Momentum Shell Renormalization Group 36
    2.3.3 Kardar-Parisi-Zhang Equation 41
    2.3.4 Molecular Beam Epitaxy Equation 43
2.4 Discrete Growth Models 45
    2.4.1 Ballistic Deposition 46
    2.4.2 Eden Model 47
    2.4.3 Irreversible Molecular Beam Epitaxy Growth Models 49
    2.4.4 Directed Percolation Depinning 50

3 Numerical Methods 52

3.1 CellSim3D Assumptions 53
3.2 Force Field And Cell Structure 54
    3.2.1 Cell Shape And Boundary 55
    3.2.2 Force Field 56
3.3 Cell Division 60
3.4 Cell Apoptosis 62
3.5 The CellSim3D Implementation 64
    3.5.1 The Integrator 64
    3.5.2 Boundary Conditions 66
    3.5.3 Multi-GPUs Implementation 68
    3.5.4 Neighbor List Method 71
    3.5.5 Simulation Units 72

4 *In silico* testing of the universality of epithelial tissue growth 75

4.1 Introduction 75

4.2 METHODS 78

4.2.1 CellSim3D Simulator and Model 78

4.2.2 Interface Scaling 80

4.3 Results 81

4.3.1 Linear Interfaces 81

4.3.2 Radial Interfaces 82

4.4 Conclusions 85

4.5 Supplemental Material 87

4.5.1 The *CellSim3D* model 87

Damped harmonic oscillator and angle force in *CellSim3D* 87

Adhesion, repulsion and intermembrane friction in *CellSim3D* 88

Cell growth and division 90

Modeling epithelial tissue 90

Parameterization 91

4.5.2 The *CellSim3D* software 91

4.5.3 Analysis methods 92

4.5.4 Chi-squared test 93

4.5.5 Analyses on Brú’s data set 93

5 Effect of substrate heterogeneity and topology on epithelial tissue growth dynamics 105

5.1 Introduction 105

5.2 Methods 110

5.2.1 CELLSIM3D SIMULATOR AND MODEL 110

5.2.2 Disorder 113

5.2.3 Colony configurations 113

5.3 Analyses . . . 114
  5.3.1 Scaling analysis . . . 114
    Interface width . . . 114
    Structure factor . . . 118
  5.3.2 Chi-squared minimization . . . 119
5.4 Results . . . 120
    Interface velocity . . . 120
    Fractal dimension . . . 121
    Roughness exponents for linear interfaces . . . 121
    Roughness exponents for radial growth . . . 123
5.5 Discussion and conclusions . . . 126

6 Conclusions and Future Work **130**

6.1 Conclusions . . . 130
6.2 Future Work . . . 134
  6.2.1 Cell Division Rules . . . 134
  6.2.2 Cell Polarity . . . 135
  6.2.3 Multicellular Tissue Simulation . . . 136
  6.2.4 Surface Analysis . . . 137

Bibliography **138**

Curriculum Vitae **172**

List of Figures

1.1 This figure illustrates the cell's cytoskeleton components: The actin filaments, microtubules, and intermediate filaments. Mechanical properties of the cell are derived from the interaction of these three elements. Image taken from Ref. [1] with permission from Elsevier Press. 4

1.2 Representation of cellular morphology throughout the eukaryotic cell cycle. The majority of time is spent in interphase, where growth and function occur, while M-phase is when cell division happens. Adapted from Figure 40.2 in Ref. [2] with permission from Elsevier Press. 5

1.3 The diagram depicts the progression of the apoptosis process, including nucleus condensation, cell shrinkage, blebbing, and phagocytosis. Adopted from Ref. [3], CC license 6

1.4 Figure shows some elementary processes on a surface. Green particles approaching the surface will fall at random locations. Yellow particles have broken their bonds with the surface and left the surface. Red particles diffuse in random directions on the surface. 10

1.5 Colony front and bulk images of a radially spreading HeLa cell colony captured at various times. Image taken from Ref. [4] with permission from American Physical Society (APS) Journals. 12

2.1 Deterministic growth curves that follow a specific pattern, as described by the KPZ equation. The inset demonstrates how lateral growth occurs locally along the surface normal. Image taken from Ref. [5] with permission from the American Physical Society (APS) Journals. 21

2.2 Surface local geometries are depicted schematically. It is energetically unfavorable for an atom to remain on top of the surface with the local hill, which has a positive chemical potential and, consequently, a negative local Laplacian. At the local valley, the local Laplacian, which is the inverse of the radius r_2 of the circle that fits the surface locally, is positive, corresponding to a negative chemical potential. Lastly, on a flat surface, the chemical potential of an atom is zero, and the radius, R, of the circle is infinite. 26

2.3 RG flow in a 3d space of coupling. The fixed point K^* has a basin of attraction with two irrelevant directions and one relevant direction. 40

2.4 The flow for coupling constant g in (a) one dimension, where a non-zero fixed point is attractive and determines the scaling exponents, and (b) two dimensions, where a non-zero fixed point is repulsive, separates the linear regime, $\lambda = g = 0$ from the strong coupling regime for which in $\lambda \to \infty$ for one loop approximation. Adapted from Figure 7.4 in [6] with permission from Cambridge University Press. 42

2.5 By use of ballistic deposition (BD) [7], square particles are deposited one at a time from random heights above a flat substrate; these particles adhere to the substrate upon initial contact. The attachment points of squares A and B to their respective surfaces are shown by the dashed lines squares A and B. 47

2.6 Figure illustrates two distinct Eden models. In both models, the growth started from the red square. In the subsequent stage, one of the neighboring sites to the surface will be chosen, where in the (a) all unoccupied sites have the same probability p, however in the (b) the probability is dependent on the number of bonds each unoccupied site has with the surface. 48

2.7 (a) the DT model and (b) the WV model. The columns of incidence of the particles are shown by large vertical arrows. Small arrows indicate the path of a particle after it collides with the surface, and when there are two possible courses of action, one is chosen at random. Image taken from Ref. [8] with permission from Elsevier Press. 49

2.8 The DPD model [9] for surface growth without overhangs. The blue sites represent a system that expands in a lattice with quenched disorder (red sites). 51

3.1 In our model, we suppose that the cell is a sphere and that its mechanical properties are comparable to those of a viscoelastic sheet represented by a network of connected balls. Models are constructed using the C180 molecule's shape and topology, as well as the positions of its carbon atoms at equilibrium. The nodes that are closer to the viewer are shown in a larger size than those that are farther away. 55

3.2 The intracellular forces acting on node i are dependent on the node's first and second neighbors. This node's three initial neighbors, j, will give the bond forces, while each initial neighbor's two additional neighbors, k, will offer the angle forces. For convenience, only one of the first and second neighbors is labeled. 57

3.3 The position of two cells (m and n) that are close enough to activate intercellular forces. The attracting and repulsive forces will be parallel to $\hat{r}_{ij}$ and between the two nodes i and j. In addition, they will suffer a frictional force tangent to the relative velocity $\mathbf{v}_{ij} = \mathbf{v}_i - \mathbf{v}_j$. 59

3.4 The nodes of a cell larger than the threshold division volume are copied (black and red). The cell is divided in half by a randomly oriented division line (green). The nodes of the two new cells are projected so that the nodes in contact are placed along the division plane. Image taken from Ref. [10] with permission from Elsevier Press. 62

3.5 Before the apoptotic cell is removed, it undergoes disassembly process, which includes membrane blebbing, membrane protrusion formation, and cell fragmentation. Image taken from Ref. [11], CC license. 63

3.6 The Lees-Edwards boundary conditions are shown in the figure. The simulation box is located in the center of the cell at the center. At the same time, the upper and lower replicas are travelling in the opposite directions with speed $\dot{\gamma}L$. 67

3.7 In the spatial decomposition algorithm, the mechanism by which a processor obtains adjacent atom positions. All atom positions in adjacent boxes in the (a) east/west (b) north/south (c) up/down directions can be communicated in six data exchanges. Adapted from Figure 10 in Ref. [12] with permission from Elsevier Press. 70

4.1 Interface evolutions of cell colonies starting from a horizontal line and a radially expanding interface. (a) Line configuration at weak (10) and (b) strong cell-cell adhesion (2000). (c) Radially expanding interface with at weak (10) and (d) strong adhesion (2000). All interfaces have overhangs. Scaling analysis was done using overhang-corrected interfaces [6]. For the units, see Table 4.1. . 79

4.2 (a) Velocity ($\langle v \rangle$) of the interface determined from the mean colony radius $\langle R \rangle$ and the mean interface height $\langle h \rangle$ vs. time for different cell-cell adhesion strengths. Radially expanding interface: (red circles) at weak (10) and (blue circles) strong adhesion ($2,000$). Line configuration: (green triangles) at weak and (orange triangles) at strong adhesion. (b) The fractal dimension (d_{f}) determined by plotting box counts vs. box size. For radially expanding interface: (red circles) at weak (10) and (blue circles) strong adhesion ($2,000$). For line configuration: (green triangles) at weak and (orange triangles) strong adhesion. For units, see Table 4.1. 82

4.3 Data collapse for line growth at high adhesion at three different times. (a) Using the structure factor (Eq. 4.6) and MBE exponents, $\alpha^{\mathrm{MBE}} = \frac{3}{2}$ and $z^{\mathrm{MBE}} = 4$. (b) With KPZ exponents, $\alpha^{\mathrm{KPZ}} = \frac{1}{2}$ and $z^{\mathrm{KPZ}} = \frac{3}{2}$. The y-axis is scaled with the factor $(\mathrm{kt}^{\frac{1}{z}})^{\frac{3}{2}}$ to have the same range as MBE scaling. (c) Using the Family-Vicsek relation for width (Eq. 4.1) with MBE exponents, $\beta^{\mathrm{MBE}} = \frac{3}{8}$ and $z^{\mathrm{MBE}} = 4$, and (d) with KPZ exponents, $\beta^{\mathrm{KPZ}} = \frac{1}{3}$ and $z^{\mathrm{KPZ}} = \frac{3}{2}$. For units, see Table 4.1. 83

4.4 Data collapse for the radially growing interface at low adhesion at three different times. (a) Using the structure factor (Eq. 4.6) with MBE, $\alpha^{\mathrm{MBE}} = \frac{3}{2}$ and $z^{\mathrm{MBE}} = 4$ and (b) KPZ exponents, $\alpha^{\mathrm{KPZ}} = \frac{1}{2}$ and $z^{\mathrm{KPZ}} = \frac{3}{2}$. The y-axis is scaled with the factor $(\mathrm{kt}^{\frac{1}{z}})^{\frac{3}{2}}$ to have the same range as MBE scaling. (c) Using the Family-Vicsek relation for width (Eq. 4.1) with MBE exponents, $\beta^{\mathrm{MBE}} = \frac{3}{8}$ and $z^{\mathrm{MBE}} = 4$, and (d) with KPZ exponents, $\beta^{\mathrm{KPZ}} = \frac{1}{3}$ and $z^{\mathrm{KPZ}} = \frac{3}{2}$. For units, see Table 4.1. 84

4.5 Log-log plot of the colony interface width vs growth time of the linear interface for different adhesion strength, 10 (blue) and $2,000$ (orange). Growth exponents are $\beta^{\mathrm{weak}} = 0.28 \pm 0.01$ and $\beta^{\mathrm{strong}} = 0.25 \pm 0.02$, respectively. For units, see Table 4.1. 100

4.6 Log-log plot of the colony interface width of the linear interface vs length l at three different times. (a) Weak adhesion strength (10) with $\alpha_{\mathrm{loc}}^{\mathrm{weak}} = 0.59 \pm 0.01$ (b) strong adhesion strength (2,000) with $\alpha_{\mathrm{loc}}^{\mathrm{strong}} = 0.62 \pm 0.02$. For units, see Table 4.1. 100

4.7 Log-Log plot of the structure factor at three different times for linear expanding interface. (a) weak adhesion strength (10) with $\alpha_{\mathrm{glob}}^{\mathrm{weak}} = 0.75 \pm 0.04$. (b) strong adhesion strength (2,000) with $\alpha_{\mathrm{glob}}^{\mathrm{strong}} = 0.52 \pm 0.02$. For units, see Table 4.1. . 101

4.8 Log-log plot of the colony interface width vs growth time of the radially expanding interface for different adhesion strength, 10 (blue) and 2,000 (orange). Growth exponents are $\beta^{\mathrm{weak}} = 0.40 \pm 0.04$ and $\beta^{\mathrm{strong}} = 0.42 \pm 0.06$, respectively. 101

4.9 Log-log plot of the colony interface width of the radially expanding interface vs length l at different times. (a) Weak adhesion strength (10) with slope $\alpha_{\mathrm{loc}}^{\mathrm{weak}} = 0.66 \pm 0.01$, and (b) strong adhesion strength (2,000) with slope $\alpha_{\mathrm{loc}}^{\mathrm{strong}} = 0.70 \pm 0.01$. For units, see Table 4.1. 102

4.10 Log-log plot of the structure factor at three different times for the radially expanding interface. (a) Weak adhesion strength (10) with $\alpha_{\mathrm{glob}}^{\mathrm{weak}} = 0.95 \pm 0.04$, and (b) strong adhesion strength (2000) with $\alpha_{\mathrm{glob}}^{\mathrm{strong}} = 0.71 \pm 0.02$. 102

4.11 Log-Log plot of the structure factor of radially expanding interfaces for (a) The division plane is sampled from a unit circle in the epithelial plane, and can yield two symmetric or asymmetric daughter cells in size. (b) The cell population can contain only one type of cell or two types of cells with different stiffness interacting with each others. (c) different friction coefficients for cell-cell interaction, and (d) different medium friction forces. For units, see Table 4.1. 103

4.12 (a) Data collapse using Family-Vicsek relation for width functions digitized from Fig. 3 from Brú *et al.* [13], at different times with (a) MBE exponents, $\beta = \frac{3}{8}$ and $z = 4$, and (b) KPZ exponents, $\beta = \frac{1}{3}$ and $z = \frac{3}{2}$. 104

5.1 (a-b) Colony expansion (red cells) in a medium with quenched disorder (blue cells) with linear initial configuration. (a) At weak and (b) strong cell-cell adhesion strength. (c) Interface evolution at different times (d) at weak and (lower right) strong cell-cell adhesion strength. The scaling analysis was done using overhang-corrected interfaces [6]. For units, see Table 5.1. 115

5.2 (a,b) Radially growing colony (red cells) in a medium with quenched disorder (blue cells). (a) At weak and (b) strong cell-cell adhesion strength. (c) Interface evolution at different times at weak cell-cell adhesion strength. The interface has overhangs, but the scaling analysis was done using overhang-corrected interfaces [6]. (d) Morphology for a system started with a single cell at the centre of a box on a substrate with a high density of quenched disorder at weak cell-cell adhesion strength. Due to the high disorder density, the morphology is not round but instead chiral with branched structures. Eventually the interface becomes pinned by the disorder and the growth stops. The final population of the cell colony consists of roughly 10,000 cells. For units, see Table 5.1. 116

5.3 Interface velocity calculated from the time evolution of the mean colony radius ($\langle R \rangle$) and the mean interface height ($\langle h \rangle$) for radially (circles) and linearly (triangles) expanding interfaces, respectively. For units, see Table 5.1. 120

5.4 Fractal dimension (d_f) determined by plotting box counts vs. box size for the linear interface (triangles) 1) at weak (red triangles) and 2) at strong (orange triangles) adhesion strength, and 3) at weak cell-cell adhesion in high disorder density (purple triangle). For the radially expanding interface (circles) 1) at weak (green circles) and 2) strong (blue circles) cell-cell adhesion, and high disorder density (violet circles). The colony fractal dimension, ($d_\mathrm{f}^\mathrm{col}$), for colony expansion at weak cell-cell adhesion began with a single cell in the centre of a box on a substrate with a high density of quenched disorder. This system does not have a dense and round morphology, instead it forms slowly to a chiral morphology with branched structure until the colony interface becomes pinned with the disorder on the substrate. The colony fractal dimension is very close to the DLA fractal model, $d_\mathrm{f} = 1.71$. 122

5.5 The structure factor (Eq. 5.10) measured at three different times, green: long time; orange: intermediate time; blue: short time, and different conditions (indicated by line type; legend). (a) For the linear interface: Solid lines: strong cell-cell adhesion and low disorder density; dashed lines: weak adhesion, low disorder density; dotted lines: weak adhesion, high disorder density. The black dashed line with a slope of = −2.0 is drawn to guide the eye. (b) for the radial interface at low disorder density: Solid lines: strong cell-cell adhesion; dashed lines: weak adhesion. The black dashed line with a slope of = −2.26 is drawn to guide the eye. The global roughening exponent for each case is reported in Table 5.3. For units, see Table 5.1. 124

5.6 The height-height correlation function vs length (ℓ) for the linear interface in a medium (a) with quenched disorder (b) without quenched disorder, and for the radial interface in a medium (c) with quenched disorder (d) without quenched disorder at (green) long (orange) intermediate (blue) short time at different adhesion strengths and disorder densities: Solid lines: strong cell-cell adhesion and low disorder density; dashed lines: weak adhesion, low disorder density; dotted lines: weak adhesion, high disorder density. The correlation function exponents, ζ, are reported in the Table 5.3. For units, see Table 5.1. 127

List of Tables

3.1 This table represents the DPD-VV integration algorithm implemented in *CellSim3D* [10, 14], where $\mathbf{F}^{\mathrm{C}}$ represents the conservative forces, $\mathbf{F}^{\mathrm{D}}$ represents the dissipative forces, and $\mathbf{F}^{\mathrm{R}}$ represents the random forces. $\mathbf{x}_i$ and $\mathbf{v}_i$ are the positions and velocities of particle i whereas m_i is the particle's mass and Δt is the time step. 65

3.2 These parameters determine the mechanical properties of each cell. They are usually adjusted to represent a variety of different cell types. *CellSim3D* uses the symbol *dagger* to represent units of Δt and $*$ units of mean cell division time, which depends on the cell types and is set to 1.0 in *CellSim3D*. For the derivation and details, please see Refs. [10, 15] 74

4.1 Each cell's mechanical properties are determined by the values indicated here. They are usually subtly altered to represent different types of cells. The mechanical properties of cells addressed in this work are listed in the table. The symbol † indicates units of Δt and $*$ units of mean time to cell division, which varies between cell types and is set to 1.0 in *CellSim3D*. For more details and their derivation, please see Refs. [10, 15] 95

4.2 Table shows the Chi-squared values, Eq. 4.19, (degrees of freedom) and p-values (goodness of fit) for the graphs in Fig. 3a, which provides data collapse of the structure factor with MBE scaling exponents for line growth at strong cell-cell adhesion at three different times. The large off diagonal chi-squared values and near-zero off diagonal p-values show that the curves in Fig. 3a at different times do not overlap with each other. 96

4.3 Table shows the Chi-squared values, Eq. 4.19, (degrees of freedom) and p-value (goodness of fit) for the graphs in Fig. 3b, which provides data collapse of the structure factor with KPZ scaling exponents for line growth at strong cell-cell adhesion at three different times. The low off diagonal chi-squared values and mid-range off diagonal p-values indicate that the curves in Fig. 3b at different times roughly overlap with each other. 96

4.4 Table shows the Chi-squared values, Eq. 4.19, (degrees of freedom) and p-value (goodness of fit) for the graphs in Fig. 3c, which provides data collapse of the width function with MBE scaling exponents for line growth at strong cell-cell adhesion at three different times. The large off diagonal chi-squared values and zero off diagonal p-values show that the curves in Fig. 3c at different times do not overlap with each other. 97

4.5 Table shows the Chi-squared values, Eq. 4.19, (degrees of freedom) and p-value (goodness of fit) for the graphs in Fig. 3d, which provides data collapse of the width function with KPZ scaling exponents for line growth at strong cell-cell adhesion at three different times. The low off diagonal chi-squared values and near-one off diagonal p-values indicate that the curves in Fig. 3d at different times certainly overlap with each other. 97

4.6 Table shows the Chi-squared values, Eq. 4.19, (degrees of freedom) and p-value (goodness of fit) for the graphs in Fig. 4a, which provides data collapse of the structure factor with MBE scaling exponents for the radially growing interface at weak cell-cell adhesion at three different times. The low off diagonal chi-squared values and mid-range off diagonal p-values indicate that the curves in Fig. 4a at different times roughly overlap with each other. 98

4.7 Table shows the Chi-squared values, Eq. 4.19, (degrees of freedom) and p-value (goodness of fit) for the graphs in Fig. 4b, which provides data collapse of the structure factor with KPZ scaling exponents for the radially growing interface at weak cell-cell adhesion at three different times. The large off diagonal chi-squared values and zero off diagonal p-values show that the curves in Fig. 4b at different times do not overlap with each other. 98

4.8 Table shows the Chi-squared values, Eq. 4.19, (degrees of freedom) and p-value (goodness of fit) for the graphs in Fig. 4c, which provides data collapse of the width function with MBE scaling exponents for the radially growing interface at weak cell-cell adhesion at three different times. The low off diagonal chi-squared values and near-one off diagonal p-values indicate that the curves in Fig. 4c at different times certainly overlap with each other. 99

4.9 Table shows the Chi-squared values, Eq. 4.19, (degrees of freedom) and p-value (goodness of fit) for the graphs in Fig. 4d, which provides data collapse of the width function with KPZ scaling exponents for the radially growing interface at weak cell-cell adhesion at three different times. The large off diagonal chi-squared values and zero off diagonal p-values show that the curves in Fig. 4d at different times do not overlap with each other. 99

5.1 The parameters for the cells used in this study. These values are based on the HeLa (named after Henrietta Lacks [16]) cell properties. † indicates units of Δt and $*$ units of mean time to cell division, which varies between cell types and is set to 1.0 in CellSim3D. 112

5.2 The area density, $\frac{N}{A}$, for quenched disorder in SI units ($\frac{1}{\mu\mathrm{m}^2}$) in the different configurations (linear and radial), and at different attraction stiffnesses ($\frac{\mathrm{nN}}{\mu\mathrm{m}}$). The parameters for the strong and weak cases are given in Table 5.1. 113

5.3 Interface fractal dimension (d_f), global (α) and local (α_loc) roughness exponents, correlation function exponent (ζ; Eq. 5.5), growth exponent (β), and average step height exponent (λ), in different configurations with different cell-cell adhesion stiffness strengths, and quenched disorder densities, see Tables 5.1 and 5.2. For the DLA-like chiral geometry, the fractal dimension is the colony fractal dimension. The exponents for the well-knows cases of KPZ, qKPZ and MBE for one-dimensional interfaces are also given for reference. † indicates experiments in heterogeneous media and $*$ indicates the crossover with two different regimes. 125

List of Abbreviations, Symbols, and Nomenclature

CAMs	Cell Adhesion Molecules
DNA	Deoxyribonucleic Acid
ECM	Extracellular Matrix
ATP	Adenosine Triphosphate
mRNA	Messenger Ribonucleic Acid
EW	Edward Wilkinson
KPZ	Kardar-Parisi-Zhang
qKPZ	quenched Kardar-Parisi-Zhang
MBE	Molecular Beam Epitaxy
CA	cellular Automaton
RG	Renormalization Group
RMS	Root Mean Square
BD	Ballistic Deposition
DPD	Directed Percolation Depinnin
DT	Das Sarma and Tamborenea
WV	Wolf-Villain
DLA	Diffusion-limited aggregation
MD	Molecular Dynamics
GPU	Graphics Processing Unit
RAM	Random Access Memory
MPI	Message Passing Interface
RDMA	Remote Data Memory Acces
CUDA	Compute Unified Device Architecture
FGCI	Finnish Grid and Cloud Infrastructur
DPD-VV	Dissipative Particle Dynamics velocity Verlet
PBCs	Periodic Boundary Conditions
LEbc	Less-Edward boundary conditions
SD	Spatial Decomposition
SIMD	Single Instruction, Multiple Data
SoA	Structure of Arrays

Chapter 1

Introduction

1.1 Mechanical Cell Models

The study of the relationship between cell biomechanics and human health concerns, such as the onset and progression of human diseases such as arthritis, asthma, and tumor progression, has expanded rapidly over the past decade [17]. There is abundant evidence that, in addition to biochemical interactions, cells engage in mechanical interactions with their environments and with one another [18]. These mechanical properties of the cells and tissues revealed the significance of applying the framework of classical mechanics from physics and engineering to the study of biological problems. Understanding how cells and tissues respond to mechanical stress can help us to prevent, detect, and treat diseases such as cancer and heart diseases [19, 20, 21]. Previous studies have helped our comprehension of the mechanical foundation of processes such as tissue development, organ function, tissue mechanical response, and related subjects [22, 23, 24, 25]. Studying cell tissue mechanics raises a number of unsolved questions, many of which are of crucial importance to medicine and biomedical engineering. Here, we mention a few of these crucial questions:

1. As mechanical stress and load start to vary, how do different cells and tissues respond to it?

2. How do mechanical properties and forces influence the onset and progression of disease?
3. How does the diversity in mechanical properties and responses of various cells in a tissue affect the mechanical properties of the tissue?
4. How can tissues be engineered to have specified mechanical properties?

Due to the rising interest in understanding the mechanics of cells and tissues, momentum is gaining in the scientific community for the development of cellular tissue models. Incredibly rapid developments in experimental techniques and computational power over the past few decades have made it feasible to better comprehend and simulate the mechanics and dynamics of tissue growth [26], cells deformation [27] and cell subcellular components such as the cytoskeleton [28]. Since the mechanical properties of tissues are controlled by the mechanical properties of their constituent cells and the extracellular matrices, the mechanical properties of cells have a crucial role in developing accurate and predictive models of tissue mechanics [29, 30, 31]. Hence, in order to accurately represent the mechanical behavior of tissues, it is required to take into account a number of essential factors, including cell membrane stiffness, cell cytoskeleton mechanical properties, and cell growth and division processes. Here, we discuss some of these factors:

- Cell Shape and Geometry: A cell's response to and generation of mechanical stresses within tissues are influenced by cell shape and geometry. For example, cells with an elongated shape may be less likely to change along their long axis than cells with a spherical or more uniform shape. In addition, cell size and aspect ratio can also play a role in how a cell deforms and transmits tension into its environment [32, 33].
- Cell Boundary: The mechanical properties of the cell membrane influence both the response of cells to mechanical stimuli and their ability to deform in response to such stimuli. However, the membranes on their own are insufficient to support the structure of the cell [34]. The cell membrane encases the entire cell and is composed of a phospholipid bilayer interspersed with various types of proteins and oligosaccharides [35].

The cell membrane is a ”selective barrier” [36] and regulates the passage of various substances into and out of the cells. The mechanical properties of the cell membrane are viscoelastic, meaning that they vary not only with force magnitude but also with force frequency and duration [37, 38].

- Cell Cytoskeleton: The cytoskeleton is a network of protein filaments that provides mechanical support to the cell. Cytoskeleton networks, which are found in most eukaryotic cells and made of long self-assembled supramolecular polymers, are responsible for the cell’s interior mechanical characteristics, and the generation and transmission of mechanical forces [39]. They also assist in the transmission of internal and extracellular signals throughout the cell. The cell’s internal network of intermediate filaments and microtubules serve to strengthen and stabilize the cell [40, 41]. In addition to protecting the cell’s membrane from mechanical shocks, they convey messages from the cell’s interior to the cell membrane.

  In animal cells, the mechanical characteristics of the cells are also dependent on the actomyosin cortex of the cytoskeleton [2, 42]. The actomyosin cortex is a network of protein fibers called F-actin that are directed around the cell to form a mesh that covers the entire cell [43, 2, 44, 45]. Molecular motors like myosin can create an active binding between the fibers. The network’s average stiffness and viscosity can be altered by changes in myosin concentration and activity [42]. Cells control the polymerization of F-actin supramolecular polymer, the activity and concentration of myosin motors to cause a wide range of intriguing cell movements [46]. Research on the actomyosin cortex in greater depth has been done using models like those in Refs. [47, 48]. Figure 1.1 shows the cell’s cytoskeleton.

- Cell Adhesion: The adhesion of cells to their substrate or to adjacent cells can impose forces on the cells and their environment, thereby contributing to tissue organization and mechanics [49]. Many proteins, referred to as Cell Adhesion Molecules (CAMs), are

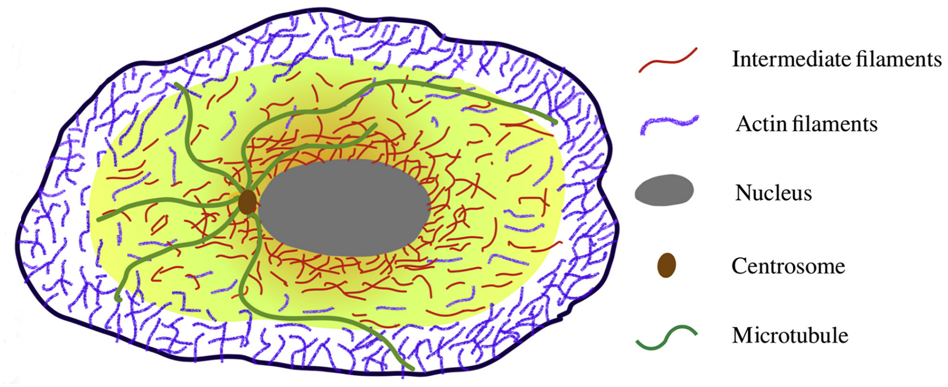

Figure 1.1: This figure illustrates the cell's cytoskeleton components: The actin filaments, microtubules, and intermediate filaments. Mechanical properties of the cell are derived from the interaction of these three elements. Image taken from Ref. [1] with permission from Elsevier Press.

found in the cell membrane and are involved in the cell's interactions with its environment and with other cells. These molecular interactions within the cell membranes result in mechanical cell-cell interactions. This family of proteins is divided into a number of subfamilies, including integrins, selectins, cadherins, and others [47]. The kind and quantity of these proteins in the membrane are controlled by the cell. For example, focal points with a higher concentration of CAMs can be formed when the cell is in need of stronger or more persistent adhesion sites [50]. These cell-cell interactions play an important role in several biological processes, such as the formation and stability of biological tissues [51, 52, 53, 54] and selective adhesion in embryonic development [47]. Tissue morphology is also influenced by the strength and density of intercellular junctions along the cell surface. A range of biochemical variables control these junctions' strength, density, and locations [55, 51, 52].

- Cell Growth and Division: Cell division is a crucial factor in tissue development. The number of cells in a tissue, their size, and their distribution can all be altered by cell division and proliferation. Cell development and growth are driven by the flux of materials from the outside environment into the cell itself. There are four main phases in the cell

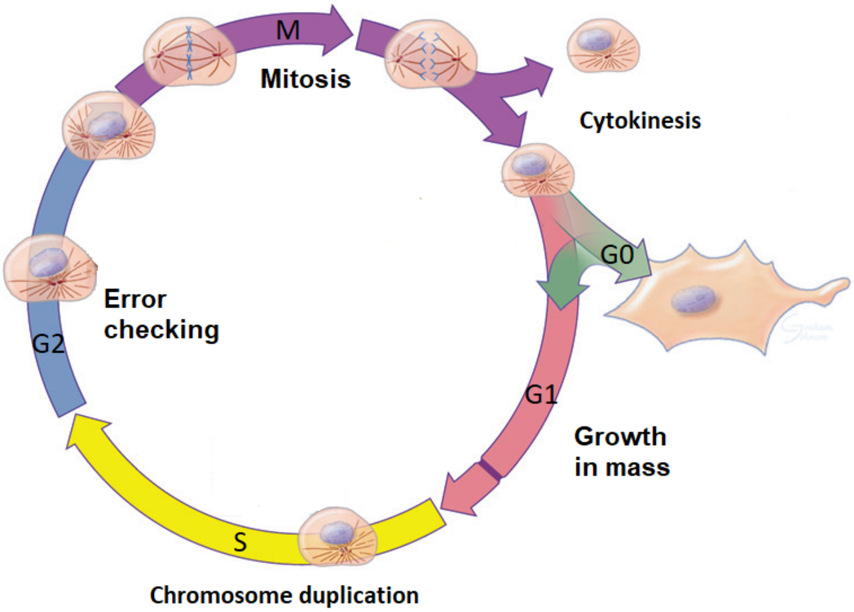

Figure 1.2: Representation of cellular morphology throughout the eukaryotic cell cycle. The majority of time is spent in interphase, where growth and function occur, while M-phase is when cell division happens. Adapted from Figure 40.2 in Ref. [2] with permission from Elsevier Press.

cycle: two growth phases ($G1$ and $G2$), the synthesis phase (S), and the mitosis phase (M) [56, 2]. Most growth happens in $G1$ and $G2$. A new cell's size will have more than doubled by the time it has completed the $G1$ phase. DNA replication frequently takes place at several spots along the DNA strand throughout the course of the synthesis, S, phase. In $G2$ phase, a protein complex connects the two copies of DNA for the purpose of detecting damage or replication errors. Lastly, the cell's mass grows and drives it into M phase [56, 57]. Mitosis is the shortest phase of the cell life cycle, accounting for only a small fraction of the total lifespan of the cell cycle. A resting state known as $G0$, also known as ”senescence”, happens outside of the usual life cycle of cells and allows them to stay in this condition for a long time. During this phase, cells are extremely active and performing their duties, which may involve migration. These steps are illustrated in Fig. 1.2.

Before the known process of cell division starts, a protein-rich structure called the mitotic spindle is utilized by the cell to transmit two copies of DNA (chromatids) to opposite ends of the cell [58]. There are several types of cell division, including cytokinesis, meiosis, and binary fission [59, 60, 61]. Cytokinesis [59], occurs almost concurrently with *M* phase [2] where an actomyosin band develops perpendicular to the mitotic spindle and divides the parent cell in two. Over time, the spindle disintegrates and the cell membrane becomes deformed, leaving behind two daughter cells [59]. Cells are capable of dividing symmetrically and asymmetrically, resulting in the production of two identical or diverse daughter cells.

- Cell Shrinkage and Cell Apoptosis: A programmed cell death is a natural process that occurs during biological processes including aging, the growth and function of the immune system, and embryo development [62, 63, 64]. Apoptosis and necrosis are two cell death processes that can occur simultaneously, depending on factors such as the stimulus's intensity and duration, the degree of ATP depletion, and the availability of caspases [62]. Cell death regulation abnormalities can be a crucial factor in diseases such as cancer [65]. If an apoptotic cell is removed from a tissue, the surrounding cells may rearrange themselves to fill the void, hence affecting the density and shape of the tissue [66]. As a result, the mechanical stress pattern within the tissue will change, leading to modifications in tissue rigidity, elasticity, and other mechanical properties. From initiation to completion, apoptosis can occur in a short time as 2–3 hours [67]. Methodology based classification

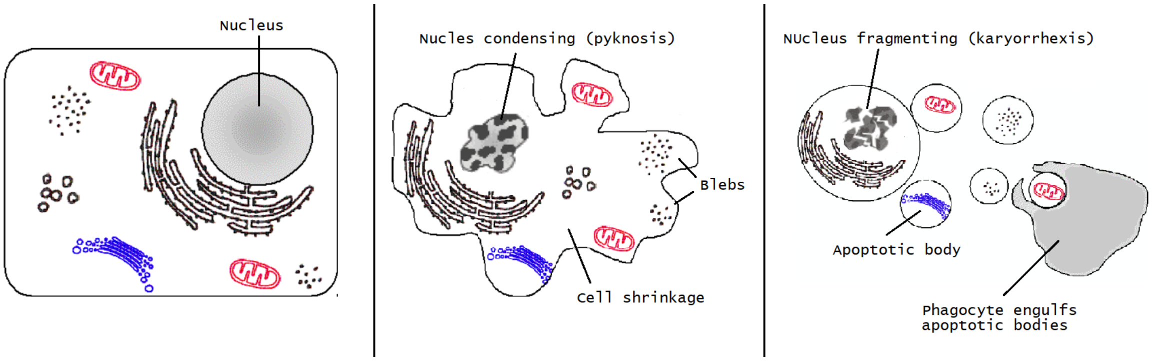

Figure 1.3: The diagram depicts the progression of the apoptosis process, including nucleus condensation, cell shrinkage, blebbing, and phagocytosis. Adopted from Ref. [3], CC license

of apoptosis assays into six major groups such as cell shrinkage, nuclear fragmentation, DNA fragmentation, mRNA decay, etc [62]. During the initial phase of apoptosis, light microscopy reveals cell shrinkage and pyknosis. As a result, cells shrink in size, cytoplasm gets denser, organelles become more tightly packed, and electron-dense nuclear material accumulates often peripherally under the nuclear membrane [68]. Then, the extensive plasma membrane blebbing occurs, where the cell's cytoskeleton disintegrates, causing the membrane to bulge [69]. It is followed by the "budding" phase, where the karyorrhexis and the dissociation of cell fragments into apoptotic bodies occurred. Finally, these apoptotic bodies are phagocytosed by macrophages, parenchymal cells, or neoplastic cells and eliminated in phagolysosomes [62]. A simplified description of the apoptosis process is shown in Fig. 1.3.

Throughout the last few decades, numerous research groups have attempted to model biological phenomena to generate new testable hypotheses [70]. There are two primary modelling approaches for biological phenomena: the mathematical and the computational [71, 72]. Mathematical models for simulating biological systems are continuous in time and space and are based on sets of differential equations. Numerous mathematical continuum models have been developed to examine the mechanisms underlying the control of the cell cycle, cell death, cellular renewal, and sub-cellular behaviors such as DNA regulation [73, 74, 75].

Computational models represent and execute the models via computer-programmed operational descriptions based on theoretical foundations such as the stochastic master equations or the laws of classical mechanics. Among these models, those that identify the cell as the fundamental unit of model development can be loosely classified into two categories: those that require a lattice to function [76, 77] and those that do not [78, 79]. In lattice-based models, the cell is often modelled as a lattice site, which allows for the modelling of enormous cell population sizes, as in the Cellular Potts Model [80] and cellular automata [76, 77], whereas in off-lattice models, cells are represented as a spherical ball or polygonal structure with interacting edges and faces, as in vertex models [78].

The majority of the aforementioned computational models lack the required resolution to appropriately approximate inter-membrane interactions and forces at the subcellular level. Taking into account the previously described cell mechanical features, our research group developed a theoretical and computational off-lattice model , *CellSim3D*, with the following assumptions [10]:

- Cell membrane modelled as a viscoelastic material to reproduce the membrane's stiffness and flexibility.
- The mechanical properties of a cell, such as membrane stiffness and adhesion strength, are uniform in all directions.
- Intercellular communication is restricted to mechanical contact over short distances.
- The environment of a cell is modeled as a viscous fluid.
- Cells divide symmetrically by positioning the division plane through their center of mass
- The force field takes into account the intracellular forces, such as the damped spring force between nodes connected to three nearest neighbors on the cell surface and internal pressure, and the intercellular interactions, such as adhesion and repulsion between cells, friction between cells, and friction between cells and the intercellular medium.

CellSim3D allows us to investigate purely mechanical aspects of cell behavior and cell division, such as the manner and strength with which cells interact mechanically with one another and their environment, the mechanical effects of a cell's growth and division on its neighbors, as well as a cell's mechanical response to external stimuli [10]. In this dissertation, we incorporated new cell mechanical parameters and force fields, such as new boundary conditions, the asymmetric division rule, cell shape diversity, and the apoptosis process, into the *CellSim3D* framework and investigated large-scale cell population growth using this model. The old version of the *CellSim3D* was implemented to run on a single GPU, while the current version of *CellSim3D* offers researchers a fast, open-source cell simulator that can operate on multiple GPUs to simulate large-scale tissue growth and colloidal dynamics with precise control over the mechanical properties of the cells and colloidal particles. The current multi-GPU version also permits researchers to simulate multicellular tissue composed of two distinct cell types with different mechanical properties. The simulator's source code is available on github: `https://github.com/SoftSimu/CellSim3D`

1.2 Epithelial Tissue Growth Dynamics

In recent decades, various experimental studies on growth phenomena in biological systems, such as the cultivation of agar in a petri dish [81, 82], the growth of healthy and cancerous cell colonies *in vivo* and *in vitro* [13, 4], and the cell colony growth in a gel medium [83] have been performed. Cell colony growth depends on a wide variety of biochemical regulations and mechanical factors, including, but not limited to, intercellular interactions, nutrient concentrations, the mechanisms of cell division and apoptosis, as well as the extracellular matrix and cellular migration [84]. Studying the mechanical factors that influence tissue growth and how they manifest in the kinetics and morphology of cell aggregation necessitates the characterization of the interfacial growth of cellular colonies. In this work, we investigated the effect of the cell mechanical properties on the cellular colony expansion and the colony interface morphology and roughness.

To study the growth of surfaces within the framework of statistical physics, two complementary approaches exist: the atomistic approach and the continuum approach [6]. In atomistic approach, the influence of microscopic mechanics such as deposition, desorption, and surface diffusion on the morphology of surfaces has been investigated. For instance, in the growth of the crystal surface, vapor atoms fall to the substrate at random positions, and form chemical bonds with other atoms. After deposition, the deposited atoms can also diffuse throughout the surface and seek an energetically favorable position. Depending on experimental parameters such as temperature, the length of this diffusion might sometimes be long. Atoms can escape the interface if the bonds to surfaces completely break; however, this depends on the strength of the bond. This phenomenon is known as desorption [6]. Figure 1.4 shows these processes on a two-dimensional surface. The continuum approach studies the surface on a coarse-grained scale. In this approach, it is crucial to comprehend the underlying symmetries and conservation laws governing growth before developing the continuum equations describing the roughening of the surface.

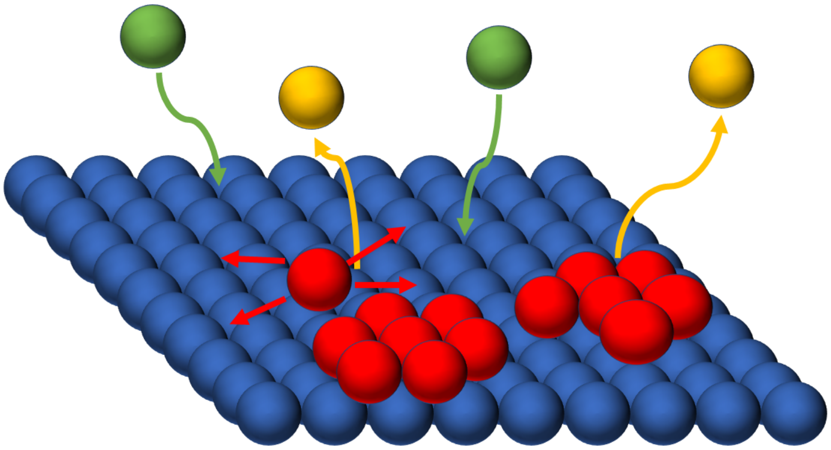

Figure 1.4: Figure shows some elementary processes on a surface. Green particles approaching the surface will fall at random locations. Yellow particles have broken their bonds with the surface and left the surface. Red particles diffuse in random directions on the surface.

There are a number of well-known scaling universality classes of surface roughness scaling defined by their own critical exponents. Scaling analysis is a commonly used technique to calculate these critical exponents of a surface. Each of these scaling universality classes identifies the fundamental growth mechanisms involved in surface growth. Three well-known scaling universality classes are:

- Edwards-Wilkinson (EW) [85]: This universality class is associated with the surface growth phenomenon, in which randomly deposited atoms relax to the lowest site in their neighborhood to minimize their gravitational potential energy.

- Kardar-Parisi-Zhang (KPZ) [5]: In this class of universality, the main surface growth mechanism is the lateral growth, meaning the surface expands in a direction that is locally normal to the interface.

- Molecular Beam Epitaxy (MBE) [86]: The surface diffusion mechanism of the deposited atoms are the physical mechanism that distinguishes molecular beam epitaxy from other growth universality classes. The deposited atoms move until they locate the most energetically favorable positions where they have more bonds with their neighboring atoms. The diffusion length can be quite large and is influenced by variables such as temperature.

Experimental studies reveal that the interface growth of radially and linearly expanding cell colonies has diverse scaling behavior. Brú *et al.* examined cell proliferation using 15 distinct *in vitro* cell lines and 16 distinct patient-derived *in vivo* tumor cell types [87, 13]. They discovered that the growth belongs to the MBE universality class. They showed that interface dynamics are characterized by a linear growth rate, the restriction of growth activity to the cell colony or tumor's outer border, and diffusion at the colony surface, which indicates that cells move along the colony border as opposed to moving freely away from it [13]. A decade later, Huergo *et al.* found that both HeLa (cervix carcinoma) and Vero cell colonies show KPZ-like behaviors at their interfaces, characterised by lateral growth due to cell duplication or size increase or cell migration on the colony interface along the local normal to the interface [88, 89, 4], see Fig. 1.5. Huergo *et al.* also examined the 2D growth dynamics of quasilinear Vero cell colony fronts in a methylcellulose-containing culture medium and found that the dynamical behavior of the colony interface is roughly equivalent to that predicted by a quenched KPZ (qKPZ) model [83]. Galeano *et al.* also examined the development of two plant cell species, *Brassica oleracea* and *B. rapa*, under varied growing conditions and demonstrated that none of the well-known universality classes for dynamics can account for the observed results [90].

These experimental results of the cell interface dynamics raise the question of whether the cell interface dynamics may be characterized by a well-known scaling universality class. This diversity in the growth behavior of cell colonies is advantageous for efficient evolution

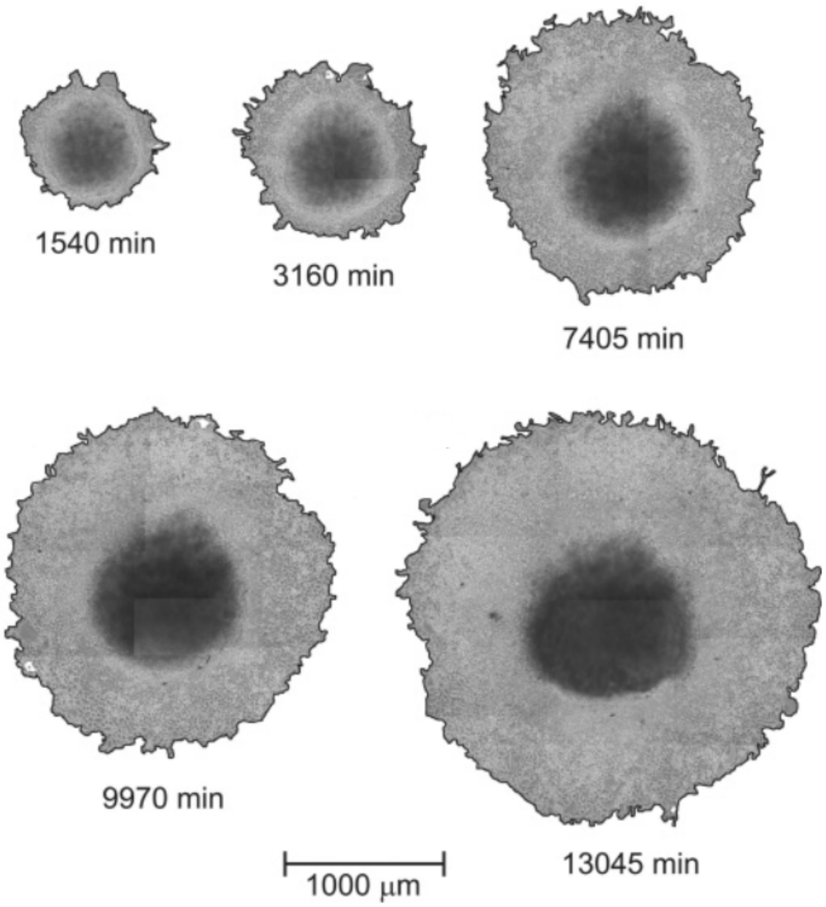

Figure 1.5: Colony front and bulk images of a radially spreading HeLa cell colony captured at various times. Image taken from Ref. [4] with permission from American Physical Society (APS) Journals.

and adaptable growth dynamics. It amplifies the significance of searching for the underlying mechanisms for the development of cell tissues and tumors invasion. In recent decades, a range of theoretical and computational methodologies have been developed to simulate the mechanics and dynamics of cellular tissue growth and to study the effect of cell mechanical properties on the interface scaling behavior of cell tissues.

For example, Block *et al.* discovered that the interface growth dynamics suggest a Kadar-Parisi-Zhang (KPZ)-like behavior across a broad range of parameters and for various cell migration mechanisms by studying the growth of 2D cellular monolayers using a class of cellular automaton (CA) growth models on an irregular lattice [77]. Azimzade *et al.* developed a tumor growth model based on the non-linear Fisher-Kolmogorov-Petrovsky-Piskunov equation and demonstrated that KPZ dynamics behavior is unable to characterize tumor invasion fronts due to the influence of the cellular environment and spatial correlations [91]. Santalla and Ferreira incorporated nutrient diffusion into a variant of the off-lattice Eden model [92]. They report a transition consistent with the qKPZ class at the pinning transition, from a transient KPZ-like behavior dynamics regime under limited nutrients to an unstable growth regime [92]. These results strengthen the hypothesis that the interface roughness behavior of cell colonies is diverse and cannot be classified by a well-known universality class.

The colony expansion dynamics of the aforementioned methods are based on stochastic differential equations or a stochastic master equation and do not account for the direct influence of cell mechanical properties, such as cell-cell friction and adhesion, on the scaling of the colony interface roughness. In this dissertation, we studied the effect of some of the cell's mechanical properties on the interface scaling behavior of cell colony expansion. We have studied the impact of mechanical factors, such as cell-cell adhesion, cell-medium friction, and intermembrane friction, as well as cell division rules, on the dynamics of cell population growth. These factors can influence the migration and collective motion of cells on the colonies borders, and thus surface diffusion. We showed that by changing some of these factors such as cell-cell adhesion strength, we can reproduce both KPZ-like and MBE-like behavior observed in the experimental studies. We also showed that they affect the kinetics of colony growth such as the colony growth rate. We also investigate the effect of environmental heterogeneity on the dynamics and kinetics of the cell colonies growth, and morphology of cell colonies. We demonstrated that in a medium with quenched disorder, the tissue interface has a lesser exponent for interface roughness and a larger exponent for growth. We observed that these scaling exponents of tissue interface also depend on the substrate's topology and cannot be classified by well-established universality classes. This effort to examine the effect of mechanical and biochemical factors on tissue growth and tumor invasion can aid in the identification of cell activities whose modification would result in the most potent inhibition of multicellular growth and invasion, thereby identifying potential molecular drug targets [77].

1.3 Thesis Outline

The remainder of this thesis is organized as follows:

Chapter 2 describes the theoretical background on surface analysis, which includes continuum theory and symmetry principles for the derivation of surface growth equations in Section 2.1, scaling arguments in Section 2.2, the renormalization group approach in Section 2.3, and a review on discrete growth models in Section 2.4.

Chapter 3 discusses the theoretical and computational aspects of the *CellSim3D* model, which includes a discussion on *CellSim3D* assumption in Section 3.1, force field and cell structure in Section 3.2, cell division mechanism in Section 3.3, cell apoptosis mechanism in Section 3.4, and *CellSim3D* structure and implementation in Section 3.5.

Chapter 4 presents *In silico* study of epithelial tissue growth, which includes an introduction to the subject in Section 4.1, a description of the model and surface roughness analysis in Section 4.2, the linear and radial interface roughness scaling results in Section 4.3, the conclusion in Section 4.4, and supplementary material in Section 4.5.

Chapter 5 describes *In silico* study of epithelial tissue growth dynamics in heterogeneous substrates with different topologies, which includes an introduction to the subject in Section 5.1, a description of the model in Section 5.2, the theory of the surface roughness analysis in Section 5.3, the linear and radial interface roughness scaling results in Section 5.4, and the conclusion in Section 5.5.

Finally, Chapter 6 concludes the thesis and discusses future work.

Chapter 2

Surface Growth in Nature

This chapter focuses on theories and methods for quantifying the roughness of a particular surface. To be more precise, we will see how the meaning of the surface roughness is expressed through exponents that incorporate scale changes. Surface roughness scaling behaviors are categorized by various scaling universality classes [6]. Several of these scaling universality classes, including Kardar-Parisi-Zhang (KPZ) [5] and Molecular Beam Epitaxy (MBE) [86], have been reported in experimental studies on the growth processes of biological systems. The cultivation of agar in a petri dish [81, 82], the expansion of healthy and cancerous cell colonies *in vivo* and *in vitro* [13, 4], and the expansion of cell colonies in a gel medium [83] are just some of the experimental studies on growth processes in biological systems that have been performed in recent decades.

This chapter discusses in depth the derivation and scaling behavior of these universality classes in order to better comprehend their significance in the growth of biological matter, such as bacterial colony growth and tumor invasion. We also discuss the physical mechanisms responsible for the time-dependent dynamics of a surface, including deposition, diffusion, and the propagation of a surface across heterogeneous environments. Intercellular interactions, nutrient concentrations, and the substrate's heterogeneity are just a few of the factors that influence a cell colony's expansion and interface roughness dynamics [81, 82, 13, 83].

The development of innovative methodologies with strong prediction ability is one of the primary objectives of research in any subject of study. In this chapter, we will briefly address the theoretical and computational approaches to studying surface growth processes and will not cover the details of the experimental techniques and equipment that have been developed for this purpose.

When we examine a particular surface growth problem for the first time, we initially attempt to derive a continuum growth equation. Utilizing stochastic differential equations is a valuable tool for understanding the dynamics of various growth processes. The continuum growth equation of a surface can be obtained by taking into account the surface's underlying symmetries. A surface is frequently characterized by an equation at large length scales. Hence, we can disregard details at shorter length scales and rely on asymptotic coarse-grained characteristics. In Section 2.1, we discuss the continuum theory in detail.

Roughness of a surface can be analyzed by determining the scaling exponents and scaling functions. A scaling-relation will lead us to categorize the universality scaling behavior of the processes. The universality class notion, developed in contemporary statistical mechanics, formalizes the observation that exponents describing the scaling behavior depend on just a small number of critical factors. In Section 2.2, we discuss the scaling method.

Another technique to study the scaling behavior of a surface is the renormalization group (RG) method. Since there are not any exact solutions for many equations, we have to use approximations to figure out the scaling behavior. RG is an especially useful technique that has been applied to various problems with great success, and is discussed in Section 2.3.

The study of surface scaling was motivated in part by computational modeling and simulation. Simulation studies allow us to discern between the important morphological variables and unnecessary aspects. For many processes, a relatively straightforward model is adequate. Modeling surfaces that arise as a result of basic processes can be accomplished using modern computer resources. Some of these numerical models are discussed in detail in Section 2.4.

2.1 Continuum Theory

The growth process can be viewed as occurring along a continuum perspective. Continuum approaches employ a coarse-grained viewpoint, viewing the entire domain as a single large area with multiple subunits. Continuum theory aims to describe the basic factors that determine surface growth while disregarding the atomistic features of a growth process. Continuum theory is able to overcome the challenge of having conflicting effects, such as deposition time in a growth process. To derive an appropriate continuum equation describing the roughening of a surface, one must have a thorough understanding of the underlying symmetries and conservation principles governing the growth process [6].

2.1.1 Symmetry Principle

The methods and ideas of near-equilibrium dynamics must be applied with caution to a wide variety of natural systems that display generic scale invariance and are far from equilibrium, such as a growing biological tissue [82, 93]. It is unknown whether or not a simple Hamiltonian governs the dynamics of such processes, hence, the conventional method may not be applicable. In the same vein as the development of an efficient coarse-grained field theory, there exists a generic strategy for studying the dynamics of these open and far from equilibrium systems.

In the setting of non-equilibrium dynamics, we will treat the equation of motion as the primary focus of attention. In the presence of dissipative dynamics, inertial terms lose their significance over sufficiently long time scales. To write a continuum equation of motion for the surface of a particular growth model, we consider that the equation of motion is the simplest equation that reflects the symmetries of the problem [94]. We construct an equation that characterizes the equilibrium surface, where equilibrium indicates that the surface is not being driven by an external field.

Assume that the height of a surface, represented by the function $h(\mathbf{x}, t)$, has a single value at any position $\mathbf{x}$, where $\mathbf{x}$ belongs to a d-dimensional substrate, so that no overhangs exist. This section's objective is to derive a generalized growth equation. Given the symmetry principles, we anticipate the growth equation to appear as follows [6]:

$$\partial_t h(\mathbf{x}, t) = F(h, \mathbf{x}, t) + \xi(\mathbf{x}, t), \tag{2.1}$$

where $\xi(\mathbf{x}, t)$ expresses the noise term and $F(h, \mathbf{x}, t)$ represents a general function that is time-, position-, and height-dependent. Whether the noise, $\xi(\mathbf{x}, t)$, is conservative or non-conservative depends on whether it is caused by internal reorganizations or external inputs and outputs. The function, $F(h, \mathbf{x}, t)$, at $\mathbf{x}$ and t requires only $h(\mathbf{x}, t)$ and low order spatial derivatives of $h(\mathbf{x}, t)$ due to the short-ranged interactions. In order to find the growth equation, it is necessary to identify the underlying symmetries of the problem. It is unnecessary to derive the function, $F(h, \mathbf{x}, t)$, from a potential, and there is no need to satisfy the fluctuation–dissipation condition [6].

The first symmetry to address is the time translation invariance of the surface. To verify that the growth equation is time-independent, it must be invariant under the transformation $t \longrightarrow t + \delta t$. Due to this symmetry, there can be no direct temporal dependence on F.

The second symmetry to take into account is the translational invariance along the growth direction. Therefore, the growth equation must be invariant under the translation $h \longrightarrow h + \delta h$, and the growth rule must be valid regardless of the point where $h = 0$. This symmetry precludes an explicit dependence of F on h; hence, the equation must be constructed using the combinations of the derivative of the height such as $\nabla h, \nabla^2 h, ..., \nabla^n h$.

Another symmetry to consider is the translational invariance in the direction perpendicular to the growth direction. Given that the equation has the symmetry $\mathbf{x} \longrightarrow \mathbf{x} + \delta\mathbf{x}$, it should be independent of the actual value of $\mathbf{x}$. This eliminates the requirement for F to explicitly depend on $\mathbf{x}$.

The rotational and inversion ($\mathbf{x} \longrightarrow -\mathbf{x}$) symmetry about the growth direction are another symmetries, eliminating derivatives of odd orders in the coordinates, such as ∇h, $\nabla(\nabla^2 h)$, etc.

Finally, in some surface growth phenomena, the fluctuations in surface height, h, relative to the mean surface height are similar in both directions. This symmetry is called Up/Down symmetry and can be checked by looking for the invariance under $h \longrightarrow -h$. Terms with even powers of h, such as $(\nabla h)^2$ and $(\nabla h)^4$, are therefore disallowed. This symmetry can be broken in non-equilibrium systems.

As an example, we consider the Edward-Wilkinson (EW) equation [85]. All possible combinations of powers of $\nabla^n h$ are taken into account to determine the final form of this growth equation, and each one that violates one of the aforementioned symmetries is removed. Hence, we have

$$\begin{aligned}\partial_t h(\mathbf{x},t) = \upsilon + \nabla^2 h(\mathbf{x},t) + \nabla^4 h(\mathbf{x},t) + ... + \nabla^{2n} h(\mathbf{x},t) + \nabla^2 h(\mathbf{x},t)\ (\nabla h(\mathbf{x},t))^2 + ...\\ + \nabla^{2k} h(\mathbf{x},t)\ (\nabla h(\mathbf{x},t))^{2j} + \xi(\mathbf{x},t),\end{aligned}$$

where each of n, k, and j may be any positive integer. The velocity term, υ, is possible if the surface is moving at a speed greater than zero. The scaling features of the surface are unaffected by this uniform motion created by the velocity term. This term can be transferred away by defining the process in a coordinate system moving at speed υ, using the transformation $h \longrightarrow h + \upsilon t$. We are mainly interested in the long-time, $t \longrightarrow \infty$, and long-distance, $x \longrightarrow \infty$, behavior of the surface-defining functions. Simple scaling arguments or a more sophisticated RG calculation will confirm that under this hydrodynamic limit, higher order derivatives are irrelevant terms and less significant than lower order derivatives.

As an illustration, we demonstrate that $\nabla^4 h$ approaches zero faster than $\nabla^2 h$ term. Therefore, it is an irrelevant term that has no effect on the scaling exponents. Using the scale transformation $\mathbf{x} \longrightarrow \mathbf{x}' \equiv b\mathbf{x}$, where the coarsening factor $b > 1$. Assuming that the surface has a roughness exponent α, we need to rescale the height using the formula $h \longrightarrow h' \equiv b^{\alpha} h$ to obtain a surface with similar geometric properties. Therefore we have $\nabla^2 h \longrightarrow \nabla'^2 h' \equiv b^{\alpha-2}\nabla^2 h$ and $\nabla^4 h \longrightarrow \nabla'^4 h' \equiv b^{\alpha-4}\nabla^4 h$. Hence, in the hydrodynamic limit, the term $\nabla^4 h$ and similar terms with higher order derivatives go faster to zero than $\nabla^2 h$. With the same arguments, we can show that all terms like $\nabla^{2k} h\ (\nabla h)^{2j}$ approach zero faster than $\nabla^2 h$ and are irrelevant in scaling analysis [6].

The randomness of the fluctuation process is introduced with Gaussian white noise given by $\langle \xi(\mathbf{x}, t)\rangle = 0$ and $\langle \xi(\mathbf{x}, s)\xi(\mathbf{x}', t)\rangle = 2D\delta(s-t)\delta^d(\mathbf{x}-\mathbf{x}')$. Hence, in the simplest terms, the EW equation represents equilibrium surface fluctuations with the form [85].

$$\partial_t h(\mathbf{x}, t) = \nu \nabla^2 h(\mathbf{x}, t) + \xi(\mathbf{x}, t), \tag{2.2}$$

where ν is commonly referred to as the surface tension, as the $\nabla^2 h$ term tends to make the surface smoother.

2.1.2 Kardar-Parisi-Zhang Equation

When looking into how particle deposition can affect the growth of surfaces, the EW equation is the simplest continuum equation [6]. When non-linear factors are introduced into the growth equation, the linear approximation no longer holds true. Non-linear terms were proposed as an addition to the EW equation by Kardar, Parisi, and Zhang [5]. The KPZ equation is a non-linear and unsolvable equation in closed form. Hence, scaling properties and exponents can only be derived via approximation approaches, such as RG. We present a description of the KPZ equation and highlight its key features. We will attempt to generalize the EW equation using both physical rules, which motivate the addition of non-linear terms to the linear theory, and symmetry principles. We assume that our system is capable of lateral expansion, which implies that growth occurs in the direction of the local normal to the surface, which is excluded in the EW equation due to the Up/Down symmetry. To include lateral growth to the EW equation, Eq. 2.2, we could add a new particle that is locally normal to the surface [6]. This

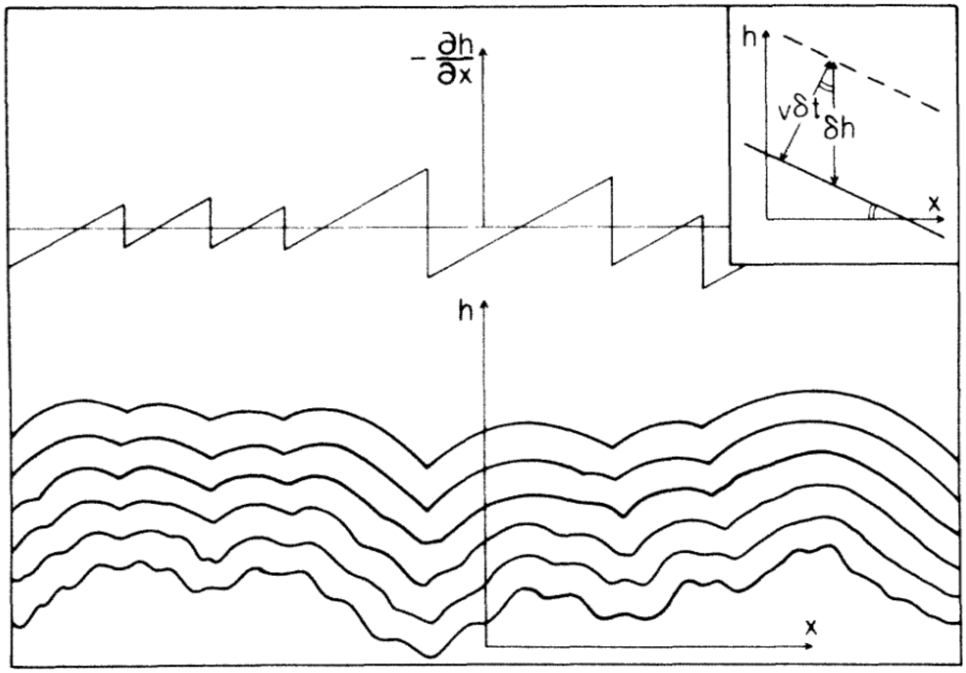

Figure 2.1: Deterministic growth curves that follow a specific pattern, as described by the KPZ equation. The inset demonstrates how lateral growth occurs locally along the surface normal. Image taken from Ref. [5] with permission from the American Physical Society (APS) Journals.

would result in an increase along the h axis, which would be, see Fig. 2.1:

$$\delta h = v\delta t\left[1 + (\nabla h)^2\right]^{\frac{1}{2}}, \tag{2.3}$$

for $|\nabla h| \ll 1$, we can expand the previous equation as

$$\frac{\delta h}{\delta t} \approx v + \frac{v}{2}(\nabla h)^2. \tag{2.4}$$

Using this approximated term to describe the lateral growth, the EW equation, Eq. 2.2, can be generalized as follows:

$$\partial_t h(\mathbf{x}, t) = \nu\nabla^2 h(\mathbf{x}, t) + \frac{\lambda}{2}(\nabla h(\mathbf{x}, t))^2 + \xi(\mathbf{x}, t), \tag{2.5}$$

where relaxation of the surface due to surface tension, ν, is described by the first term on the right side of the equation, and the second term is the non-linear term resulting from lateral growth. The noise term has the same properties as in the EW equation.

The KPZ equation can also be derived using symmetry principles. We include all the symmetries used to derive the EW equation, Eq. 2.2, except the Up/Down symmetry. By violating the Up/Down symmetry of the surface height $h(x, t)$, we are able to construct the KPZ equation, Eq. 2.5, which indicates that the surface is not invariant under the transformation, $h \rightarrow -h$. For example, the presence of a driving force perpendicular to the surface, which dictates a certain growth direction for the surface, is a necessary condition for this symmetry breakdown. Due to the Up/Down symmetry, terms such as $(\nabla h)^{2n}$ are inapplicable to the EW growth equation. The KPZ equation, Eq. 2.5, is generated by adding to the EW equation, Eq. 2.5, the lowest order element of this type, represented as $(\nabla h)^2$ [6].

In the absence of a driving force, the average velocity evaluated using the EW equation, Eq. 2.2, will be zero because the integral of the Laplacian term under periodic boundary conditions is zero. However, the non-linear term in the KPZ equation, Eq. 2.5, assures that the average velocity is larger than zero, and only when the surface is perfectly flat does it equal zero. The surface average velocity is defined as follows:

$$v = \int_0^L \langle \partial_t h(\mathbf{x}, t) \rangle \, d\mathbf{x} = \frac{\lambda}{2} \int_0^L \langle (\nabla h(\mathbf{x}, t))^2 \rangle \, d\mathbf{x}. \tag{2.6}$$

With the help of a Cole–Hopf transformation [95, 96], the non-linear KPZ equation, Eq.2.5, can be linearized [97]. If we define the function $W(\mathbf{x}, t)$ as follows:

$$W(\mathbf{x}, t) = \exp\left\{-\frac{\lambda}{2\nu} h(\mathbf{x}, t)\right\}, \tag{2.7}$$

where ν and λ are the surface tension and the nonlinear parameter, respectively. The evolution of the function W is governed by the diffusion equation with multiplicative noise,

$$\partial_t W(\mathbf{x}, t) = \nu \nabla^2 W(\mathbf{x}, t) + \frac{\lambda}{2\nu} W(\mathbf{x}, t) \xi(\mathbf{x}, t). \tag{2.8}$$

In the absence of the noise, $\xi(\mathbf{x}, t) = 0$, this equation can be solved to determine the growth profile for a given initial state, $W(\mathbf{x}, t = 0) = \exp\{-\frac{\lambda}{2\nu} h_0(\mathbf{x})\}$. Using the inverse of Eq. 2.7, we can write the answer as follows: [97]

$$h(\mathbf{x}, t) = \frac{\lambda}{2\nu} \ln\{\int d^d\mathbf{x}' \exp[-\frac{|\mathbf{x} - \mathbf{x}'|^2}{2\nu t} + \frac{\lambda}{2\nu} h(\mathbf{x}, t)]\}. \tag{2.9}$$

Moreover, by using $\mathbf{u}(\mathbf{x}, t) = -\lambda \nabla h(\mathbf{x}, t)$, we can demonstrate that the KPZ equation can be transformed into the stochastic Burgers' equation [98, 99], which is a simple description of the generation of shock waves in a fluid [100],

$$\partial_t \mathbf{u}(\mathbf{x}, t) + \mathbf{u}(\mathbf{x}, t) \cdot \nabla \mathbf{u}(\mathbf{x}, t) = \nu \nabla^2 \mathbf{u}(\mathbf{x}, t) - \lambda \nabla \xi(\mathbf{x}, t). \tag{2.10}$$

2.1.3 Quenched Kardar-Parisi-Zhang Equation

When it comes to characterizing the behavior of a driven surface, the KPZ equation is the most general form. Assume that in a porous media, a vertical driving force F is applied to a surface that resembles a spatially expanded string that, due to surface tension, tends to stay straight and not tangle. The disorder in the porous media subsequently applies an inhomogeneous frictional force to the surface and pins a portion of it. The quenched in noise caused by the disorder is more prominent than the thermal noise in a disordered medium. As a result, the expression $\xi(\mathbf{x}, t)$ for thermal noise has been superseded by the expression $\eta(\mathbf{x}, h)$ for quenched noise [101, 102]. The quenched KPZ (qKPZ) equation is as follows [103]:

$$\partial_t h(\mathbf{x}, t) = \nu \nabla^2 h(\mathbf{x}, t) + \frac{\lambda}{2} (\nabla h(\mathbf{x}, t))^2 + \eta(\mathbf{x}, h). \tag{2.11}$$

As with thermal noise, we assume that the average quenched noise is also zero, $\langle \eta(\mathbf{x}, h) \rangle = 0$. Here, the angle brackets stand for an average over different random realizations. The correlation has the following form:

$$\langle \eta(\mathbf{x}, h)\eta(\mathbf{x}', h')\rangle = \delta^d(\mathbf{x} - \mathbf{x}')\Delta(h - h'), \tag{2.12}$$

where $\Delta(u)$ is a monotonically decreasing function of u with the condition $\Delta(u) = \Delta(-u)$. The Dirac delta function, $\delta(u)$, is a particular instance of this function and is referred to as random field disorder [6, 104]. The KPZ equation, Eq. 2.5, is a stochastic differential equation. Therefore, even if the surface is restarted from identical initial conditions, it will end up in a different state every time. On the other hand, if we run our simulation repeatedly, beginning with the identical conditions for a quenched disordered system, we always end up with the same surface [105, 101].

For the quenched KPZ (qKPZ) equation, we will be confronted with a variety of different circumstances based on the strength of the driving force. In the absence of the driving force or a weak driving force, the surface will continue to travel until it becomes immobilized and achieves a configuration with a local minimum energy. At a critical force, F_c, the driving force is able to overcome the pinning force due to the disorder, and the surface begins to move with a finite velocity. Slightly above F_c, when the driving and elastic forces are strong enough to overcome the pinning forces in one region, the surface progresses, only to be stopped again by another region of strong pinning sites. Hence, the surface motion is not uniform and consists of a combination of slow and smooth motion and abrupt jumps. Lastly, if the driving force is much larger than F_c, a rapidly fluctuating noise is experienced at the surface. In this domain, the KPZ equation, Eq. 2.5, adequately characterizes the motion, and thermal fluctuations eliminate the influence of quenched randomness [6].

In the zero-temperature limit, where thermal noise is small, Eq. 2.11 describes the system. In spite of this, thermal noise is usually present in experiments. Thus, we generalize this equation to include both quenched noise, $\eta(\mathbf{x}, h)$, and thermal noise, $\xi(\mathbf{x}, t)$, as follows:

$$\partial_t h(\mathbf{x}, t) = \nu\nabla^2 h(\mathbf{x}, t) + \frac{\lambda}{2}(\nabla h(\mathbf{x}, t))^2 + \eta(\mathbf{x}, h) + \xi(\mathbf{x}, t). \tag{2.13}$$

Thermal noise can influence the mobility of the surface close to and below the depinning transition [106, 107]. It is plausible that the quenched disorder has trapped the surface in a local potential minimum. Since the velocity of the surface at zero temperature is zero, it will remain at the local minimum forever. However, at temperatures greater than absolute zero, thermal noise can assist the surface in overcoming the potential barriers [6].

2.1.4 Molecular Beam Epitaxy Equation

Poor contact properties of rough semiconductor or metal surfaces can render them practically unusable for electronic purposes. Therefore, the great majority of experiments explore surfaces with high contact characteristics, avoiding roughening wherever possible. However, even with advanced experimental tools, roughening is frequently unavoidable. A greater understanding of the roughening process might assist in identifying the experimental and technological limits of what is achievable, which could lead to the development of strategies for managing surface roughness. Scaling laws and continuum theory in the contexts of molecular beam epitaxy (MBE) have received an increasing amount of interest from both theorists and experimentalists [108, 109].

In this section, we will analyze how the continuum theory describes the MBE equation, Eq. 2.18, by including the effects of deposition, desorption, and surface diffusion. First, we focus on linear terms which are sufficient for describing many important phenomena. Finally, the non-linear contributions will be added to the MBE equation [6].

Surface diffusion of the deposited particles is the underlying physical mechanism that sets molecular beam epitaxy (MBE) apart from other growth techniques [110, 111, 112]. We begin by discussing a variety of approaches to including surface diffusion in the growth equations. In order to formulate a continuous equation that accounts for fluctuations in surface height, $h(\mathbf{x}, t)$, the following steps must be taken. We consider a continuous equation of the following form:

$$\partial_t h(\mathbf{x}, t) = F(h, \mathbf{x}, t) + \xi(\mathbf{x}, t). \tag{2.14}$$

We disregard desorption in our original model, hence, atoms deposit on the surface and then disperse. The total number of particles does not change during the diffusion process. Upon diffusing over the surface, the diffusing particles generate a macroscopic current that is perpendicular to the normal direction of the surface. This current, denoted by $\mathbf{j}(\mathbf{x}, t)$, follows the continuity equation [6].

$$\partial_t h(\mathbf{x}, t) = -\nabla \cdot \mathbf{j}(\mathbf{x}, t). \tag{2.15}$$

We can relate the surface current to the variations in the local chemical potential based on the first Fick's law as follows:

$$\mathbf{j}(\mathbf{x}, t) \propto -\nabla \mu(\mathbf{x}, t). \tag{2.16}$$

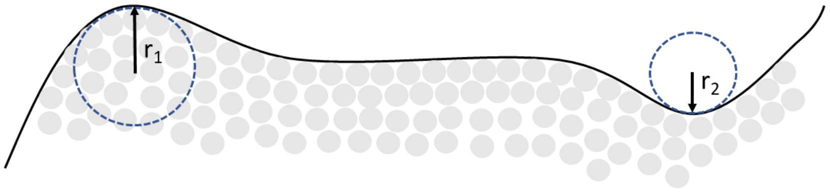

Figure 2.2: Surface local geometries are depicted schematically. It is energetically unfavorable for an atom to remain on top of the surface with the local hill, which has a positive chemical potential and, consequently, a negative local Laplacian. At the local valley, the local Laplacian, which is the inverse of the radius r_2 of the circle that fits the surface locally, is positive, corresponding to a negative chemical potential. Lastly, on a flat surface, the chemical potential of an atom is zero, and the radius, R, of the circle is infinite.

To calculate the local chemical potential, we assume that the mobility of an atom does not depend on the local height of the surface, but on the number of bonds that must be broken for diffusion. The local curvature of the surface determines the number of bonds an atom may form at a specific position. If R, the local radius of curvature, is positive, then the atom is surrounded by a large number of other atoms. Instead, if R is negative, the atom is separated from its environment and can diffuse easily, see Fig. 2.2. The simplest assumption is that the chemical potential regulating the probability of diffusion is proportional to $-\frac{1}{R}$, which is proportional to $\nabla^2 h(\mathbf{x},t)$. This result could also be achieved using a simple symmetry argument [6]. Hence, we find the equation characterizing surface diffusion relaxation as

$$\partial_t h(\mathbf{x},t) = -\nabla^4 h(\mathbf{x},t). \tag{2.17}$$

The deposition process is random because the intensity of the atomic beam changes. Random fluctuation, $\xi(\mathbf{x},t)$, at the surface is described by Gaussian noise given by $\langle\xi(\mathbf{x},t)\rangle = 0$, and $\langle\xi(\mathbf{x},s)\xi(\mathbf{x}',t)\rangle = 2D\delta(s-t)\delta^d(\mathbf{x}-\mathbf{x}')$. For the purpose of adding this randomness into the MBE growth equation, we think of the deposition flux as being made up of the average flux of the incoming particles, $F(\mathbf{x},t)$, and the noise, $\xi(\mathbf{x},t)$. Wolf and Villain [113], and Das Sarma and Tamborenea [114] introduced independently the stochastic MBE growth equation that includes both surface diffusion and deposition as

$$\partial_t h(\mathbf{x},t) = -K\nabla^4 h(\mathbf{x},t) + \xi(\mathbf{x},t). \tag{2.18}$$

There are models of growth in which the scaling behavior is determined by non-linear terms [112, 111]. There is no reason to exclude the possibility of non-linear terms in the MBE equation, Eq. 2.18, when surface diffusion is the dominating mechanism. In the following lines, the significance of non-linear components will be studied.

To derive the relevant non-linear term for the MBE equation, symmetry arguments are applied. Here, we extend the MBE equation to include all relevant non-linear variables and filter out those that do not satisfy the fundamental symmetry restrictions of the growth process. Our objective is to find an equation that is rotationally symmetric and has inversion symmetry, $\mathbf{x} \to -\mathbf{x}$, thereby eliminating the necessity for odd-order spatial derivatives. Additionally, it must maintain translational invariance along the growth axis, $h \longrightarrow h+\delta h$, and its perpendicular, $\mathbf{x} \longrightarrow \mathbf{x} + \delta\mathbf{x}$ directions.

Any non-linear component in a diffusion-dominated growth process must also meet the continuity equation, which states that permissible terms must maintain a constant number of particles at the surface. This condition eliminates, for instance, the KPZ non-linear lateral growth term, which cannot be described as the gradient of a current. As a result, the generalized linear MBE equation has the form

$$\partial_t h(\mathbf{x}, t) = -K\nabla^4 h(\mathbf{x}, t) + \lambda_1 \nabla^2 (\nabla h(\mathbf{x}, t))^2 + \lambda_2 \nabla \cdot (\nabla h(\mathbf{x}, t))^3 + \xi(\mathbf{x}, t), \tag{2.19}$$

where terms up to the fourth order spatial derivatives are taken into account [111]. The non-linear term $\nabla^2(\nabla h)^2$, also known as the conserved KPZ term, is represented by the current $\mathbf{j} \sim \nabla(\nabla h)^2$ [115]. The non-linear term $\nabla \cdot (\nabla h)^3$, which is represented by the current $-(\nabla h)^3$, cannot be described as a gradient of a chemical potential. We will not elaborate on the λ_2 term because no physical process has been identified for its generation [111]. Nevertheless, the λ_2 term is more relevant than the λ_1 term, and it has been argued that it represents a higher-order surface tension correction [6].

2.2 Scaling Arguments

Surface growth phenomena are influenced by a wide variety of factors. In surface growth studies, scientists always assume that the morphology and dynamics are regulated by a handful of basic rules. The evolution of a surface can be described qualitatively. To define a surface, we can construct a scenario in which particles assemble in columns on top of one another. We then offer two new functions for qualitatively describing the surface. The first useful function is the average surface height, which for a one-dimensional surface is defined as [6]

$$\bar{h}(t) \equiv \frac{1}{L}\sum_{i=1}^{L} h(i,t), \tag{2.20}$$

where $h(i,t)$ represents the height of column i at time t and L is the total number of columns. Given a constant rate of deposition, the average height of a system will increase linearly over time,

$$\bar{h}(t) \sim t. \tag{2.21}$$

The surface width function is another useful function. We measure the roughening process specifically by measuring the surface width over time. The width of the surface is determined by the root-mean-square (rms) fluctuation in the surface's height,

$$w(L,t) \equiv \sqrt{\frac{1}{L}\sum_{i=1}^{L}[h(i,t) - \bar{h}(t)]^2}. \tag{2.22}$$

The value of $w(L,t)$ on a surface shows power law behavior as t approaches the roughness saturation time,

$$w(L,t) \sim t^{\beta} \qquad t \ll t_s, \tag{2.23}$$

where t_s is the roughness saturation time, and the growth exponent, β, characterizes the time-dependent dynamics of the roughening process. At saturation time, t_s, at a constant surface length, L, the surface roughness saturates. This saturation value changes based on the length L of the surface and increases with L as [116]

$$w(L,t) \sim L^{\alpha} \qquad t \gg t_s. \tag{2.24}$$

There is a third critical exponent, z, that characterizes the scaling connection between the critical length and time scale. This critical exponent also depends on the system size and is given as

$$t_s \sim L^z. \tag{2.25}$$

These critical exponents are not independent, and the relationship between them is

$$z = \frac{\alpha}{\beta}. \tag{2.26}$$

The width function possesses the Family-Vicsek scaling relation as follows [117, 118]:

$$w(l,t) \sim t^{\beta} F(l t^{-\frac{1}{z}}), \tag{2.27}$$

where l is a local length of the surface and $F(u)$ is a u-dependent scaling function represented as

$$F(u) = \begin{cases} \text{const} & \text{if } u \gg 1; \\ u^{\beta} & \text{if } u \ll 1. \end{cases} \tag{2.28}$$

Scaling behavior may be understood through the width function's scaling relation and expressed in fractal notation. The single-valued functions known as self-affine functions define a type of anisotropic fractals that we find particularly useful for measuring disordered surfaces [119]. The surface width function is a self-affine function. Scaling relation of a self-affine function, $h(x)$, can be expressed as:

$$h(x) \sim b^{-\alpha} h(bx), \tag{2.29}$$

where α is known as the Hölder exponent, or self-affine exponent, and provides a numerical value for the roughness of the function $h(x)$. This indicates that the vertical and horizontal scaling factors for $h(x)$ are not the same. The transformation is isotropic and the system is self-similar if and only if $\alpha = 1$. In the following, we will estimate the scaling exponents of the surfaces for the various continuity equations stated above by making use of the self-affinity features of the surfaces [6].

2.2.1 Kardar-Parisi-Zhang Scaling

By applying the scale transformation $\mathbf{x} \longrightarrow b\mathbf{x}$ and rescaling the height as $h \longrightarrow b^{\alpha}h$ and the time as $t \longrightarrow b^{z}t$, the KPZ growth equation is modified to [5]:

$$b^{\alpha-z}\partial_t h(\mathbf{x},t) = \nu b^{\alpha-2}\nabla^2 h(\mathbf{x},t) + \frac{\lambda}{2}b^{2\alpha-2}(\nabla h(\mathbf{x},t))^2 + b^{-d/2-\alpha/2}\xi(\mathbf{x},t). \tag{2.30}$$

The non-linear term is larger than the surface tension term in the limit $b \longrightarrow \infty$, as shown by comparing $b^{2\alpha-2}(\nabla h)^2$ and $b^{\alpha-2}\nabla^2 h$. This demonstrates that the non-linear term is indeed a relevant term, and hence influences the scaling exponents. Multiplying both sides by $b^{z-\alpha}$, we can simplify the equation as

$$\partial_t h(\mathbf{x},t) = \nu b^{z-2}\nabla^2 h(\mathbf{x},t) + \frac{\lambda}{2}b^{\alpha+z-2}(\nabla h(\mathbf{x},t))^2 + b^{-d/2+z/2-\alpha}\xi(\mathbf{x},t), \tag{2.31}$$

where we used the following property of the delta function

$$\delta^d(a\mathbf{x}) = \frac{1}{a^d}\delta^d(\mathbf{x}), \tag{2.32}$$

where $\mathbf{x}$ is a d-dimensional vector, and as a result, we have

$$\begin{aligned}\langle \xi(b\mathbf{x}, b^z t)\xi(b\mathbf{x}', b^z t')\rangle = 2D\delta^d(b\mathbf{x} - b\mathbf{x}')\delta(b^z t - b^z t') = \\ 2Db^{-d-z}\delta^d(\mathbf{x} - \mathbf{x}')\delta(t - t').\end{aligned} \tag{2.33}$$

To ensure scaling invariance, it can be assumed that the right hand side of the equation must be unaffected by the factor b. However, by providing different scaling relations for α and z, this technique overdetermines them. By assuming the limit in which the non-linear term has a large impact on the surface tension, and $\nu\nabla^2 h$ term can be disregarded, we can find the following exponents that leave the right hand side of the equation unaffected by the scaling factor b in the absence of the surface tension term [5, 6]:

$$\alpha = \frac{2-d}{3}, \quad \beta = \frac{2-d}{4+d}. \tag{2.34}$$

Simulation and experiment results do not match these theoretical values [120, 121, 122, 123]. The various variables (ν, λ, and D) in the growth equation are connected to one another, therefore they do not renormalize independently upon rescaling. Later in this chapter, when we talk about the renormalization group method, we explore this issue in further detail.

2.2.2 Molecular Beam Epitaxy Scaling

We can derive an exact solution to the linear MBE growth equation, Eq. 2.18, by employing the Fourier transform. However, since the scaling characteristics of the system are of the utmost importance, we can derive the exponents using relatively simple scaling arguments. Multiplying both sides of the linear MBE growth equation by $b^{z-\alpha}$ after doing scaling of $\mathbf{x}$, t, and h yields

$$\partial_t h(\mathbf{x},t) = -Kb^{z-4}\nabla^4 h(\mathbf{x},t) + b^{\frac{z-d-2\alpha}{2}}\xi(\mathbf{x},t). \tag{2.35}$$

We can find the exponents by considering the self-affinity of the surface [6],

$$z = 4, \quad \alpha = \frac{4-d}{2}, \quad \beta = \frac{4-d}{8}. \tag{2.36}$$

Large roughness exponents, $\alpha = 3/2, 1$ for $d = 1, 2$, respectively, serve as an early warning of the potential influence of non-linear factors. In Section 2.3, we will examine the impact of non-linear terms on the scaling exponents.

2.3 Renormalization Group Method

The objective of the RG method is to preserve the physical aspects of interest while re-expressing the problem's defining parameters in terms of another simpler set. In the critical phenomena, when long-distance physics is desirable, this may be achieved by coarsening the short-range degrees of freedom [97, 124, 125, 126, 127].

An easy way to construct a perturbation series when using the RG on non-linear Langevin equations is to first recast the dynamical problem into a form similar to the field-theoretic description of equilibrium statistical mechanics, and then to use the well-established machinery of the RG. We begin by constructing a dynamic response functional from a non-linear Langevin equation, followed by a conceptual discussion of the RG method.

2.3.1 Dynamic Janssen–De Dominicis Response Functional

To employ the well-established framework of quantum field theory, we must first transform the dynamical problem into a form analogous to the field-theoretic description of equilibrium statistical mechanics [124]. We begin by looking at dynamical equations of motion of the Langevin type for coarse-grained stochastic field variables $h(\mathbf{x},t)$ of the form

$$\partial_t h(\mathbf{x},t) = F(h(\mathbf{x},t),\mathbf{x},t) + \xi(\mathbf{x},t), \tag{2.37}$$

where $F(h(\mathbf{x},t),\mathbf{x},t)$ represents a general function that is height-, position-, and time-dependent, and the stochastic noise $\xi(\mathbf{x},t)$ represent the influence of fast degrees of freedom; its mean is zero as before, $\langle\xi(\mathbf{x},t)\rangle = 0$, and its second moment is assumed to be defined by diagonal white noise $\langle\xi(\mathbf{x},s)\xi(\mathbf{x}',t)\rangle = 2L\delta(s-t)\delta^d(\mathbf{x}-\mathbf{x}')$. We substitute L for D and use D as the functional measure in the functional integrals in this section. If we can demonstrate that the noise correlation derives from a probability distribution, this dynamical problem can be transformed into a field-theoretic description of equilibrium statistical mechanics. We can construct a probability distribution for the noise using the following Gaussian integral formulas

$$\int e^{-\frac{\xi(\mathbf{x},t)L^{-1}\xi(\mathbf{x},t)}{4}}\,d\mathbf{x} = 2\,(\pi L)^{\frac{1}{2}} \quad \text{and} \tag{2.38}$$

$$\int \xi^2(\mathbf{x},t)\,e^{-\frac{\xi(\mathbf{x},t)L^{-1}\xi(\mathbf{x},t)}{4}}\,d\mathbf{x} = 4L\,(\pi L)^{\frac{1}{2}}\,. \tag{2.39}$$

where we consider that the noise strength, L, can be an operator, and its inverse is regarded as a Green's function. The noise probability distribution can then be written as follows:

$$W(\xi(\mathbf{x},t)) \propto \exp\left(-\frac{1}{4}\int d\mathbf{x}\int dt\,\xi(\mathbf{x},t)L^{-1}\xi(\mathbf{x},t)\right). \tag{2.40}$$

We can also write this function in Fourier space. Hence the exponent is of the form, $-\int_{\mathbf{q},\omega}\frac{|\xi(\mathbf{q},\omega)|^2}{4L\mathbf{q}^2}$. Now, we can obtain a probability distribution $P[h]$ for the field $h(\mathbf{x},t)$ by interpreting the noise as a functional of the field $h(\mathbf{x},t)$, whose relationship is defined by the Langevin equation, $\partial_t h(\mathbf{x},t) - F(h(\mathbf{x},t),\mathbf{x},t) = \xi(\mathbf{x},t)$.

$$W[\xi]D[\xi] = P[h]D[h] \propto e^{-G[h]}D[h]. \tag{2.41}$$

The derivation of the functional determinant, $D[\xi]/D[h]$, resulting from this non-linear variable transformation can be found in Ref. [124]. Here, $G[h]$ is the Onsager–Machlup functional [128]

$$G[h] = \frac{1}{4}\int d\mathbf{x}\int dt\,(\partial_t h(\mathbf{x},t) - F(h(\mathbf{x},t),\mathbf{x},t))\,(L)^{-1}\,(\partial_t h(\mathbf{x},t) - F(h(\mathbf{x},t),\mathbf{x},t))\,. \tag{2.42}$$

which is identical to the Hamiltonian, H, in equilibrium statistical mechanics, as it defines the statistical weight of a particular configuration, $h(\mathbf{x},t)$. However, assuming that the noise probability distribution is properly normalized, the partition function is unity and the associated free energy is zero. This equation yields a basis for perturbational expansion and is the preferred field-theoretic formulation of non-linear Langevin dynamics from a theoretical standpoint. However, this formulation is difficult to deal with due to the development of the inverse of the operator L in the Onsager-Machlup functional, which, for example, results in a singularity as $\mathbf{q} \to 0$ in the case of conserved dynamics, $L \sim \mathbf{q}^2$ [124]. To overcome this issue, we can apply the Hubbard–Stratonovich transformation [129] to transfer the inverse of the operator L to the operator L. We know that the average of the observable A over the noise is

$$\langle A[h] \rangle_\xi \propto \int D[\xi]\, A[h(\xi)]\, W[\xi], \tag{2.43}$$

where we also need to force that the fields obey the Langevin dynamics by inserting a convoluted unity at each spacetime point [124].

$$\begin{aligned} 1 &= \int D[h] \prod_{(\mathbf{x},t)} \delta\left(\partial_t h - F(h, \mathbf{x}, t) - \xi\right) \\ &= \int D[i\tilde{h}] \int D[h] \exp\{-\int d\mathbf{x} \int dt\, \tilde{h}\left(\partial_t h - F(h, \mathbf{x}, t) - \xi\right)\}, \end{aligned} \tag{2.44}$$

where functional integral representation of the delta function was employed. The new field, $\tilde{h}(\mathbf{x}, t)$, is called the Martin–Siggia–Rose auxiliary fields [130], commonly known as a response field. Using this integral, the average of an operator A over the noise can be expressed as follows:

$$\begin{aligned} \langle A[h] \rangle_\xi \propto \int D[i\tilde{h}] \int D[h] \exp\Big\{-\int d\mathbf{x} \int dt\, \tilde{h}\left(\partial_t h - F(h, \mathbf{x}, t)\right)\Big\} \\ \times A[h] \int D[\xi] \exp\Big\{-\int d\mathbf{x} \int dt\, \left(\xi L^{-1} \xi - \tilde{h}\, \xi\right)\Big\}, \end{aligned} \tag{2.45}$$

where the second line can be evaluated as a completed square Gaussian integral. This average formula reveals the subsequent probability distribution for stochastic field variables, $h(\mathbf{x}, t)$, as

$$P[h] = C^{-1} \int D[i\tilde{h}]\, e^{-A(h, \tilde{h})}, \tag{2.46}$$

with the normalization constant

$$C = \int D[h] \int D[i\tilde{h}]\, e^{-A(h,\tilde{h})}, \tag{2.47}$$

where $A[h, \tilde{h}]$ is the dynamic Janssen–De Dominicis response functional [124]

$$A[h, \tilde{h}] = \int d\mathbf{x} \int dt\, \{\tilde{h}\, (\partial_t h - F(h, \mathbf{x}, t)) - \tilde{h}\, L\, \tilde{h}\}. \tag{2.48}$$

In a field theoretic framework, the resulting dynamic Janssen-De Dominicis response functional can serve as the action that can be used as a starting point for applying the RG technique.

2.3.2 Momentum Shell Renormalization Group

Kadanoff promoted employing the self-similarity of the fluctuations to remove the correlated degrees of freedom at small length scales, leaving only the simple, uncorrelated degrees of freedom at a length scale comparable to the correlation length scale of the system [131]. In condensed matter physics, RG can be done in both real and momentum space. The RG method consists of three distinct processes.

Coarsening, which is the process of removing short-scale fluctuations, is the initial stage in the RG procedure. The shortest scale of the system is determined by the shortest distance between two points in space where the field can change its value. This is the minimum scale underlying models such as the Landau-Ginzburg Hamiltonian or the lattice spacing for the spin-like models [97, 125]. The initial stage of the RG procedure is to reduce the spatial resolution by altering minimum scale a to ba, where $b > 1$. Following coarsening, the new field, $\vec{h}(\mathbf{x})$ is

$$\vec{h}(\mathbf{x}) = \frac{1}{b^d} \int_{\text{box centered at } x} d^d\mathbf{x}'\, \vec{h}'(\mathbf{x}), \tag{2.49}$$

where the coarse-grained space is grainier than the original one since the shortest spatial scale has been increased.

In the second stage, we rescale the space to bring the system back to its original minimum length scale. This process is referred to as rescaling. Reduce all length scales by a factor of b, and the original minimum scale of the system will be recovered as

$$\mathbf{x}_{\text{new}} = \frac{\mathbf{x}_{\text{old}}}{b}. \tag{2.50}$$

The RG procedure culminates with the renormalization of the field. In general, the rescaled field profile's fluctuations differ from those of the original. To fix this, a renormalized field is defined, resulting in a reduction of the field strength by a factor ζ. Following these procedures, we obtain a renormalized configuration, $\vec{h}_{\text{new}}(\mathbf{x})$, from any given configuration, $\vec{h}_{\text{old}}(\mathbf{x})$, as [97]

$$\vec{h}_{new}(\mathbf{x}) = \frac{1}{\zeta\, b^d} \int_{\text{box centered at } b\mathbf{x}_{\text{new}}} d^d\mathbf{x}'\, \vec{h}'_{\text{old}}(\mathbf{x}). \tag{2.51}$$

This equation can be used to construct the probability distribution, or weight W, by imagining it as a mapping between two sets of random variables.

Now, we will describe each of these steps in the momentum-space. The momentum-space RG can be used for systems whose degrees of freedom are described as Fourier modes of a certain field. We define $\vec{h}(\mathbf{q})$ as the Fourier transfer of the field $\vec{h}(\mathbf{x})$. Because the shortest length scales are associated with the largest wavenumbers, filtering out variations on short length scales in the real space renormalization group is comparable to extracting high momentum modes in the Fourier space by integration. The elimination of fluctuations at scales $a < x < b\,a$ is equivalent to the suppression of Fourier modes with wavenumbers $\frac{\Lambda}{b} < q < \Lambda$ [97, 125]. Consequently, the wavevector space is split into two subspaces,

$$\{\vec{h}(\mathbf{q})\} = \{\vec{\sigma}(\mathbf{q}^{>})\} \bigoplus \{\tilde{\vec{h}}(\mathbf{q}^{<})\}, \tag{2.52}$$

where $\mathbf{q}^{>}$ and $\mathbf{q}^{<}$ stand for $\frac{\Lambda}{b} < \mathbf{q} < \Lambda$ and $\mathbf{q} < \frac{\Lambda}{b}$, respectively, and $\bigoplus$ is the direct sum between two subspaces [97]. The new fields $\vec{\sigma}(\mathbf{q}^{>})$ and $\vec{h}(\mathbf{q}^{<})$ are the functions of $\mathbf{q}^{>}$ and $\mathbf{q}^{<}$, respectively. Consequently, we may formulate the partition function, Z, as follows:

$$Z = \int D\tilde{\vec{h}}(\mathbf{q}^{<}) \int D\vec{\sigma}(\mathbf{q}^{>}) \exp^{-H[\tilde{\vec{h}},\vec{\sigma}]} . \tag{2.53}$$

The top cutoff of the integration has been coarsened to $\frac{\Lambda}{b}$, thus the partition function with the modes $\tilde{\vec{h}}(\mathbf{q}^{<})$ is nearly identical to the original. In the rescaling phase, the cutoff is reset to its prior value following the transformation $\mathbf{x} = \frac{\mathbf{x}}{b}$ in real space, which is equivalent to $\mathbf{q} = b\mathbf{q}$ in momentum space. We should remember that when the integral is a d-dimensional integral, $d\mathbf{q}' = b^{d} d\mathbf{q}$ will hold. RG in real space concludes with field renormalization, $\vec{h}'(\mathbf{x}') = \frac{\tilde{\vec{h}}(\mathbf{x}')}{\zeta}$, and in momentum space using $\vec{h}'(\mathbf{q}') = \frac{\tilde{\vec{h}}(\mathbf{q}')}{z}$ [97, 125].

All of these RG processes lead to mathematical equations expressing RG flows in a parameter space. Scalability and universality are profoundly affected by the investigation of these flows and what they indicate about the underlying physical problem. In the context of equilibrium critical behavior, for instance, this generic aspect of RG is most evident in the method of real space renormalization as applied to lattice spin systems.

All the couplings in the reduced Hamiltonian form a set, $\{K\}$, of couplings. For instance, K_1 may have been the only coupling in the original model, with the others set to 0. However, applying the renormalization group can produce other couplings. The experimentalist will need to experiment with a wide range of tunable physical parameters such as temperature, pressure, and magnetic field to get a decent sense of the coupling constants. Consequently, one can consider the space of all potential couplings to be transformed by the RG transformation, R, as [126, 125]

$$\{K'\} = R\left(\{K\}\right) . \tag{2.54}$$

We suppose that the RG transformation has the form above, where R depends on the particular transformation chosen and the length rescaling parameter b. Then, there exists a fixed point, $K = K^{*}$, in the space of all possible couplings. As in the case of a single variable, we shall assume that R is differentiable at the fixed point; hence, the RG equations can be linearized about the fixed point as

$$K'_a - K^*_a \sim \sum_b T_{ab} \left(K_b - K^*_b\right), \tag{2.55}$$

where $T_{ab} = \frac{\partial K'_a}{\partial K_b}|_{K=K^*}$, and the indices a and b goes through all the couplings in set $\{K\}$. We denote the eigenvalues of matrix T as λ^i and its left eigenvectors as $\{\phi^i\}$. Hence, we have

$$\sum_b \phi^i_a T_{ab} = \lambda^i \phi^i_b. \tag{2.56}$$

The left eigenvectors of T are not necessarily the same as the right eigenvectors of T, as we have no reason to assume that T is symmetric. We cannot even assume that all eigenvalues are always real. Some eigenvalues, for instance, arise in complex conjugate pairs in some random systems [126]. This topic, however, goes beyond the scope of this thesis. We define scaling variables as linear combinations of the deviations from the fixed point as

$$u_i \equiv \sum_a \phi^i_a \left(K_a - K^*_a\right). \tag{2.57}$$

This can be simplified near the fixed point:

$$\begin{aligned} u'_i = \sum_a \phi^i_a \left(K'_a - K^*_a\right) &= \sum_{a,b} \phi^i_a T_{ab} \left(K_b - K^*_b\right) \\ &= \sum_b \lambda^i \phi^i_b \left(K_b - K^*_b\right) = \lambda^i u_i. \end{aligned} \tag{2.58}$$

The eigenvalues of the RG values, y_i, are defined as $\lambda^i = b^{y_i}$. They can be seen to be associated with the critical exponents [126]. We can distinguish three distinct cases:

- If $y_i > 0$, u_i is referred to as a relevant operator, as the RG transformation is repeated, the value moves away from the fixed-point.
- If $y_i < 0$, u_i is referred to as a irrelevant operator, and it converges to zero as the iteration

continues if we begin close enough to the fixed point.

- If $y_i = 0$, the value of u_i is referred to as a marginal operator. The linearized equations do not reveal whether u_i will move away from or toward the fixed point.

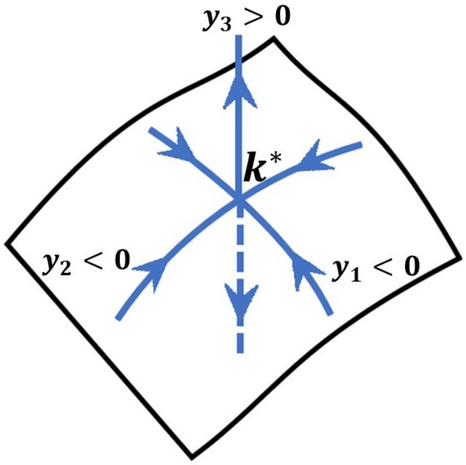

Figure 2.3: RG flow in a 3d space of coupling. The fixed point K^* has a basin of attraction with two irrelevant directions and one relevant direction.

We consider the case of a fixed point with n relevant eigenvalues. To make things easier to visualize, consider the space close to the fixed point to have m total dimensions. We consider the presence of $(m - n)$ irrelevant eigenvalues that attract into the fixed point. Hence, there will be a $(m - n)$-dimensional hypersurface. We assume that this hypersurface continues in a finite region surrounding the fixed point because of continuity, despite being the linear space spanned by irrelevant eigenvectors close to the fixed point. Because the fixed point governs the long-distance features of any system corresponding to a point on this surface, it is named the critical surface [126]. Figure 2.3 depicts the topology of a fixed point in three-dimensional space.

2.3.3 Kardar-Parisi-Zhang Equation

By applying RG to the KPZ equation, Eq. 2.5, we can determine the flow equations for the KPZ equation parameters. The flow equations for the parameters ν, D, and λ are [5, 6]

$$\frac{d\nu}{dl} = \nu\left[z - 2 + K_d g^2 \frac{2-d}{4d}\right] \tag{2.59}$$

$$\frac{d\mu}{dl} = D\left[z - 2 - 2\alpha + K_d \frac{g^2}{4}\right] \tag{2.60}$$

$$\frac{d\lambda}{dl} = \lambda\left[\alpha + z - 2\right], \tag{2.61}$$

where $K_d \equiv \frac{S_d}{(2\pi)^d}$ and S_d is the surface area of a d-dimensional unit sphere, and we define the coupling constant, g, as [6, 132]

$$g \equiv \frac{\lambda^2 D}{\nu^3}. \tag{2.62}$$

Before discussing the KPZ problem, we look at what the flow equations suggest for the EW equation, Eq. 2.2. In order to calculate the exponents, we should study all possible fixed points in the flow equations. If the nonlinear term in the KPZ equation is ignored, $\lambda = 0$, then the coupling constant, g, is zero, and $z - 2 = 0$ and $z - d - 2\alpha = 0$ are obtained. Therefore, $z = 2$ and $\alpha = (2 - d)/2$. We can also observe that the parameters of the EW equation can be rescaled independently of one another.

The exponents are then calculated for the KPZ problem, in which the parameters are not independent. The result of the third flow equation, $\frac{d\lambda}{dl} = 0$, is the scaling relationship $\alpha + z = 2$. Due to Galilean invariance, we expect that higher loop corrections will vanish, making this relationship precise for the KPZ systems. We may calculate the flow of the coupling constant, g, by utilizing the relationship for the coupling constant together with the three flow equations we know for ν, D, and λ,

$$\frac{dg}{dl} = \frac{2-d}{d} g + K_d \frac{2d-3}{4d} g^3. \tag{2.63}$$

We study the solution in a variety of cases, as the flow equation changes with the dimension of the space. Taking $\frac{dg}{dl} = 0$ yields the fixed point g^* of the equation. We begin with the case of $d = 1$, where there are only two fixed points [132],

$$g_1^* = 0 \quad \text{and} \quad g_2^* = \left(\frac{2}{K_d}\right)^{\frac{1}{2}}. \tag{2.64}$$

The g_1^* fixed point is repulsive, which means that if we start with g close to this fixed point, the system will flow away from it. In contrast, if the flow begins at a non-zero g near the fixed point g_2^*, it will continue to move towards this fixed point since g_2^* is an attractive fixed point, see Fig. 2.4. By entering the non-zero fixed point into the ν and D flow equations, we can derive the scaling exponents for $d = 1$ [6],

$$z = \frac{3}{2} \quad \text{and} \quad \alpha = \frac{1}{2}. \tag{2.65}$$

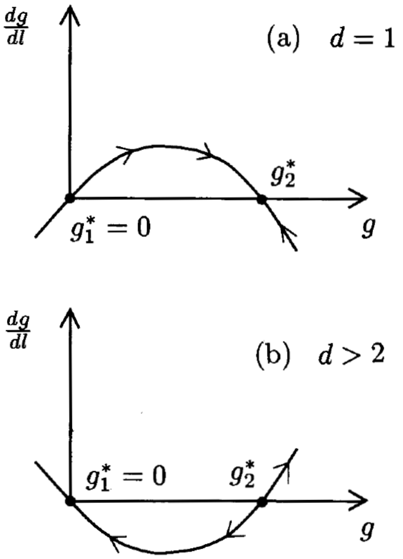

Figure 2.4: The flow for coupling constant g in (a) one dimension, where a non-zero fixed point is attractive and determines the scaling exponents, and (b) two dimensions, where a non-zero fixed point is repulsive, separates the linear regime, $\lambda = g = 0$ from the strong coupling regime for which in $\lambda \to \infty$ for one loop approximation. Adapted from Figure 7.4 in [6] with permission from Cambridge University Press.

In $d = 2$, according to the coupling constant flow equation, the coupling constant g is marginally relevant and grows with rescaling. There is no non-zero fixed point for the coupling constant g, and this fixed point is repulsive when $d > 2$. Here, there are two different phases. In the phase of weak coupling, where $g < g_2^*(d)$, the coupling constant starts to disappear, and growth is described by the EW equation. In the region of strong coupling, if $g > g_2^*(d)$, the coupling constant flows to infinity, indicating the existence of new scaling behavior whose exponents can be determined using numerical simulations, see Fig. 2.4.

2.3.4 Molecular Beam Epitaxy Equation

Changing to the co-moving reference frame, $h \longrightarrow h - vt$, eliminates the constant flux term, which has no impact on the scaling exponents. The physically unmotivated term, $\nabla \cdot (\nabla h(\mathbf{x}, t))^3$, is neglected as well. Therefore, we have a growth equation, which is the lowest-order non-linear equation with conserved dynamics and non-conserved noise [111, 112]:

$$\partial_t h(\mathbf{x}, t) = -K\nabla^4 h(\mathbf{x}, t) + \lambda_1 \nabla^2 (\nabla h(\mathbf{x}, t))^2 + \xi(\mathbf{x}, t). \tag{2.66}$$

We use the dynamic RG to find the scaling exponents. The equations describing the flow equation of the non-linear MBE equation, Eq. 2.19, as [6, 133]

$$\frac{dK}{dl} = K\left[z - 4 + K_d \frac{\lambda_1^2 D}{K^3} \frac{6-d}{4d}\right], \quad \text{and} \tag{2.67}$$

$$\frac{dD}{dl} = [z - 2\alpha - d], \tag{2.68}$$

$$\frac{d\lambda_1}{dl} = \lambda_1 [z + \alpha - 4], \tag{2.69}$$

where $K_d \equiv \frac{S_d}{(2\pi)^d}$ and S_d is the surface area of d-dimensional unit sphere, and the coupling constant, g, is

$$g^2 \equiv \frac{\lambda_1^2 D}{K^3}. \tag{2.70}$$

We determine the flow of the coupling constant, g, by combining the coupling constant relationship with the three flow equations for K, D, and λ_1 as

$$\frac{dg}{dl} = \frac{4-d}{d} g + K_d \frac{3(d-3)}{8d} g^3. \tag{2.71}$$

We can exactly determine the exponents due to the availability of the two scaling relations. The first is the result of setting the flow equation for D to zero, $\frac{dD}{dl} = 0$:

$$z - 2\alpha - d = 0. \tag{2.72}$$

By setting the equation of the non-linear coefficient, λ_1, equal to zero, $\frac{d\lambda_1}{dl} = 0$, we obtain the second scaling relation:

$$z + \alpha - 4 = 0. \tag{2.73}$$

These two scaling relations are exact, and we can use them to obtain the scaling exponents for the MBE growth process [6]

$$z = \frac{8+d}{3}, \qquad \alpha = \frac{4-d}{3} \quad \text{and} \quad \beta = \frac{4-d}{8+d}. \tag{2.74}$$

We can compare the exponents for the KPZ and MBE equation in one dimension, $d = 1$. For the MBE equation in one dimension, we have the following scaling exponents which are greater than the KPZ scaling exponents

$$z = 3 \quad \text{and} \quad \alpha = 1. \tag{2.75}$$

The linear theory predicts different values for these quantities. The larger roughness exponent was induced by the absence of non-linear term. These scaling exponents of the non-linear MBE equation correctly represents the scaling behavior of a variety of discrete models developed to characterize the MBE growth process [6].

2.4 Discrete Growth Models

The morphologies and scaling behavior observed in surface growth studies can perhaps be better understood by analyzing basic discrete models. The gap between experimental results and continuous theories may be bridged by discrete models. These models can also be used to analyze the effects of certain mechanisms, such as surface diffusion and desorption.

Scaling exponents for systems with $d > 1$ are frequently computed numerically due to mathematical complexities, and we need the exponents to determine the scaling universality class. For example, we cannot compute the KPZ exponents analytically for $d > 1$ [134, 135]. However, we can obtain reasonable approximations for the exponents by employing discrete models. In this section, we present a few models that have considerably contributed to our understanding of specific aspects of surface roughening.

Generally, non-equilibrium growth processes involve models with random deposition, local relaxation, and sticking principles. Typically, when atoms or cells are deposited or produced, they migrate over the surface for a short distance before becoming firmly attached. Due to the simplicity of their relaxation criteria, these models are the most numerically efficient since they can perform large-scale simulations for extended periods of time, which increases the possibility of obtaining asymptotic scaling behavior.

The majority of growth models, including the Eden model [136] and the ballistic deposition (BD) [7] model, are founded on attempts to resolve real physical or biological challenges. In particular, vapor deposition can be modeled using the BD model, while biological growth can be modeled using the Eden model. There are issues with these models, such as the imprecision of their scaling exponents. Studying the collective behavior of atoms during growth is another scenario that could benefit from numerical simulations of discrete models. Paradigmatic cases are the Wolf-Villain [113], and Das Sarma and Tamborenea [114] model.

Numerous numerical investigations have also been driven by the need to deduce how quenched disorder affects the morphology of surfaces. Overhangs on the surface are disregarded by a group of models [137, 138, 9], whereas overhangs are allowed by another group of models [139, 140, 141]. There is a mapping between surface growth in the presence of quenched disorder and the two types of well known problems: the directed percolation problem and the site percolation problem, respectively. This section also includes a discussion of the directed percolation depinning (DPD) model [9, 6].

2.4.1 Ballistic Deposition

The Ballistic Deposition (BD) model was first proposed as a simplified sedimentation model [7]. Since falling particles adhere to their first nearest neighbor on the aggregate, the BD model is one of the simplest nearest-neighbor models. To establish the next-nearest neighbor model, we just need to permit particles to also attach to a neighbor on the diagonal.

The model's non-linear term, which is the result of the lateral sticking rule, is responsible for the existence of voids. Vacancies accelerate the surface's expansion because the mean height grows at a faster rate for the same number of deposited particles. The non-linear factor is included in both the nearest neighbor and the next-nearest neighbor models, therefore non-linear theory may describe the scaling characteristics of both. These two models belong to the same universality class [6].

To illustrate the model's functionality, let's imagine a substrate of length L, sectioned into L equal columns. Each of the particles is a tiny square that is dropped vertically onto the flat, one-dimensional substrate. Particles are released one by one and accumulate in random columns above the substrate. By adhering on top of or to the side of their nearest neighbors, particles take into account both the nearest neighbor and next-nearest neighbor models, see Fig. 2.5.

The height profile $h(x, t)$, also known as the surface, completely determines the dynamics of this expanding process. The height, h, in a certain column, x, at a particular time, t, can be expressed as a discrete integer value by the following function:

$$h(x', t+1) = max[h(x'-1, t)\, ,\ h(x', t)\, ,\ h(x'+1, t)], \tag{2.76}$$

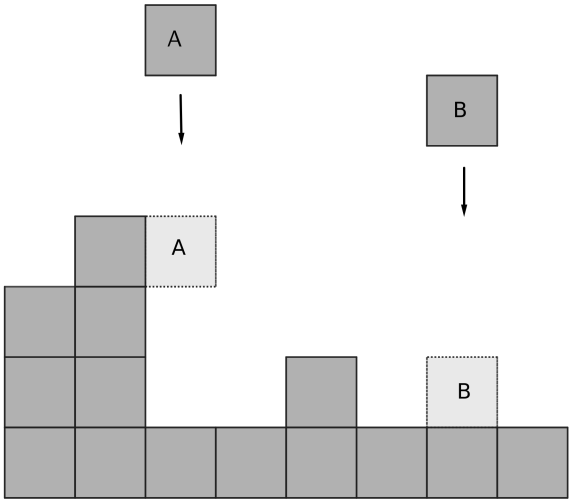

Figure 2.5: By use of ballistic deposition (BD) [7], square particles are deposited one at a time from random heights above a flat substrate; these particles adhere to the substrate upon initial contact. The attachment points of squares A and B to their respective surfaces are shown by the dashed lines squares A and B.

where $h(x,t)$ is the height-profile and x' is a column number between 1 and L selected randomly at time t. Each "drop" of particles in this terminology represents one unit of time. It is more practical to measure time in terms of deposited layers. Therefore, $t = N/L$ where N is the total number of particles deposited and L is the length of the substrate. Boundary effects can be mitigated and scaling behavior enhanced by employing periodic boundary conditions.

2.4.2 Eden Model

Colonies of organisms, whether they are bacteria or cells in tissue culture, can be understood from the perspective of a conventional growth model first given by M. Eden in 1961 [136]. Currently, it is believed that the scaling properties are defined by the KPZ equation. In accordance with KPZ predictions, early simulations established $\alpha = 0.5$ for $d = 1$ [142, 143]. The model is defined as follows: Consider a lattice in which a seed particle is initially situated at the origin. Each newly formed particle randomly joins an already existing particle anywhere along the seed's perimeter, Fig. 2.6. Iterated Eden models produce a cluster with a somewhat circular core and a rough surface [144, 145, 146].

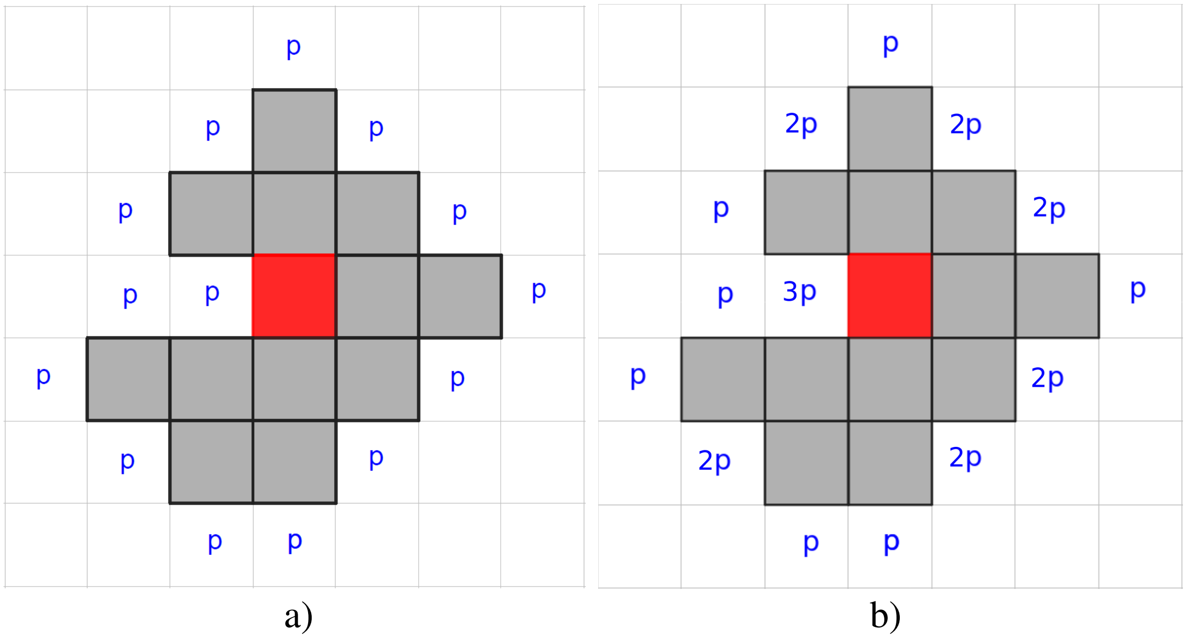

a) b)

Figure 2.6: Figure illustrates two distinct Eden models. In both models, the growth started from the red square. In the subsequent stage, one of the neighboring sites to the surface will be chosen, where in the (a) all unoccupied sites have the same probability p, however in the (b) the probability is dependent on the number of bonds each unoccupied site has with the surface.

In addition, the geometry of growth from a horizontal substrate of length L and periodic boundary condition is investigated. Growing from a line of seeds rather than a single seed makes it easier to examine its surface features. There are three distinct Eden models, each with its own microscopic rules for selecting a suitable growing location [147]. Finally, off-lattice variations of the Eden model have occasionally been discussed in the literature [148, 149, 150].

Methods for reducing noise allow for more precise estimates of the exponents and validation of the validity of the scaling relation [151]. These methods [152, 153, 154, 155] permit the intrinsic width to be reduced by keeping track of the number of times a certain growth site is chosen at random. The site becomes occupied only when the counter reaches a specified threshold value s, known as the noise reduction parameter.

2.4.3 Irreversible Molecular Beam Epitaxy Growth Models

Wolf and Villain [113], and Das Sarma and Tamborenea [114] independently proposed models of non-equilibrium growth that incorporated deposition and surface diffusion. The functionality of the model is defined as follows: a particle is defined to be placed at a random site at each time step, after which the particle can migrate to the left or right by one site, or remain stationary. The Wolf-Villain (WV) model implies that the particle will go to the site with the strongest binding to the surface [113], whereas the Das Sarma-Tamborenea (DT) model says that the particle will migrate to the closest kink site to increase the number of neighbors [114], see Fig. 2.7.

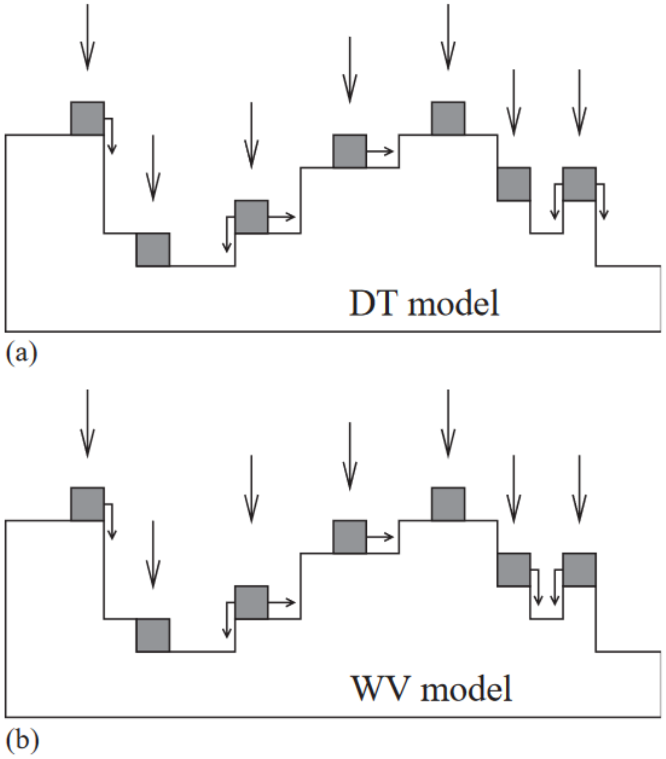

Figure 2.7: (a) the DT model and (b) the WV model. The columns of incidence of the particles are shown by large vertical arrows. Small arrows indicate the path of a particle after it collides with the surface, and when there are two possible courses of action, one is chosen at random. Image taken from Ref. [8] with permission from Elsevier Press.

When comparing the relaxation processes of the two models, there are only minor differences. The key feature of surface relaxation in both models is that atoms diffuse to maximize their number of neighbors. The irreversible sticking after relaxing is similar to how, at low temperatures, atoms attached to the edge of an island form strong connections with neighboring atoms. There are alternative methods that are more in line with the actual surface relaxation process occurs during the MBE growth phenomena. For instance, there are models in which all surface atoms hop around with a probability determined by the Arrhenius law [156, 157, 158, 159, 160]. Due to the lengthy activation procedure, these models can only manage short simulation times and small system sizes.

Calculating the scaling exponents determines whether these models obey the linear or non-linear MBE growth equations. It has been suggested that the Wolf-Villain and related models do not follow the Family-Viscek scaling relation [161, 86, 162]. Kotrla *et al.* [163, 164] and Das Sanna and Ghaisas [165] explored the generalization of the WV model to two dimensions with local surface diffusion. They found exponents that closely matched those expected by the non-linear equation.

2.4.4 Directed Percolation Depinning

Using the directed percolation depinning (DPD) model, the depinning problem can be mapped onto the percolation framework. In the presence of quenched disorder, the link between directed percolation and surface expansion was separately established by two separate studies [166, 9].

We start with an L-sided square lattice with periodic boundary conditions (PBCs). Initially, the surface consists of a horizontal line, which is the first row of the lattice. To include the quenched disorder in the lattice, we block a portion of the cells on the lattice. The surface will be halted by the blocked cells, but development can proceed uninterrupted in unblocked cells. As the first step, we select a cell at random from the surface's closest neighbors that are not blocked. The selected cell and its column neighbors then be added to the surface. Next, a second unblocked cell is selected for addition to the surface, and the previous processes are

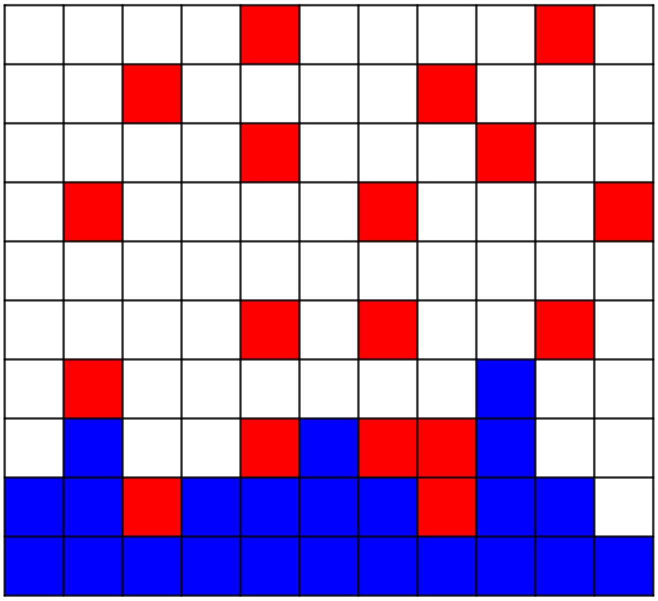

Figure 2.8: The DPD model [9] for surface growth without overhangs. The blue sites represent a system that expands in a lattice with quenched disorder (red sites).

repeated [6], see Fig. 2.8.

The model's design forbids overhangs. If the fraction of blocked cells is less than a critical threshold, P_c, then the surface continues to spread unobstructed; if it is greater than P_c, then the surface is pinned by the blocked cells. The roughness exponent, α, for this model is reported to be $\alpha = 0.63$, which is the same as the roughness exponent of dipping a paper in suspensions of ink or coffee [9].

Chapter 3

Numerical Methods

In this chapter, we will explore *CellSim3D*, an off-lattice growth model and open source package designed to model massive systems on a single [10] and multiple Graphics Processing Units (GPUs). The *CellSim3D* is a coarse-grained molecular dynamics model of celluar dynamics. Molecular dynamics (MD) algorithm is applicable to the study of everything from atoms to colloid particles that interact with one another via a potential [167, 168, 169, 170, 171, 172, 173]. A force field is a functional form and set of parameters used to express the potential energy of a system of particles. There are various types of force fields, including all-atom and coarse-grained [174, 175]. All-atom force fields contain parameters and interactions at the atomic level, whereas coarse-grained force fields are derived by integrating out the interactions at shorter time scales and smaller length scales, and replacing them with a coarse grained description of the system [176, 177, 178]. For instance, viscoelasticity of the cell membrane on a small length scale can be attributed to the biochemical interactions between the phospholipids that make up the cell membrane and the biochemical interactions between the actin filaments and myosin motors in the actomyosin cortex. At the scale of cell size, a coarse-grained force field integrates out those biochemical interactions and describes the membrane as a viscoelastic object.

3.1 CellSim3D Assumptions

We are interested in studying mechanical behavior and dynamics of cell tissues that are affected by the mechanical properties of their constituent cells, such as how cells grow and interact with their environment [18, 179, 180]. This implies that the model should include an approximation of parameters such as the mechanical properties of cells and substrates [181, 182]. To be accurate, the model must have variables that indicate the degree of interactions between cells and their environments, such as neighboring cells, the extracellular matrix (ECM), and the liquid medium. It is also necessary to consider cell development and division as well as their effects on the cell's environment [179]. Even if the stimulus is not mechanical, an approximation of the cell's mechanical responses must be made. When simulating the mechanical cell, one must take into account a variety of complicated interactions.

We assume that each cell type has a unique set of parameters that characterize it. Cell's mechanical properties are not always the same in every direction. There is a wide range in the density of cell adhesion molecules (CAMs) within a cell membrane [183]. For our model, we suppose that they are isotropic. In actual cells, mechanical parameters such as stiffness [184] and adhesion strength [185] can vary. However, here, we assume that they are uniform.

Cells can communicate over long and short distances. Hormones and synapses are two forms of long-distance communication. They are not included in the interaction forces in *CellSim3D*. In our models, intercellular communication is limited to short-range communication via mechanical contact. Cells also interact with the ECM [186, 187, 188]. Many different types of proteins form the ECM, which has a significant impact on cell behavior [2]. We do not model the ECM explicitly; instead, we approximate it as a fluid.

Cell surfaces can first be viewed as elastic substances. The actomyosin cortex and the lipid bilayer are the two major components. Since the acin filaments can flow past each other, the membrane can be considered a viscous material [189]. We consider the membrane as viscoelastic so that it can mimic the membrane's ability to be both stiff and flexible.

Cell division may not be possible without strong sphericity in the parent cells [190, 191, 192]. The balance of forces between the cell membrane's contractility, and the incompressiblity of the cell's contents causes a cell to be roughly spherical when submerged in liquid [32, 193]. We assume that cells divide symmetrically through their centers of mass and asymmetrically by placing the division plane off-center.

Finally, undesirable environmental conditions, lack of nutrients, or a signal from the organism in which they live can all cause cells to die [62, 194, 195]. In the apoptosis process, the cell loses its internal pressure and shrinks, the cytoplasm becomes denser, and the organelles become more densely packed [196]. Apoptosis of cells is modelled as a Poisson process. During apoptosis, the growth rate changes from positive to negative, and cells begin to shrink before being removed when their volume falls below a predetermined threshold.

3.2 Force Field And Cell Structure

The force field is an approximation of the physical interactions that occur between the particles on the time and length scales of the system. The evolution and dynamics of cell tissue are approximated by the classical mechanics framework of mechanical forces, with respect to time and length scales determined by the average cell size and division cycle times.

In the *CellSim3D* model, we concentrate on the cellular components responsible for the cells' mechanical properties to construct a force field. These characteristics include rigidity, pressure, cell adhesion, and interaction with its environment. Exterior, interior, and environment form the bulk of a cell. A cell's internal structure consists of organelles and cytoplasm. The cell boundary is roughly defined by the actomyosin cortex, the cell membrane, and the cell wall. The ECM is a wide range of three-dimensional scaffolding on which cells can be located. In this section, we will discuss the *CellSim3D* force field.

3.2.1 Cell Shape And Boundary

In the *CellSim3D* model, the cell boundary is considered a single object with underlying mechanical properties such as stiffness and viscosity. The integrated structure of the cellular boundary will hereafter be referred to as the cell membrane.

Due to the diverse sizes and shapes of cells, we approximate their structure by using the cell's shape as input. To keep things simple, we utilize a well-known geometry that is simple to implement into the program. To begin, we suppose that the cells' surfaces are spherical while they are in mechanical equilibrium. Cell surface nodes are shown in Fig. 3.1, along with their connections. To simulate cells with a relatively homogeneous actomyosin cortex, the distance between the nearest neighbor nodes should be nearly equal. A large number of nodes is necessary to adequately resolve the spherical shape of the cell, despite the fact that a small number of nodes is advantageous for accelerating simulation time.

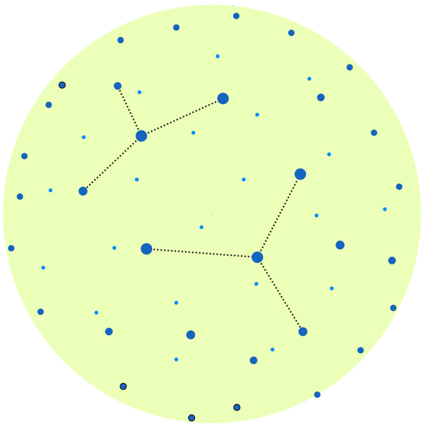

Figure 3.1: In our model, we suppose that the cell is a sphere and that its mechanical properties are comparable to those of a viscoelastic sheet represented by a network of connected balls. Models are constructed using the C180 molecule's shape and topology, as well as the positions of its carbon atoms at equilibrium. The nodes that are closer to the viewer are shown in a larger size than those that are farther away.

The fullerene C180 geometry satisfies the above requirements. It has three times as many carbon atoms as its more well-known sibling, the C60 fullerene. Its geometry can be found in various sources [197, 198]. Carbon atoms are the nodes in our cells, and the force field models the interactions between these nodes. There are 180 nodes in the mesh on the surface of the cell, which gives sufficient resolution while maintaining reasonable performance. The surface of the fullerene is uniformly covered by these nodes organized in hexagons and pentagons by the Euler rule, and all of the bonded nodes have almost the same equilibrium bond length. At mechanical equilibrium, the fullerene is around 95 percent spherical. To determine how similar an object's form is to that of a sphere, the sphericity, ψ, is defined as a function of volume V and surface area A [199]

$$\psi = \frac{\pi^{\frac{1}{3}}(6\mathrm{V})^{\frac{2}{3}}}{\mathrm{A}}. \tag{3.1}$$

3.2.2 Force Field

Each node on the cell is subjected to forces generated by both intercellular and intracellular interactions. Intracellular forces are represented by simple, damped Hookean springs that stand in for the cell membrane and an internal pressure that drives the cell growth process. We begin by giving a description of intracellular forces.

The damped harmonic oscillator force, $\mathbf{F}^{\mathrm{B}}$, between a node i and its bonded neighbors j on a cell's membrane is given as

$$\mathbf{F}_i^{\mathrm{B}} = \sum_{j=1}^{3}[k_{ij}^{\mathrm{B}}\,\hat{\mathbf{b}}_{ij}\,(R_{ij} - R_{ij}^0) - \gamma_{\mathrm{int}}\mathbf{v}_{ij}], \tag{3.2}$$

where R_{ij}^0 is the equilibrium bond length between nodes i and j, $\mathbf{v}_{ij}$ is the relative velocity between nodes i and j, and $\hat{\mathbf{b}}_{ij}$ is a vector from node i to j. The parameter γ_{int} is the coefficient of friction that dampens the oscillations of the bonds, and the bonding spring constant, k_{ij}^{B}, is constant throughout all bonds. The angle force, $\mathbf{F}^{\theta}$, is a harmonic force exerted on three nodes, i, j, and k which oppose the deformation of the angle between these three nodes and maintains cell curvature. It is defined as

$$\mathbf{F}_i^{\theta} = \frac{1}{2} \sum_j \sum_{k \neq i} - k_{ijk}^{\theta} \, \nabla_{\mathbf{x}i} \, (\theta_{ijk} - \theta_{ijk}^0)^2, \tag{3.3}$$

where θ_{ijk}^0 is the equilibrium angle between three nodes i, j, and k, and the angle spring constant, k_{ijk}^{θ}, considered to be constant over the cell's surface in our model. The gradient, $\nabla_{\mathbf{x}i}$, is taken with respect to the position of the node i. We consider it constant throughout all bonds. Figure 3.2 shows the first neighbors j (three) and second neighbors k (six) for node i on the surface of a cell.

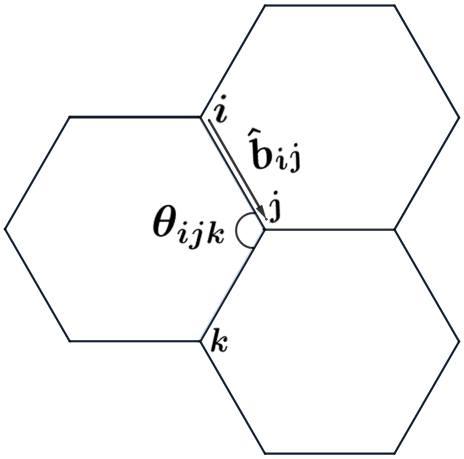

Figure 3.2: The intracellular forces acting on node i are dependent on the node's first and second neighbors. This node's three initial neighbors, j, will give the bond forces, while each initial neighbor's two additional neighbors, k, will offer the angle forces. For convenience, only one of the first and second neighbors is labeled.

To simulate cell development and division, we must include a growth force in the force field. This is done via a pressure force. This pressure results from the incompressibility and tonicity of the cytoplasm's physical and chemical properties. This hydrostatic pressure caused by differences in osmolyte concentrations between a cell's cytoplasm and its outside affects the shape and form of the cell [193, 200, 201, 202, 190]. $\mathbf{F}^{\mathrm{P}}$ is the growth force resulting from intracellular osmotic pressure. It is defined as

$$\mathbf{F}_i^{\mathrm{P}} = (PS)\,\hat{\mathbf{n}}_i, \tag{3.4}$$

where P is the force due to pressure and S is the unit area element on the surface. The normalized vector, $\hat{\mathbf{n}}$, defines a family of planes parallel to the surface tangent of the sphere at the location of i, and it defines the direction of the pressure force. Since cells are approximately spherical, we define the normalized vector, $\hat{\mathbf{n}}$, as the vector pointing from the cell's center of mass to the node on the cell surface, $\hat{\mathbf{r}}_{\mathrm{CoM}}$. This assumption regarding the direction of the normalized vector will be beneficial when cells deform into irregular shapes and the growth force can makes their shapes even more irregular.

The initial cell pressure is set at $(PS)_0$ and it increases by the growth rate, $\varDelta(PS)$, to the maximum value of $(PS)_\infty$. The increase in pressure results in an increase in the cell volume up to the threshold volume V_{div} at which cells divide.

Intercellular interactions include adhesion, repulsion, friction between cells, and friction between cells and the extracellular environment. Due to the variety of CAMs, accurate cell-cell contact is difficult to recreate. We assume, based on this mechanical cell approximation, that the individual contacts of multiple CAMs may be averaged to provide a uniform interaction on the cell surface. These mechanical communications between cells are short-ranged. When two cell membranes come into contact, the adhesive component holds them together, while the repulsive part keeps them apart by repelling them. We consider $\mathbf{F}^{\mathrm{R}}$ and $\mathbf{F}^{\mathrm{A}}$ as the repulsive and attractive forces between nodes in different cells, respectively. Figure 3.3 shows two nodes i and j on the surface of the cells m and n in the range of the attraction and repulsion interaction. Harmonic potentials with variable spring constants and cutoffs are used to approximate these

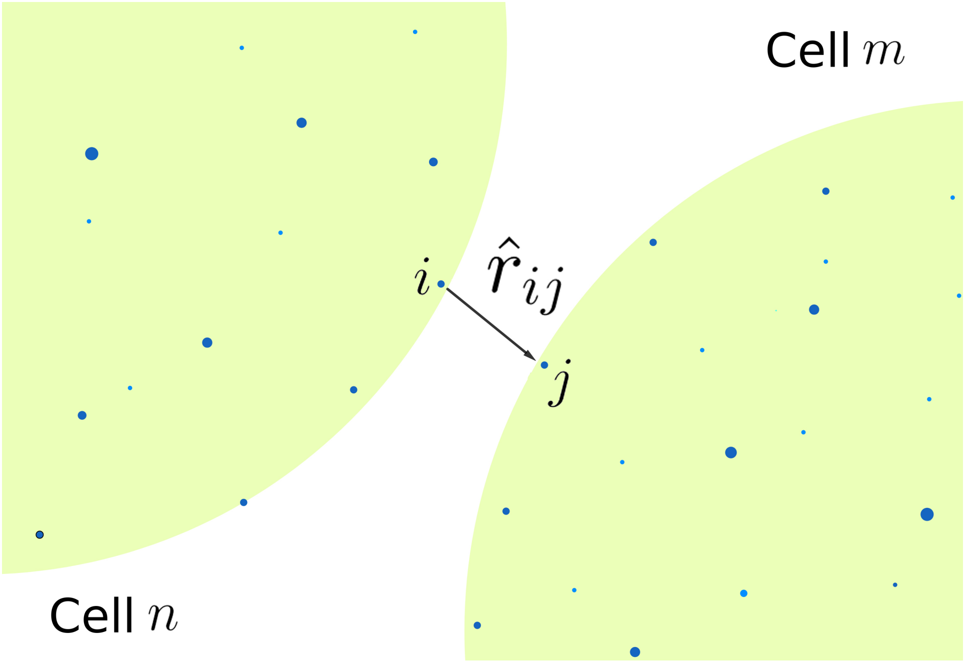

Figure 3.3: The position of two cells (m and n) that are close enough to activate intercellular forces. The attracting and repulsive forces will be parallel to $\hat{r}_{ij}$ and between the two nodes i and j. In addition, they will suffer a frictional force tangent to the relative velocity $\mathbf{v}_{ij} = \mathbf{v}_i - \mathbf{v}_j$.

terms as follows:

$$\mathbf{F}^{\mathrm{A}}_{i,m} = \sum_n \sum_j \begin{cases} \mathrm{k}^{\mathrm{A}} \, (\mathrm{r}_{ij,n} - R^{\mathrm{A}}_0)\hat{\mathbf{r}}_{ij,n} & \text{if } r_{ij,n} < R^{\mathrm{A}}_0 \; ; \\ 0 & \text{if } r_{ij,n} \geq R^{\mathrm{A}}_0 \; , \end{cases} \tag{3.5}$$

and

$$\mathbf{F}^{\mathrm{R}}_{i,m} = \sum_n \sum_j \begin{cases} -\mathrm{k}^{\mathrm{R}} \, (r_{ij,n} - R^{\mathrm{R}}_0)\hat{\mathbf{r}}_{ij,n} & \text{if } r_{ij,n} < R^{\mathrm{R}}_0 \; ; \\ 0 & \text{if } r_{ij,n} \geq R^{\mathrm{R}}_0 \; , \end{cases} \tag{3.6}$$

where $\mathbf{k}^{\mathrm{A}}$ and $\mathbf{k}^{\mathrm{R}}$ are the attraction and repulsion spring constants, and R^{A}_0 and R^{R}_0 are the attraction and repulsion equilibrium bond lengths and cutoffs, respectively.

The mechanical characteristics of organs are determined by the combined mechanical properties of their environment and cells. The ECM is composed of several protein-based molecules, such as collagen, elastin, fibronectin, and laminins [203], which form a three-dimensional scaffolding into which cells can adhere.

Biochemical and biomechanical properties of the ECM play crucial roles in cell migration.

The ECM surrounding the cells has a dynamic structure and can be altered by cells stimulus to better suit their needs [204, 205, 206]. There is evidence that cells prefer some types of ECM over others and will migrate to those regions where the ECM is more readily available [203]. Instead of directly modeling the ECM, we approximate it as a fluid.

$\mathbf{F}^{\mathrm{F}}$ is the friction term separated into viscous drag due to cell-extracellular matrix interactions and intermembrane friction, which is proportional to the relative velocity tangential to the cell surface. Intermembrane friction force is defined as:

$$\mathbf{F}^{\mathrm{F,e}}_{i,m} = \sum_n \sum_j \begin{cases} -\gamma_{\mathrm{ext}}\, \mathbf{v}^{\tau_m}_{ij} & \text{if } r_{ij,n} < R^{\mathrm{A}}_0 \; ; \\ 0 & \text{if } r_{ij,n} \geq R^{\mathrm{A}}_0 \; , \end{cases} \tag{3.7}$$

where γ_{ext} is the intermembrane friction coefficient, and $\mathbf{v}^{\tau_m}_{ij}$ is the relative velocity tangential component to the surface, see Fig. 3.3. The second friction force term is the viscous drag due to medium. It is defined as

$$\mathbf{F}^{\mathrm{F,m}}_{\mathrm{i}} = -\gamma_{\mathrm{m}}\, \mathbf{v}_{\mathrm{i}}, \tag{3.8}$$

where γ_{m} is the drag coefficient, and $\mathbf{v}_i$ is the velocity of the node i. Finally, η is a Gaussian white noise given by $\langle \eta(x,t) \rangle = 0$ and $\langle \eta(s,x)\eta(t,y) \rangle = 2D\delta(s-t)\delta(x-y)$. Taking into account all the forces given above, we describe the force field operating on node i as

$$\mathbf{F} = m\mathbf{r} = \mathbf{F}^{\mathrm{B}} + \mathbf{F}^{\theta} + \mathbf{F}^{\mathrm{P}} + \mathbf{F}^{\mathrm{R}} + \mathbf{F}^{\mathrm{A}} + \mathbf{F}^{\mathrm{F}} + \eta. \tag{3.9}$$

3.3 Cell Division

We need to simplify the cell division process since the real process of cell division, cytokinesis [207, 208], cannot be approximated accurately and involves processes occurring at all scales, from the atomic to the cellular size. We consider the cell cycle loop in its simplest form. During the first phase of the cell cycle, the growth force causes the cell to expand until it is ready to divide.

The cell is prepared for division after it has reached a large enough size, which is usually defined as having doubled in volume. The parent cell must also be sufficiently spherical to allow for division. Measurements of the morphologies of animal cells right before dividing have shown this [190, 191, 192, 207].

The cell division plane's orientation and position are significant geometric properties [209, 210, 211]. The direction and position of the division plane and the manner in which it is chosen are the distinguishing characteristics of cells that differentiate into distinct cell types [212, 213, 208]. In symmetric division, the plane of cell division passes through the cell's center of mass, resulting in the formation of two identical daughter cells. By placing the division plane off-center, cells may divide into two distinct types, resulting in asymmetric division. For instance, a stem cell can divide into another cell, such as a heart cell, and then the heart cell can continue to produce further heart cells.

There are a variety of alternative rules that may be used to identify the direction of the division plane. For example, Hertwig's rule states that the division plane of an ellipsoidal cell is perpendicular to its longest axis and passes through its center of mass [214], whereas according to Errera's rule, the division plane must contain the shortest path through the cell's center of mass [215]. Additionally, the division plane can be randomly oriented to develop spherical tissue.

In *CellSim3D*, we choose a random orientation for the division plane by randomly selecting a unit vector to define the normal vector to the division plane, and then divide the cell into two equal halves [10, 216]. The position of the cell division plane can either pass through the cell's center of mass or another randomly chosen point within the cell, which will cause asymmetric cell division.

For the cell division, we first copy the nodes of the parent cell in the same location to have two sets of 180 nodes for each daughter cell, and then transfer the nodes of one daughter cell, half the repulsion range, $0.5R_0$, to the right of the division plane and the nodes of the other daughter cell, half the repulsion range, $0.5R_0$, to the left of the division plane. In addition, we define two new planes, P_R and P_L, which are parallel to the division plane and half the repulsion range to the right and left of the division plane, respectively. Finally, for the daughter cell moved to the right of the division plane, we project the nodes on the left of the P_R on the P_R, and for the daughter cell moved to the left of the division plane, we project the nodes on the right of the P_L on the P_L. The process is shown in in Fig. 3.4.

CellSim3D can simulate two dimensional tissues as well. In an epithelium, a quasi two-dimensional sheet of cellular tissue, cells are coordinated in a two dimensional plane. These tissues are essential for the proper functioning of several organs, including the retina, epidermis, and endothelia. We confine the systems between two plates, where the bottom plate mimics the base of the tissue, and the top plate serves as a barrier to prevent excessive buckling of epithelial cells. In order to generate epithelium, the normal vector to the division plane, **s**, is a random unit vector in the plane specified by the the normal vector to the epithelial plane in space[10, 216].

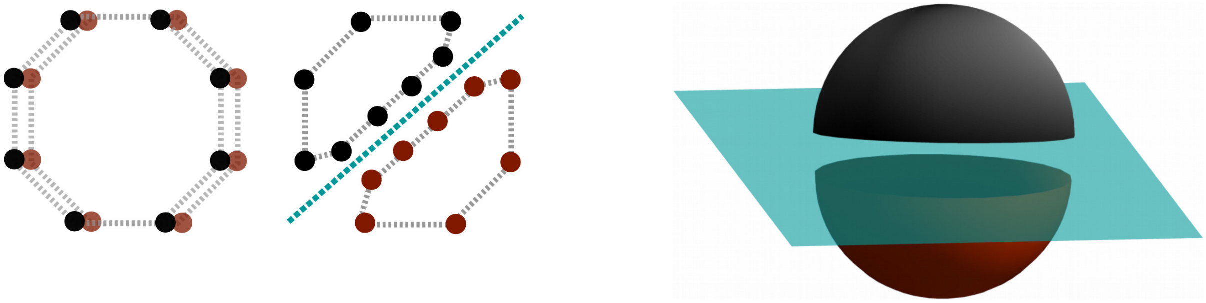

Figure 3.4: The nodes of a cell larger than the threshold division volume are copied (black and red). The cell is divided in half by a randomly oriented division line (green). The nodes of the two new cells are projected so that the nodes in contact are placed along the division plane. Image taken from Ref. [10] with permission from Elsevier Press.

3.4 Cell Apoptosis

In *CellSim3D*, we attempt to represent cell apoptosis, which involves cell shrinkage and phagocytosis of apoptotic material. The breakdown of a dying cell into smaller pieces is a crucial biological process during apoptosis. Three known stages of apoptotic cell disintegration are membrane blebbing, formation of membrane protrusions, and cell fragmentation. In membrane blebbing, small amounts of blebs occur on the cell surface; as the apoptosis process progresses, the blebs get bigger and help break organelles like the nucleus [217, 218, 219]. Following apoptotic membrane blebbing, cells experience additional morphological alterations. Microtubule spikes, apoptopodia, and beaded apoptopodia are among the thin apoptotic membrane protrusions produced by cells during membrane protrusion development [35]. For example, it has been postulated that the development of microtubule spikes facilitates the separation of membrane blebs and the distribution of nuclear contents into membrane blebs [35]. Finally, cells split into many vesicles known as apoptotic bodies, which undergo phagocytosis, as the last step in the process of apoptotic cell disintegration. Figure 3.5 depicts each of these processes.

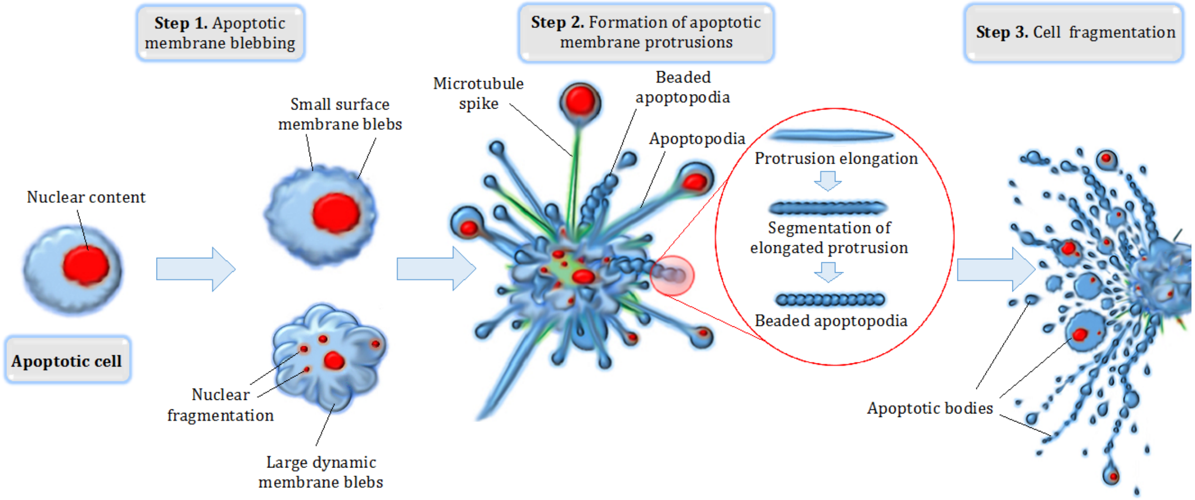
Step 1. Apoptotic membrane blebbing
Step 2. Formation of apoptotic membrane protrusions
Step 3. Cell fragmentation
Nuclear content
Apoptotic cell
Small surface membrane blebs
Nuclear fragmentation
Large dynamic membrane blebs
Microtubule spike
Beaded apoptopodia
Apoptopodia
Protrusion elongation
Segmentation of elongated protrusion
Beaded apoptopodia
Apoptotic bodies

Figure 3.5: Before the apoptotic cell is removed, it undergoes disassembly process, which includes membrane blebbing, membrane protrusion formation, and cell fragmentation. Image taken from Ref. [11], CC license.

In *CellSim3D*, the cells' apoptosis process is modeled as Poisson process, where the average interval between the events is constant, but each event occurs at a random time, regardless of what occurred previously. After a cell is selected to undergo apoptosis, its growth rate changes from positive to negative. Consequently, cells lose internal pressure and begin to shrink. Finally, the cell is removed when its volume falls below a predetermined volume threshold. User-defined parameters include the Poisson rate parameter, λ, the negative growth rate, and the volume threshold.

3.5 The CellSim3D Implementation

The source code for *CellSim3D* is written in standard C/C++ and available at `https://github.com/SoftSimu/CellSim3D` under the GPLv2 [220]. It is accelerated with CUDA [221] and parallelized with the Message Passing Interface (MPI) to run on multiple NVIDIA GPUs. The majority of computations are performed using only CUDA, with only a small amount of C/C++ host code controlling the execution and handling data input and output. The present multi-GPUs version allows users to simulate millions of cells with high efficiency. *CellSim3D* simulator was tested on a single GPU, including the GTX 760, GTX 780, GTX 980, GTX 1080Ti, GTX Titan Xp, and GTX 960M [10, 216], and also on multi-GPUs on super computing clusters such as ComputeCanada, Canada's national high-performance compute (HPC) system, and the Finnish Grid and Cloud Infrastructure (FGCI). In order to minimize the latency of communication between the host RAM (Random Access Memory) and GPU RAM, we performed computations on the GPU as much as possible.

In this section, we describe the implementation of the algorithms, such as the integrator, boundary conditions, multi-GPUs algorithm, and neighbor list algorithm. Finally, the *CellSim3D* simulation units are discussed.

3.5.1 The Integrator

To update the positions and the velocities of the systems over time, the velocity-Verlet integrator [222] is commonly employed. This does not work in *CellSim3D*. The friction force depends on the relative velocities between the cells and the cells velocity in the medium. We use the Dissipative Particle Dynamics approach [223, 224].

Since this process is computationally expensive, methods that approximate the velocity

Table 3.1: This table represents the DPD-VV integration algorithm implemented in *CellSim3D* [10, 14], where $\mathbf{F}^{\mathrm{C}}$ represents the conservative forces, $\mathbf{F}^{\mathrm{D}}$ represents the dissipative forces, and $\mathbf{F}^{\mathrm{R}}$ represents the random forces. $\mathbf{x}_i$ and $\mathbf{v}_i$ are the positions and velocities of particle i whereas m_i is the particle's mass and $\varDelta t$ is the time step.

DPD-VV integration algorithm
1. $\mathbf{v}_i \leftarrow \mathbf{v}_i + \frac{1}{2m_i}\left(\mathbf{F}_i^{\mathrm{C}}\varDelta t + \mathbf{F}_i^{\mathrm{D}}\varDelta t + \mathbf{F}_i^{\mathrm{R}}\sqrt{\varDelta t}\right)$
2. $\mathbf{x}_i \leftarrow \mathbf{x}_i + \mathbf{v}_i\varDelta t$
3. Calculate $\mathbf{F}_i^{\mathrm{C}}\{\mathbf{x}\}, \mathbf{F}_i^{\mathrm{D}}\{\mathbf{x}, \mathbf{v}\}, \mathbf{F}_i^{\mathrm{R}}\{\mathbf{x}\}$
4. $\mathbf{v}_i^0 \leftarrow \mathbf{v}_i + \frac{1}{2m_i}\left(\mathbf{F}_i^{\mathrm{C}}\varDelta t + \mathbf{F}_i^{\mathrm{R}}\sqrt{\varDelta t}\right)$
5. $\mathbf{v}_i \leftarrow \mathbf{v}_i^0 + \frac{1}{2m_i}\mathbf{F}_i^{\mathrm{D}}\varDelta t$
6. Calculate $\mathbf{F}_i^{\mathrm{R}}\{\mathbf{x}, \mathbf{v}\}$

dependence of dissipative forces have been developed [223, 225, 226, 227, 224, 228, 229, 230]. These methods allow for the integration to be completed with an acceptable level of computing efficiency. It is well-known that the dissipative particle dynamics velocity verlet (DPD-VV) integrator [224, 231] works well for systems where the force field depends on the particles velocity, and when friction coefficients and random noise components are reduced to zero, this integrator reverts to the standard velocity-Verlet algorithm.

The DPD force field contains the conservative forces, $\mathbf{F}^{\mathrm{C}}$, the dissipative forces, $\mathbf{F}^{\mathrm{D}}$, and the random forces, $\mathbf{F}^{\mathrm{R}}$. The conservative forces, $\mathbf{F}^{\mathrm{C}}$, are non-frictional forces, namely intracellular and intercellular interactions. In *CellSim3D*, the conservative forces are the bonding forces, $\mathbf{F}^{\mathrm{B}}$, excluding the bond damping term, the angle forces, $\mathbf{F}^{\theta}$, the attractive and repulsive forces $\mathbf{F}^{\mathrm{A}}$ and $\mathbf{F}^{\mathrm{R}}$ between nodes on different cells, and the pressure force, $\mathbf{F}^{\mathrm{P}}$. The dissipative forces, $\mathbf{F}^{\mathrm{D}}$, are all the fictional forces. These are the bond damping parts of the bonded force, intermembrane friction, $\mathbf{F}^{\mathrm{F,e}}$, and medium friction, $\mathbf{F}^{\mathrm{F,m}}$. Lastly, the random force, $\mathbf{F}^{\mathrm{R}}$, is conserved Gaussian white noise, $\eta \equiv \eta(\mathbf{x}, t)$, whose origin is the thermal motion of the particles in the medium.

In DPD, a thermostat is implemented in terms of pairwise random and dissipative forces so that the system's overall momentum is conserved. Hence, it gives a better description of hydrodynamic modes that are significant in the physical approach to the equilibrium of a system. In *CellSim3D*, the random force is not considered a pairwise random force, hence we do not construct a thermostat to secure that the system's total momentum conserved. The momentum of biological systems is continuously changing as energy is transferred to the substrate and new cells are added to the system. The algorithm is listed in Table 3.1.

3.5.2 Boundary Conditions

There are three different simulation boundary conditions in *CellSim3D*. They are simulation box with a rigid wall, periodic boundary conditions (PBCs), and Less-Edward boundary conditions (LEbc). In a simulation box with rigid walls, the repulsive harmonic force between the wall and a particle close to the wall is determined in each direction as

$$\mathbf{F}_i^{\mathrm{W}} = \mathrm{k}^{\mathrm{W}} \ (|\delta \mathrm{x}_i| - \epsilon)\, \hat{\delta \mathbf{x}}_i, \tag{3.10}$$

where ϵ is the threshold distance for particles to feel the wall effect, and $\delta \mathrm{x}_i$ is the particle distance to the wall in the x-direction. We have the same formula for the y- and z-directions with the same ϵ. Since the behavior of a finite-size system can be different from an infinite-size system, sometimes it is difficult to produce results that correctly mimic the behavior of an infinite system. Using PBCs, it is possible to create a system that is bounded but free of physical walls. In simulations with PBCs, two important factors must be considered. First, atoms that leave the simulation region by one of the enclosing faces immediately return via the other face. Second, close-to-boundary interactions are possible between atoms in a nearby copy of the system and atoms in the original system [177]. If, for instance, the x coordinate is set to be between 0 and L_x, where L_x is the domain size in the x direction, we have:

- if $r_x > L_x$ or $r_x < 0$, replace it by $r_x - \lfloor \frac{r_x}{L_x} \rfloor L_x$,

where $\lfloor a \rfloor$ is the greatest integer less than or equal to a. In determining the components of the distance between pairs of atoms, the effect of periodicity on the interaction computation is:

- if $r_{ij,x} \geq L_x/2$ or $r_{ij,x} < -L_x/2$, replace it by $r_{ij,x} - \lfloor \frac{r_{ij,x}}{L_x} \rceil L_x$,

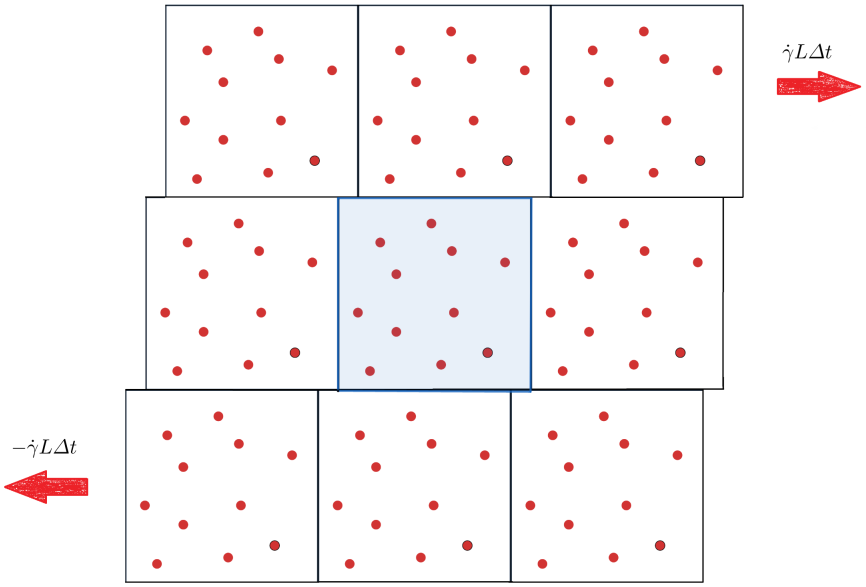

Figure 3.6: The Lees-Edwards boundary conditions are shown in the figure. The simulation box is located in the center of the cell at the center. At the same time, the upper and lower replicas are travelling in the opposite directions with speed $\dot{\gamma} L$.

where $\lfloor a \rceil$ is the nearest integer to a. The periodic boundary conditions for molecular dynamics were extended by Lees and Edwards in order to simulate a bulk system in a simple shear flow [232]. They implement this boundary condition for a system of particles with positions (r_x, r_y, r_z) and velocities (v_x, v_y, v_z) within a three-dimensional box (L_x, L_y, L_z) with a uniform shear velocity profile $\mathbf{U} = \dot{\gamma} y \mathbf{e}_x$, where $\mathbf{e}_x$ is the unity vector in the x-direction. In LEbc, particles leaving the simulation box in directions orthogonal to the velocity gradient, $\mathbf{e}_y$, are reinserted with their x-velocity enhanced by the shear velocity $\varDelta\mathbf{u} = \dot{\gamma}L_y\mathbf{e}_x$ and their positions altered by adding the time-dependent offset $d_x = t\varDelta u_x$ to their periodic image x-coordinate, where t is the duration of time that has passed from the beginning of time, Fig. 3.6. If the particles exit the box in the opposite direction, $-\mathbf{e}_y$, their periodic images are displaced by $-d_x$, and their x-velocities are reduced by the shear velocity, $\varDelta\mathbf{u}$. In LEbc, the updated positions r' and velocities v' of the particles are described as [233]

$$r'_x = \begin{cases} (r_x \bmod L_x) + d_x & \text{if } r_y \geq L_y; \\ (r_x \bmod L_x) & \text{if } 0 \leq r_y < L_y; \\ (r_x \bmod L_x) - d_x & \text{if } r_y < 0. \end{cases} \tag{3.11}$$

$$r'_y = (r_y \bmod L_y). \tag{3.12}$$

$$r'_z = (r_z \bmod L_z). \tag{3.13}$$

$$\mathrm{v}'_x = \begin{cases} v_x + \dot{\gamma}L_y & \text{if } r_y \geq L_y; \\ v_x & \text{if } 0 \leq r_y < L_y; \\ v_x - \dot{\gamma}L_y & \text{if } r_y < 0. \end{cases} \tag{3.14}$$

$$\mathrm{v}'_\mathrm{y} = \mathrm{v}_\mathrm{y}. \tag{3.15}$$

$$\mathrm{v}'_\mathrm{z} = \mathrm{v}_\mathrm{z}. \tag{3.16}$$

3.5.3 Multi-GPUs Implementation

In *CellSim3D*, spatial domain decomposition and processor communication follow the same method as in Ref. [12]. Spatial decomposition (SD) of the workload refers to partitioning the simulation box into small three-dimensional domains. We consider these domains to be a three-dimensional rectangular parallelepipeds. To reduce communication, it is preferable to set the number of processors in each dimension so that each processor's domain is as cubic as possible. In the limit of a large number of cells and particles, the communication cost of the

SD algorithm will be proportional to the surface area of the domains [12, 234, 235].

At each time step, each GPU calculates the forces and updates the positions and velocities of all cells within its domain. To compute the short-ranged pair forces between the cells, boundary cells, called ghost cells, are communicated between the neighboring processors. In every step, the positions, velocities, etc. of ghost particles are updated and communicated. There are three steps in the communication process: particle migration, ghost particle exchange, and ghost particle update [235].

As the cells pass across the domain boundaries, they are reassigned to new a processor, called particle migration. All attributes of migrated cells, including positions, velocities, coefficients of friction, stiffnesses, etc., will be sent to the new processor. By moving data in the array, the cells that have already left the domain are eliminated, and new cells are added to the end of the array. This rearranging of the GPU arrays for positions, velocities, etc., as well as for data communication between the processors are costly procedures. However, the particle migration subroutine is not executed at each time step, but rather when the neighbor list needs to be updated.

Following particle migration, the ghost cells are exchanged. A ghost cell can concurrently be a neighbor in up to three domains: a ’face’ neighbor, an ’edge’ neighbor, and a ’corner’ neighbor. The ghost particle lists are generated to restore ghost particle indices that are transferred in each direction of communication. These lists stay valid until the next neighbor list update, which occurs when a dangerous cell is detected and the neighbor list is no longer valid. Therefore, instead of scanning the full cell’s position at every time step, we only need to update the ghost particle’s position and velocity arrays and communicate them to the neighboring processors according to the ghost particle lists [12, 234, 235].

There are six communication calls between the neighboring domains, see Ref. [12]. These are the minimum necessary communications in the three spatial dimensions for the exchange of information. To maximize communication bandwidth utilization, the method combines several smaller messages into fewer larger messages [12]. Figure 3.7 depicts the communication scheme we deploy to gather required data from the neighboring GPU domains.

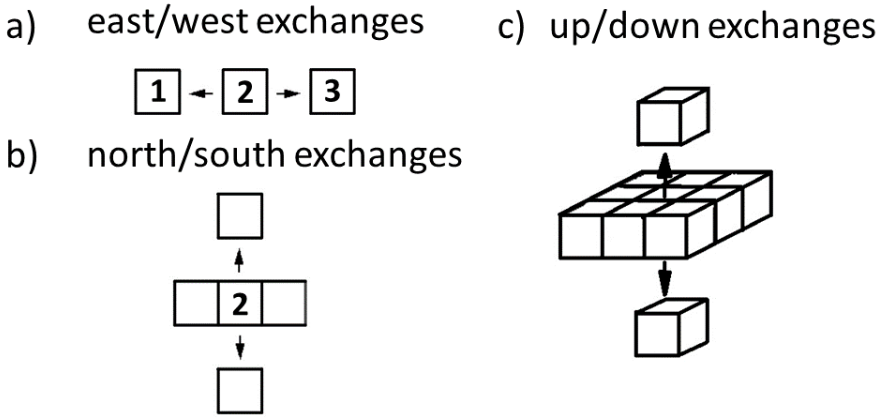

Figure 3.7: In the spatial decomposition algorithm, the mechanism by which a processor obtains adjacent atom positions. All atom positions in adjacent boxes in the (a) east/west (b) north/south (c) up/down directions can be communicated in six data exchanges. Adapted from Figure 10 in Ref. [12] with permission from Elsevier Press.

1. Each processor in the east/west dimension communicates with its neighbors. First, processors send a message to the processors in the westward direction and receive a message from the eastward direction. For example, The cells positions that processor two owns and are within a distance cutoff of processor one are put into a message buffer and send to processor one. The process is then reversed, with each processor sending to the east and receiving from the west. It continues until each processor knows the exact position of every atom within the cutoff length of its domain.

2. Now, the same process is done in the north/south dimension. Messages sent to a neighboring processor now contain not just the cells the processor owns, but also any cell positions received from the adjacent processor in the east/west communication.

3. The technique is repeated in the up/down direction in the final stage. Now, cells located

in the domain, as well as those received in the east/west and north/south communications, are communicated between processors.

This technique has a number of features that minimize the overall cost of communication in our algorithm. First, the required cells positions are collected from all the 26 surrounding domains in just 6 data exchanges. Another benefit is the reduction of data transfers. Each processor only gathers cells positions within a certain distance of its own domain. Data can be stored directly into the processor's data structure without rearranging data except for the buffered messages that must be communicated [12].

CellSim3D can take advantage of the CUDA-aware MPI libraries such as the OpenMPI library. The CUDA-aware MPI libraries provide direct GPU-to-GPU communication by utilizing NVIDIA GPUDirec technology, which includes both intra-node Peer-to-Peer transfers and inter-node Remote Data Memory Access (RDMA) [236].

3.5.4 Neighbor List Method

Setting a cutoff radius and implementing a neighbor list is the way to manage the exponential growth in pairwise force calculations. To calculate the overall force on a particle, each particle that falls outside the cutoff radius is ignored. The selection of a cutoff radius is not an easy task. The cutoff radius must neither be so large that particles interact with all other particles, nor so small that particles close enough to the particle are ignored. After selecting an appropriate cutoff radius, the neighbor list is populated by iteratively scanning all particle positions and identifying acceptable neighbors [234].

The updating of the neighbor list is an $O(n^2)$ problem, although it is not necessary to update the list at each step. Numerous approaches exist for figuring out when to perform a neighbor list update. One technique is to create a 'skin depth' outside of the cutoff radius. Every time a particle traverses the skin depth, the neighbor list is updated.

We modified the neighbor list algorithm as follows in order to extend the time between neighbor list updates. When the neighbor list is updated, the positions of the particles are stored in arrays in addition to position arrays. When a particle moves more than a buffer distance from its last recorded position, we refer to it as a 'dangerous particle'. The neighbor list must be updated whenever a dangerous particle invalidates the last neighbor list created. We therefore provide a subroutine that checks for the presence of the dangerous particles and monitors whether or not any of them invalidate the neighbor list. If the subroutine detects a dangerous particle that invalidates the neighbor list, we update the neighbor list during that simulation step [234].

Making the neighbor list is a time-consuming operation. However, having a small number of dangerous particles drastically reduces the computational effort required to construct the neighbor list. This strategy can significantly lengthen the time expected to update the neighbor list and improve simulator performance by reducing the number of neighbor list updates.

3.5.5 Simulation Units

The length scale is based on the canonical biological model of human cells, the HeLa cell [237]. HeLa cell volume is $V \approx 10^3 \mu\mathrm{m}^3$ [238, 239]. By considering the volume of the Hela as the unit of the volume in the simulation, the unit of length is $[L] \approx 10\mu\mathrm{m}$.

According to Stewart *et al.* [193], cells' interior pressures and Young's moduli of whole mitotic cells have been tested experimentally, and determined to be roughly $P = 10^{-8} N[L]^{-2}$ and $E = 1 \times 10^{-9}\,\mathrm{nN}\mu\mathrm{m}^{-2}$, respectively. Using these results as a proxy for volumetric growth, the pressure force increase rate is chosen to be $\Delta(PS) \approx 1 - 10 \times 10^{-4}[F][L]^{-2}$. The area of each cell in *CellSim3D* is approximately $5[L]^2$. Hence, the total force on the membrane due to the pressure is about $5 \times 10^{-8}\mathrm{N}$. There are more forces on the cells, and the pressure can also increase, thus, the unit of force is set to $[F] = 1\,\mathrm{nN}$. The mass is determined by comparing it to the mass of a HeLa cell, which is roughly $10^{-12}\mathrm{kg}$ [240]. Each cell is made of 180 nodes. Hence setting $[M] \approx 10^{-12}\mathrm{kg}$, the average mass of each node is $\approx 0.01[M]$. The spring constant of the bonding springs can be found through $k^{\mathrm{B}} = E\frac{A_0}{R_0} \approx 10^3[F][L]^{-1}$, where according to a mechanical cell's membrane, A_0 is its cross-sectional area and $R_0 \approx 0.1[L]$ is its equilibrium bond length.

In order to determine the possible values of adhesion and repulsion spring constants, we assume that the two spring constants may be stated as $k^{\mathrm{A}} = A\,k^{\mathrm{B}}$ and $k^{\mathrm{R}} = R\,k^{\mathrm{B}}$, where R and A are proportionality constants. Internal pressure exerts an outward force on the cell's surface, and as argued in Ref. [15], the forces of repulsion should be stronger than the forces of internal pressure. Hence, we set the repulsive constant proportional to internal pressure which is $k^{\mathrm{R}} = 100\,k^{\mathrm{B}}$. The adhesion spring constant is determined by assuming that cell membranes have a certain energy density $U_{\mathrm{adh}} = 2.5 \times 10^{-17}\,J\mu m^{-2} \approx k^{\mathrm{A}}(R_0^{\mathrm{A}} - R_0^{\mathrm{R}})^2$, where $R_0^{\mathrm{A}} \approx 2\,R_0^{\mathrm{R}} \approx 0.2$. This results in a scaling value A = 0.5.

The critical damping of the bond is defined as $\gamma_{\mathrm{int}}^{\mathrm{c}} \approx 2\sqrt{mk^{\mathrm{B}}} \approx 10$. We define the damping coefficient of the bonded intracellular force well beyond the critical damping, $\gamma_{\mathrm{int}} = 100$.

The time unit can be adjusted so that a *Drosophila* wing disc-like epithelial system is produced in 10 hours, and the time step is set to be $\Delta t = 10^{-4}[T]$. But, from a few minutes in fruit flies [241] to seven hours in hamsters [242] and up to 20 hours in humans [242], cells can have different cell cycle time. Hence, it would be insufficient if all cell types shared a single time unit. Scaling the simulation time by the average cell division time can solve this issue. Ref. [216] shows the analysis on measuring the cell division time distribution and its mean. The cell cytoplasm's viscosity, which produces membrane drag, is 10^3 Pa s [243, 240]. We are able to modify its value as an input to the package.

Table 3.2: These parameters determine the mechanical properties of each cell. They are usually adjusted to represent a variety of different cell types. *CellSim3D* uses the symbol *dagger* to represent units of Δt and $*$ units of mean cell division time, which depends on the cell types and is set to 1.0 in *CellSim3D*. For the derivation and details, please see Refs. [10, 15]

Parameter	Notation	Sim. Units	SI Units	
Nodes per cell	N_c	180	-	
Node mass	m	0.04	40	fg
Bond stiffness	k^B	1000	100	$\frac{\text{nN}}{\mu\text{m}}$
Bond damping coefficient	γ_{int}	100	0.01	$\frac{\text{g}}{\text{s}}$
Minimum pressure	$(PS)_0$	50	0.5	$\frac{\text{nN}}{\mu\text{m}^2}$
Maximum pressure	$(PS)_\infty$	65	0.65	$\frac{\text{nN}}{\mu\text{m}^2}$
Pressure growth rate	$\Delta(PS)$	0.002	2.0×10^{-5}	$\frac{\text{nN}}{\mu\text{m}^2}$
Attraction stiffness	K^A	10-2000	1-200	$\frac{\text{nN}}{\mu\text{m}}$
Attraction range	R_0^A	0.3	3	μm
Repulsion stiffness	K^R	10×10^5	10×10^4	$\frac{\text{nN}}{\text{m}}$
Repulsion range	R_0^A	0.2	2	μm
Growth count interval	-	1000	†	
Inter-membrane friction	γ_{ext}	1	10	$\frac{\mu\text{g}}{\text{s}}$
Medium friction	γ_{m}	0.4	4	$\frac{\mu\text{g}}{\text{s}}$
Time step	Δt	1.0×10^{-4}	$*$	
Threshold division volume	V^{div}	2.9	2900	μm^3

Chapter 4

In silico testing of the universality of epithelial tissue growth

The contents of this chapter have been published with the following citation: M. Mazarei, J. Åström, J. Westerholm, and M. Karttunen, *In silico testing of the universality of epithelial tissue growth*, Physical Review E, 106, L062402 (2022).

4.1 Introduction

Growth of biological matter, e.g., tumor invasion, depends on complex processes such as the mechanism(s) of proliferation, the physical properties of the microenvironment, and cellular migration that can be dominated either by single cell or collective motion [84]. Numerous experimental and computational studies have investigated the effects of biochemical regulation and mechanical factors such as cell-to-cell adhesion and friction, and cell division [244, 245, 246, 247, 76, 13, 87, 248, 88, 89]. To understand how these factors manifest in terms of both kinetics and morphology, the interfacial growth of a tissue can be characterized by a scaling analysis. This, in turn, identifies governing equations and hence leading order behavior(s).

Often, the interface width, $w(l,t)$, obeys the Family-Vicsek scaling relation [117, 118]

$$w(l,t) \sim t^{\beta} F(lt^{-\frac{1}{z}}), \tag{4.1}$$

where the exponent z describes the scaling relation between the critical time and length scales, and can be obtained from the scaling relation $z = \frac{\alpha}{\beta}$, where the exponent α characterizes the roughness of the interface. The exponent β is obtained through the scaling function $F(u) = F(lt^{-\frac{1}{z}})$ which has the following properties: There is a crossover at $u = l_*$. For $u \ll l_*$ the scaling function increases as a power law, $F(u) = u^{\alpha}$, where α is the roughness exponent. For $u \gg l_*$ the width saturates, and $F(u)$ becomes a constant [6]. With these three critical exponents, α, β and z, interfacial growth is often classified into different dynamic universality classes.

The KPZ equation is a stochastic non-linear differential equation for surface growth [249],

$$\partial_t h(x,t) = -\lambda \left[\partial_x h(x,t)\right]^2 + \nu \partial_x^2 h(x,t) + \xi(x,t), \tag{4.2}$$

where the height $(h(x,t))$ depends on position and time, and λ, ν and D are physical constants. The first term on the RHS reflects growth that occurs locally normal to the interface and renders the KPZ equation non-linear. The second term smooths the interface by surface tension ν, and the last term, $\xi(x,t)$, is Gaussian noise given by $\langle \xi(x,t) \rangle = 0$ and $\langle \xi(s,x)\xi(t,y) \rangle = 2D\delta(s-t)\delta(x-y)$. The KPZ universality class is characterized by the exponents $\alpha^{\text{KPZ}} = \frac{1}{2}$, $\beta^{\text{KPZ}} = \frac{1}{3}$, and $z^{\text{KPZ}} = \frac{3}{2}$ [249].

Mathematically, surface tension and lateral growth determine the asymptotic scaling of the KPZ equation. In some growth processes, however, surface diffusion controls the scaling behavior, and the growth process is described by the MBE model [250, 251]

$$\partial_t h(x,t) = -K\partial_x^4 h(x,t) + F + \xi(x,t), \tag{4.3}$$

where K is the surface diffusion coefficient, F is the growth rate, and $\xi(x,t)$ is Gaussian white noise. The exponents for the MBE universality class for a one dimensional interface are $\alpha^{\mathrm{MBE}} = \frac{3}{2}$, $\beta^{\mathrm{MBE}} = \frac{3}{8}$, and $z^{\mathrm{MBE}} = 4.0$.

Apparent controversy.— Brú *et al.* studied cellular growth using cells from 15 different *in vitro* cell lines and 16 *in vivo* types of tumor cells obtained from patients [13, 87]. They determined the growth to belong to the MBE universality class in all cases with exponents $\alpha = 1.5 \pm 0.15$, $\beta = 0.38 \pm 0.07$, and $z = 4.0 \pm 0.5$ thus suggesting universal growth dynamics for cells. This conclusion was strongly criticized by Buceta and Galeano [90] who dismissed universality of tumor growth dynamics stating serious flaws in Brú *et al.*'s scaling analysis. In their rebuttal Brú *et al.* [248] restated their conclusions and wrote *"the characteristics of MBE dynamics discussed in Brú et al. (2003,1998) have not only been rigorously demonstrated but have served as the basis for a successful antitumor therapy currently under development."* A recent study of growth of different brain tumors *in vivo* using fractal and scaling analysis shows similarities with some of the results of Brú *et al.* [252].

In contrast to MBE-like dynamics, Huergo *et al.* [88, 89, 4] reported KPZ scaling for both linearly and radially spreading interfaces of HeLa (cervix cancer) and Vero cell colonies. Galeano *et al.* studied the development of plant cell species *Brassica oleracea* and *B. rapa* under various growing conditions and obtained $\alpha = 0.86 \pm 0.4$, and $z = 5.0$ [253]. Santalla *et al.* [254] grew colonies of *B. subtilis* and *E. coli* using a high agar concentration regime with various nutrients and discovered branching interfaces with exponents $\beta = 0.5$ and $\alpha = 0.75$ that are inconsistent with both MBE and KPZ.

Substrate disorder can also influence growth dynamics. Vicsek *et al.* [255] studied the growth of *E. coli* and *B. subtilis* colonies and found the roughness exponent $\alpha = 0.78 \pm 0.07$ which is inconsistent with both the KPZ and MBE models as well as with the quenched KPZ (qKPZ) model [6] that includes disorder. It has also been demonstrated that the behavior of bacterial colonies in the medium-to-high nutrient concentration regime can be very rich due to the appearance of quenched disorder in growth patterns [256]. In that context, Huergo *et al.* also examined the 2D growth dynamics of quasilinear Vero cell colony fronts in a methylcellulose-containing culture medium. Their scaling analysis yielded $\alpha = 0.63 \pm 0.04$, $\beta = 0.75 \pm 0.05$, and $z = 0.84 \pm 0.05$, suggesting qKPZ dynamics [83].

On the computational and theoretical side, Santalla and Ferreira [92] used an off-lattice Eden model modified to account for nutrient diffusion. Under scarce nutrient supply, they observed initially a KPZ regime that transitioned via a qKPZ transient to unstable growth. Block *et al.* studied the growth of 2D cellular monolayers for a class of cellular automaton models. Their results suggest KPZ dynamics over a wide range of parameters and different cell migration dynamics [77] contradicting the MBE dynamics reported by Brú *et al.* [13]. Another contradiction was reported by Azimzade *et al.* who developed a tumor growth model based on the non-linear Fisher-Kolmogorov-Petrovsky-Piskunov equation, a reaction-diffusion equation, to investigate the impact of the cellular environment and spatial correlations on tumor invasion [91]. They concluded that kinetic growth models, such as KPZ, cannot characterise tumor invasion fronts, and that the structure of the tumor interface depends intimately on the initial conditions [91].

4.2 METHODS

4.2.1 CellSim3D Simulator and Model

A large number of different models has been used to describe cellular growth [257]. Here, we use the *CellSim3D* off-lattice growth model and simulator to study epithelial tissue growth [10, 258]. In this model, cells can migrate, deform, divide, and interact with each other and their environment mechanically via adhesion and friction. Its 2D version has been shown to produce, e.g., cell-cell force distributions, force dipoles, spontaneous orientation of cells in the direction of highest stiffness and cellular migration in agreement with experiments [259]. The analysis below uses averages over 10 independent simulations. In brief, in *CellSim3D*, epithelial tissues can be modeled as quasi-2D systems of 3D cells confined into a plane, corresponding to the experimental confinement of cells between two plates; the bottom plate models basal tissue and the top plate prevents excessive buckling. Details of the code, model and parameters are provided in SI. The code is open source at `https://github.com/SoftSimu/CellSim3D`.

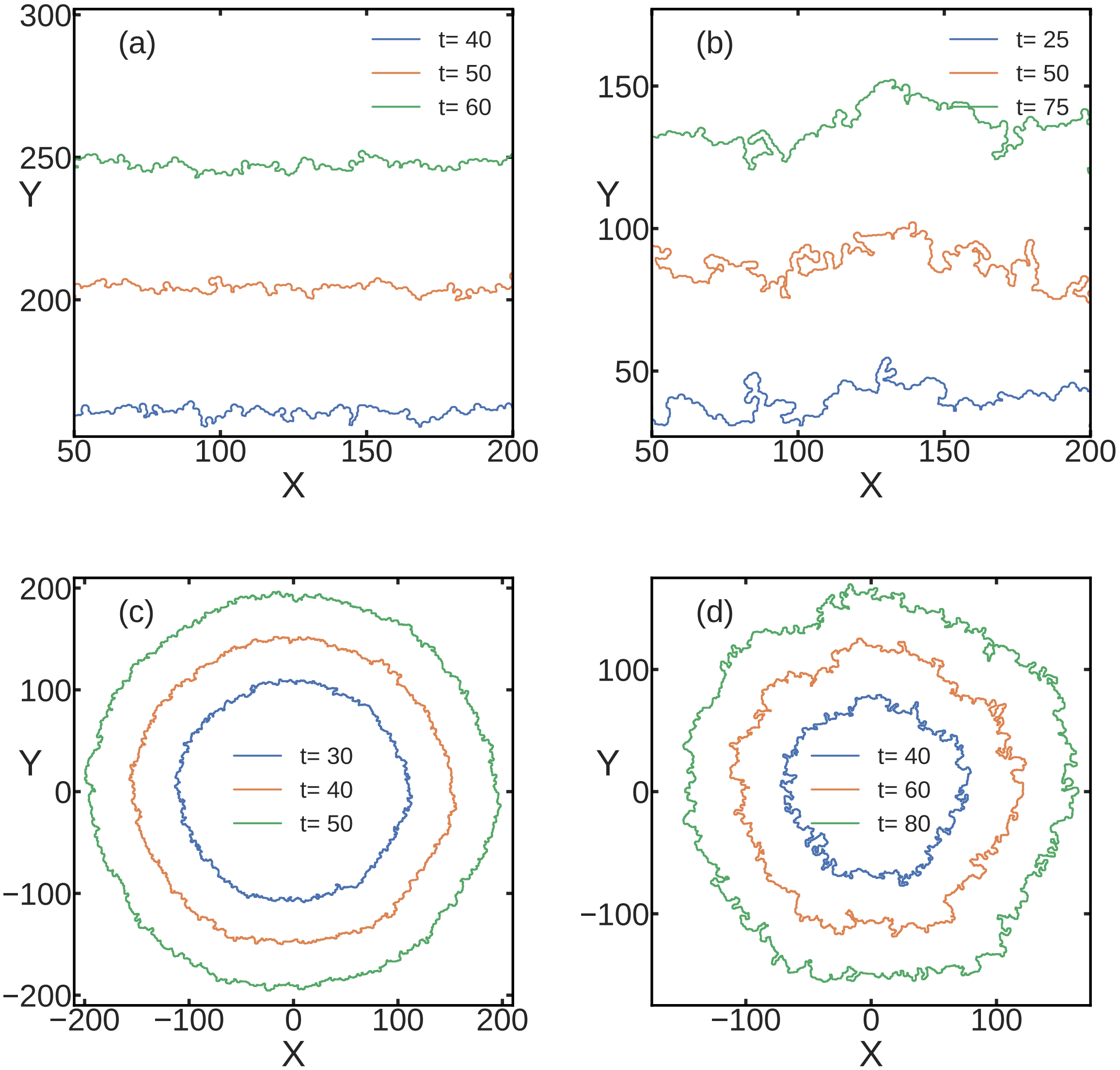

Figure 4.1: Interface evolutions of cell colonies starting from a horizontal line and a radially expanding interface. (a) Line configuration at weak (10) and (b) strong cell-cell adhesion (2000). (c) Radially expanding interface with at weak (10) and (d) strong adhesion (2000). All interfaces have overhangs. Scaling analysis was done using overhang-corrected interfaces [6]. For the units, see Table 4.1.

4.2.2 Interface Scaling

The interface width is defined as the standard deviation of height over a length scale l at time t as [6]

$$w(l,t) = \left\{ \frac{1}{N} \sum_{i=1}^{N} [h_i(t) - \langle h_i \rangle_l]^2 \right\}_L^{\frac{1}{2}}, \tag{4.4}$$

where N is the number of sites in a contour length of size l, and L is the entire contour length, which increases with time as $L = 2\pi\langle h(t)\rangle$ for radially expanding fronts and is constant and equal to the size of the box perpendicular to the growth direction for linear fronts. For radially expanding fronts, $h_\mathrm{i}(t)$ is the distance from the center of mass to the point i of the interface at time t, $\langle h_\mathrm{i}\rangle_l$ is the local average of the subsets of arc length l, and $\{\cdot\}_L$ is the overall average. We complement the universality class analysis by an examination of the structure factor,

$$S(k,t) = \langle \hat{h}(k,t)\hat{h}(-k,t)\rangle, \tag{4.5}$$

where k is the wavenumber, and $\hat{h}(k,t)$ is the Fourier transform of the interface profile $h(x,t)$ [6]. The advantage of this method over the real space is that only long-wavelength modes contribute to its scaling. Hence, it is less affected by finite-size effects [260, 261]. This method provides the global roughness exponent α and the dynamic exponent z via the Family-Vicsek scaling form for $S(k,t)$,

$$S(k,t) = k^{-(2\alpha+1)} s(kt^{\frac{1}{z}}), \text{ where} \tag{4.6}$$

$$s(u = kt^{\frac{1}{z}}) = \begin{cases} \text{const} & \text{for } u \gg 1; \\ u^{2\alpha+1} & \text{for } u \ll 1. \end{cases} \tag{4.7}$$

At $u = 1$ there is a crossover, for $u \gg 1$ the curves measured at different times collapse and for $u \ll 1$ they split.

4.3 Results

4.3.1 Linear Interfaces

We first consider the growth of linear fronts at two different adhesion strengths, 10 (weak) and 2000 (strong), see Table 4.1 for parameters. The initial configurations had a line of 240 cells, and the final populations consisted of ≈200,000 cells. Snapshots are shown in Fig. 4.1. As this figure shows, increasing the cell-cell adhesion changes the morphology of the colony and the interface. Figure 4.2a shows that the interfaces grow at constant velocities with the growth rate decreasing with increasing adhesion.

Next, the box counting method was utilized to determine the fractal dimensions (d_{f}) of the interfaces for both line configurations (triangles) and radially growing (circles) systems. Figure 4.2b shows that d_{f} is in the same range for all simulations. In both geometries, however, d_{f} is slightly higher for the case of strong adhesion. This is consistent with the experiments of Torres Hoyos *et al.* [252] who reported smaller d_{f} for malignant and invasive cancer cells as compared to the benign and more solid (higher adhesion) tumors.

We investigate the scaling behavior by plotting the width scaling function $F(u)$ in Eq. 4.1 and the structure scaling function $s(u)$ in Eq. 4.6 at three different time points in order to see if they collapse for given values of α, β and z. Instead of relying only on a visual inspection, we calculated the Chi-squared statistics (Eq. 4.19) similar to the concept of the maximum likelihood estimator for equality of two distributions. Figures 4.3a-d show the scaling results for line growth both via the width function (Eq. 4.1) and the structure factor (Eq. 4.6). Both scaling functions suggest KPZ dynamics; using the Family-Vicsek relation for the structure factor, (Eq. 4.6) Figs. 4.3a,b, and width, Eq. 4.1, the data collapses to a single function using the KPZ exponents (Fig. 4.3d). The Chi-squared statistics (Eq. 4.19) and goodness-of-fit p-values indicate better collapse for the KPZ than for the MBE exponents, see Tables 4.2 to 4.5. Figure 4.5 shows that interface roughness, $w(t)$, follows a power-law t^{β} with $\beta^{\mathrm{weak}} = 0.28 \pm 0.01$ and $\beta^{\mathrm{strong}} = 0.25 \pm 0.02$ for weak and strong adhesion, respectively. Figures 4.6 and 4.7 show

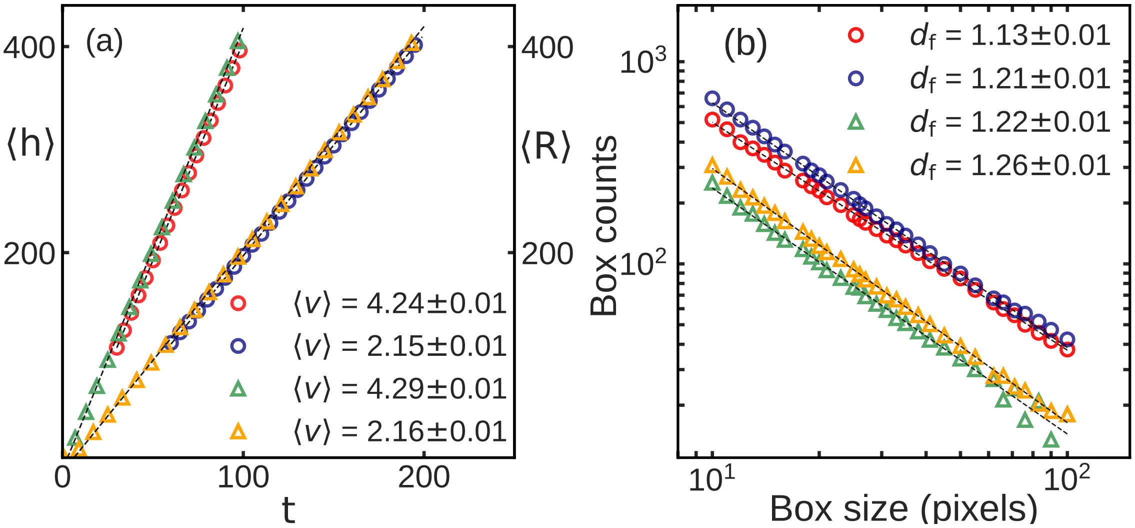

Figure 4.2: (a) Velocity ($\langle v \rangle$) of the interface determined from the mean colony radius $\langle R \rangle$ and the mean interface height $\langle h \rangle$ vs. time for different cell-cell adhesion strengths. Radially expanding interface: (red circles) at weak (10) and (blue circles) strong adhesion (2, 000). Line configuration: (green triangles) at weak and (orange triangles) at strong adhesion. (b) The fractal dimension (d_f) determined by plotting box counts vs. box size. For radially expanding interface: (red circles) at weak (10) and (blue circles) strong adhesion (2, 000). For line configuration: (green triangles) at weak and (orange triangles) strong adhesion. For units, see Table 4.1.

the local and global roughness exponents. As the figures show, determining the roughness exponent is questionable especially in the case of weak adhesion. The value $\alpha_{\mathrm{loc}}^{\mathrm{strong}} = 0.62 \pm 0.02$, was calculated using width, and $\alpha_{\mathrm{glob}}^{\mathrm{weak}} = 0.75 \pm 0.04$ and $\alpha_{\mathrm{glob}}^{\mathrm{strong}} = 0.52 \pm 0.02$, using the structure factor. As the results show, α_{glob} decreases with increasing adhesion.

4.3.2 Radial Interfaces

Next, we focus on radially expanding isotropic fronts. The initial configuration was one cell at the center of the simulation box and the final populations were ≈200,000 cells. We define $R_\mathrm{i}(t)$ to be the distance from the center of mass of the colony to the ith site at the interface. Snapshots at different times and adhesion strengths are shown in Fig. 4.1; increasing the adhesion between the cells changes the colony morphology and increases overhangs. The radii grow at constant velocities, $\langle v \rangle = 4.24 \pm 0.01$ for weak and $\langle v \rangle = 2.15 \pm 0.01$ for strong adhesion, Fig. 4.2a. As in the linear case, increasing the adhesion causes the front velocities to decrease. Again, the

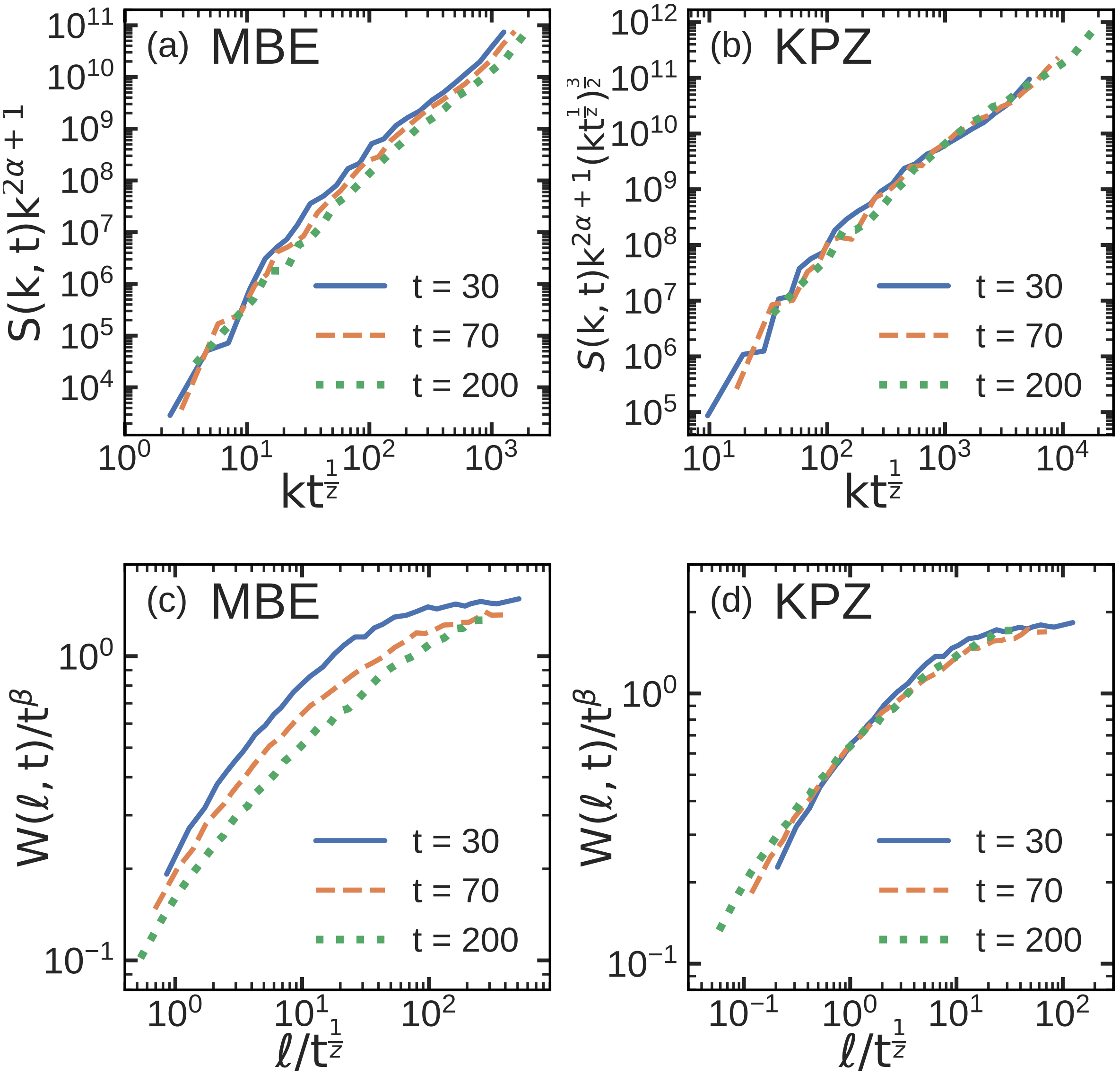

Figure 4.3: Data collapse for line growth at high adhesion at three different times. (a) Using the structure factor (Eq. 4.6) and MBE exponents, $\alpha^{\text{MBE}} = \frac{3}{2}$ and $z^{\text{MBE}} = 4$. (b) With KPZ exponents, $\alpha^{\text{KPZ}} = \frac{1}{2}$ and $z^{\text{KPZ}} = \frac{3}{2}$. The y-axis is scaled with the factor $(\mathrm{k}t^{\frac{1}{z}})^{\frac{3}{2}}$ to have the same range as MBE scaling. (c) Using the Family-Vicsek relation for width (Eq. 4.1) with MBE exponents, $\beta^{\text{MBE}} = \frac{3}{8}$ and $z^{\text{MBE}} = 4$, and (d) with KPZ exponents, $\beta^{\text{KPZ}} = \frac{1}{3}$ and $z^{\text{KPZ}} = \frac{3}{2}$. For units, see Table 4.1.

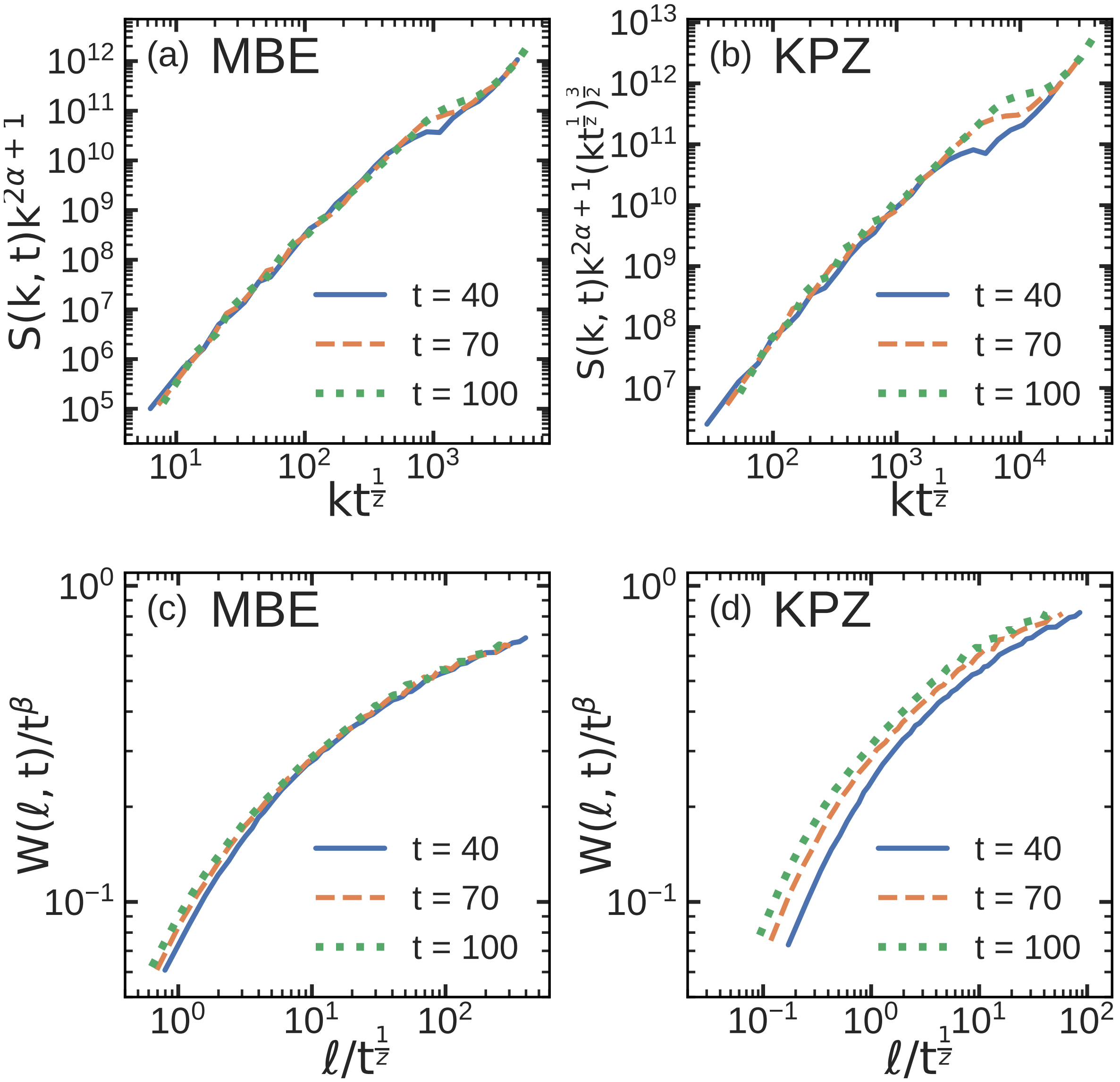

Figure 4.4: Data collapse for the radially growing interface at low adhesion at three different times. (a) Using the structure factor (Eq. 4.6) with MBE, $\alpha^{\text{MBE}} = \frac{3}{2}$ and $z^{\text{MBE}} = 4$ and (b) KPZ exponents, $\alpha^{\text{KPZ}} = \frac{1}{2}$ and $z^{\text{KPZ}} = \frac{3}{2}$. The y-axis is scaled with the factor $(\text{kt}^{\frac{1}{z}})^{\frac{3}{2}}$ to have the same range as MBE scaling. (c) Using the Family-Vicsek relation for width (Eq. 4.1) with MBE exponents, $\beta^{\text{MBE}} = \frac{3}{8}$ and $z^{\text{MBE}} = 4$, and (d) with KPZ exponents, $\beta^{\text{KPZ}} = \frac{1}{3}$ and $z^{\text{KPZ}} = \frac{3}{2}$. For units, see Table 4.1.

fractal dimension (Fig. 4.2b) shows slight increase with increasing adhesion, $d_{\mathrm{f}}^{\mathrm{weak}} = 1.13 \pm 0.01$ and $d_{\mathrm{f}}^{\mathrm{strong}} = 1.21 \pm 0.01$.

Figures 4.4a-d show the scaling results for radial growth both through the width function (Eq. 4.1) and structure factor (Eq. 4.6). Using the Family-Vicsek relation for width (Fig. 4.4c) with MBE exponents displays good collapse. In addition, the structure factors at different times show good collapse with MBE exponents, see Tables 4.6 to 4.9.

Figure 4.8 shows that fitting the width vs time gives the growth exponents $\beta^{\mathrm{weak}} = 0.40 \pm 0.04$ and $\beta^{\mathrm{strong}} = 0.42 \pm 0.06$, For varying adhesion strengths, the local roughness exponent, α_{loc}, are all within the same range: $\alpha_{\mathrm{loc}}^{\mathrm{weak}} = 0.66 \pm 0.01$ and $\alpha_{\mathrm{loc}}^{\mathrm{strong}} = 0.7 \pm 0.01$, Fig. 4.9. The scaling exponent α_{glob}, measured from the structure factor, shows a decrease with increasing adhesion strength, $\alpha_{\mathrm{glob}}^{\mathrm{weak}} = 0.95 \pm 0.04$ and $\alpha_{\mathrm{glob}}^{\mathrm{strong}} = 0.71 \pm 0.02$, Fig. 4.10.

Finally, to test the generality of the above observations, cell-medium friction, intermembrane friction, cell division rules, and the number of cell types with different stiffness were tested using the radially growing system. Figure 4.11 shows that α_{glob}, is insensitive to changes in factors such as cell-medium friction, intermembrane friction, cell division rules, and the number of cell types with different stiffness. These results suggest that dynamics of the radially growing colonies are well described by MBE-like scaling when at weak cell-cell adhesion.

4.4 Conclusions

Our simulations indicate that weak cell-cell adhesion and an isotropically growing colony display MBE-like scaling for the boundary roughness. This is consistent with the experiments of Brú *et al.* [13]; we digitized their data and show its scaling in Fig. 4.12. In contrast, a colony growing from a single line of cells, and with strong cell-cell adhesion displays KPZ-like scaling. This is in agreement with the experiments of Huergo *et al.* [88]. In all the studied cases the fractal dimensions of the interface are within the range 1.13–1.26, which is also consistent with prior experiments [13, 88, 89, 4, 253], regardless of the growth scaling behavior.

All the studied cases show linear growth with constant velocity. This is consistent with experiments: Brú *et al.* reported radially spreading cell colonies to exhibit exponential growth in the early stages followed by linear growth [13]. Huergo *et al.* showed that once the number of cells exceeds 700–1,000, radially spreading colonies grow with a constant velocity [89, 4]. Constant velocity also applies for line growth [88]. Physically, these data suggest that cells are partially contact-inhibited and that most activity occurs within a limited band along the interface challenging the notion of Gomperzian growth of cancer [262]. Experiments by Costa *et al.* indicate that *in vitro* cultivated cells may exhibit sigmoidal growth [245].

Finally, it can be assumed that the first multi-cellular life-forms were rather simple cell colonies. It is interesting to speculate that if cell-colony growth dynamics would be rigidly confined to a single universality class, adaptive evolution would likely be significantly harder in contrast to more versatile growth dynamics. This is consistent with earlier results in the sense that very rich growth behavior and diverse tissues appear with modest changes, and, e.g., non-trivial dependencies in initial conditions, nutrients, apoptosis, disorder and mechanical forces from various sources cause changes in both quantitative and qualitative behaviors, see, e.g., Refs. [244, 52, 91, 258, 259].

CellSim3D assumes that adhesion molecules are distributed uniformly over the cell surface. This is, however, not necessarily the case in real cells since cell polarity may affect their distribution and activity [263, 264, 265]. Polarized cells may exhibit directional differences in their mechanical properties and cell-cell interactions, which may influence the dynamics of tissue roughness. Work is in progress to address such issues.

Acknowledgments

We thank the Natural Sciences and Engineering Research Council of Canada (MK), Canada Research Chairs Programs (MK) and Western University's Science International Engagement Fund (MM) for financial support. Computational resources were provided by the Finnish Grid and Cloud Infrastructure FGCI, funded by the Academy of Finland.

4.5 Supplemental Material

4.5.1 The *CellSim3D* model

The CellSim3D model [10, 258] is a 3D generalization of the 2D model of cell division originally introduced by Mkrtchyan, Åström, and Karttunen [15]. In *CellSim3D* cells are defined as a set of interconnected nodes on the surface of a spherical C180 fullerene. The force field consists of bonded and non-bonded forces defined as

$$\mathbf{F} = m\mathbf{r} = \mathbf{F}^{\mathrm{B}} + \mathbf{F}^{\theta} + \mathbf{F}^{\mathrm{P}} + \mathbf{F}^{\mathrm{R}} + \mathbf{F}^{\mathrm{A}} + \mathbf{F}^{\mathrm{F}} + \eta, \tag{4.8}$$

where $\mathbf{F}^{\mathrm{B}}$ is a damped harmonic oscillator force between neighboring nodes, $\mathbf{F}^{\theta}$ is the angle force which preserves cell curvature. These two forces are bonded, and the rest are non-bonded. $\mathbf{F}^{\mathrm{R}}$ and $\mathbf{F}^{\mathrm{A}}$ are the repulsive and attractive force between C180 nodes in different cells, respectively. They are approximated by harmonic potentials with different spring constants and cutoffs. The model has been shown to produce versatile behavior in agreement with experiments [15, 10, 258, 259]. We discuss some of the main features below.

Damped harmonic oscillator and angle force in *CellSim3D*

Harmonic potentials are used to approximate bonded interactions between nearest neighbors in the same cell. Each node on a cell has a bonding force applied by its three neighbors. The force between a node i and its bonded neighbors j is defined as

$$\mathbf{F}_i^{\mathrm{B}} = \sum_{j=1}^{3} [k_{ij}^{\mathrm{B}}\, \hat{\mathbf{b}}_{ij}\, (R_{ij} - R_{ij}^{0}) - \gamma_{\mathrm{int}} \mathbf{v}_{ij}] \tag{4.9}$$

where R^0_{ij} represents the equilibrium bond length and $\mathbf{v}_{\mathrm{ij}}$ represents the relative velocity between adjacent nodes i and j. The oscillations of bonds are dampened by the coefficient of friction γ_{int}, and the spring constant $k^{\mathrm{B}}_{\mathrm{ij}}$ is constant for all bonds. Cell curvature is maintained via the angle force, $\mathbf{F}^{\theta}$, a harmonic force exerted on three nodes i, j, and k that acts against angle deformation. It is defined as

$$\mathbf{F}^{\theta}_{\mathrm{i}} = \frac{1}{2}\sum_{j}\sum_{k\neq i} - k^{\theta}_{ijk}\,\nabla_{\mathbf{x}i}\,(\theta_{ijk} - \theta^{0}_{ijk})^2 \tag{4.10}$$

where θ^0_{ijk} is the equilibrium angle between nodes i and j and k is the angle spring constant, $k^{\theta}_{\mathrm{ijk}}$, considered constant over the cell surface for simplicity.

Adhesion, repulsion and intermembrane friction in *CellSim3D*

Adhesion forces in living cells are generated by adhesive bonds between Cell Adhesion Molecules (CAMs) on the surfaces of neighboring cells [266, 267, 268]. There are numerous types of adhesion molecules, including integrins, selectins, cadherins, and the IgSuperfamily [268, 269]. In focused regions of a cell when CAMs concentrations are elevated, there may be an increase in interaction between adjacent cells and the substrate [50]. Ligands allow CAMs to bind together.

Adhesion can be modeled mechanically. In *CellSim3D*, each surface node of a cell functions as an adhesive site, replicating the behavior of CAMs. Several biological factors affect the stability, density, and position of these junctions on the surface of a cell, but we will treat them as if they are constant and uniform [10]. Within the framework of the mechanical cell approximation, we will assume that the interactions of the various CAMs may be averaged into a uniform short range interaction throughout the cell surface. This uniform interaction is segmented into adhesion, repulsion, and intermembrane friction. All sites are considered to possess identical adhesion and repulsion strengths. Attractive and repulsive intermembrane interactions on node i of cell m are defined as

$$\mathbf{F}^{\mathrm{A}}_{i,m} = \sum_n \sum_j \begin{cases} k^{\mathrm{A}}\,(r_{ij,n} - R^{\mathrm{A}}_0)\hat{\mathbf{r}}_{ij,n} & \text{if } r_{\mathrm{ij,n}} < R^{\mathrm{A}}_0\ ; \\ 0 & \text{if } r_{ij,n} \geq R^{\mathrm{A}}_0\ . \end{cases} \tag{4.11}$$

and

$$\mathbf{F}^{\mathrm{R}}_{i,m} = \sum_n \sum_j \begin{cases} -k^{\mathrm{R}}\,(r_{ij,n} - R^{\mathrm{R}}_0)\hat{\mathbf{r}}_{ij,n} & \text{if } r_{ij,n} < R^{\mathrm{R}}_0\ ; \\ 0 & \text{if } r_{ij,n} \geq R^{\mathrm{R}}_0\ . \end{cases} \tag{4.12}$$

where k^{A} and k^{R} are the attractive and repulsive spring constants, respectively, R^{A}_0 and R^{R}_0 are the corresponding attraction and repulsion equilibrium bond lengths and cutoffs, and $r_{ij,n}$ is the vector pointing from the node i on cell m to node j on cell n. $\mathbf{F}^{\mathrm{F}}$ is the friction term decomposed into viscous drag due to the medium approximating the interactions between the cell and the extracellular matrix, and intermembrane friction. In *CellSim3D*, the medium is a simple fluid and the viscous drag from the media is the only interaction between cells and the medium. The viscous drag from the media on the node i of cell m is defined as

$$\mathbf{F}^{\mathrm{F,m}}_{i} = -\gamma_m\,\mathbf{v}_i \tag{4.13}$$

where γ_{m} represents the drag coefficient. The intermembrane friction is proportional to the component of the relative velocity tangential to the surface of the cells and defined [10] as

$$\mathbf{F}^{\mathrm{F,e}}_{\mathrm{i,m}} = \sum_n \sum_j \begin{cases} -\gamma_{\mathrm{ext}}\,\mathbf{v}^{\tau_{\mathrm{m}}}_{ij} & \text{if } r_{ij,n} < R^{\mathrm{A}}_0\ ; \\ 0 & \text{if } r_{ij,n} \geq R^{\mathrm{A}}_0\ . \end{cases} \tag{4.14}$$

where γ_{ext} is the intermembrane friction coefficient, assumed to be constant across cells, and $\mathbf{v}^{\tau_{\mathrm{m}}}_{ij}$ is the tangential component of the relative velocity to the surface of cell m at $\mathbf{x}_i$. Together attractive, repulsive, and friction terms approximate inter-membrane interactions mediated by cell adhesion molecules [47, 185, 269, 270, 271]. $\mathbf{F}^{\mathrm{P}} = PS\hat{\mathbf{n}}$ is the growth force coming from the osmotic pressure within cells and the cell's internal pressure [47], where PS represents the force resulting from the cell's internal pressure and $\hat{\mathbf{n}}$ is the cell surface normal. Finally, $\eta \equiv \eta(\mathbf{x}, t)$, is Gaussian white noise given by $\langle \eta(x,t) \rangle = 0$ and $\langle \eta(s,x)\eta(t,y) \rangle = 2D\delta(s-t)\delta(x-y)$.

Cell growth and division

In *CellSim3D*, growth is induced by increasing the internal pressure, as determined by experimental measurements [193]. At each time step, the internal pressure is incremented, resulting in a increase in the pressure force [272, 10]. As a result, the cell volume gradually increases, $V = V_0 + \mathit{\Delta} V$, and once it exceeds the threshold value, V_{div}, the cell can divide into two new symmetric or asymmetric daughter cells depending on the chosen division rule [211]. In this work, we consider that the daughter cells are symmetric [273, 274].

The cell division plane's position can be either through the cell's center of mass or through another randomly chosen point inside the cell. The random point might be different for each cell, resulting in asymmetric division. The division plane's orientation can also be set using a variety of rules. According to Hertwig's rule, the division plane is perpendicular to the longest axis of an ellipsoidal cell and passes through the center of mass [214]. Errera's rule asserts that the division plane must contain the shortest path travelling through the center of mass of a cell [215]. The division plane can also be randomly oriented. In *CellSim3D*, in the case of full 3D tissue, the division plane vector is chosen randomly from a unit sphere.

Modeling epithelial tissue

Since epithelium may be considered as a 2- or quasi-2-dimensional material, we have to confine the cells to a plane; quasi-2-dimensional means that the cells themselves are fully three dimensional but the growth is planar only. Epithelial tissue is then generated by using two (virtual) plates that prevent buckling; the distance between the confining top and bottom plates was set to 1.8. We follow the same approach as in Madhikar *et al.* [258].

No friction forces exist between the plates and the cells. The only force from the plates is the repulsive force in the direction normal to the plates, that is, the positive z-direction for the bottom plate and the negative z-direction for the top plate. In addition, the *CellSim3D* cell division algorithm also adjusted for the formation of epithelium [258]. The software receives an optional vector defining the normal to the epithelial plane in space. The plane of the division furrow is then sampled from a sphere in the plane indicated by the normal vector. The volume threshold for a cell to divide is set to 2.90 in this study. For the units, please see Table 4.1.

Parameterization

The parameters used in the simulations are listed in Table 4.1. These parameters are based on the properties of HeLa cells for parameter mapping. For further details and their derivation about the *CellSim3D* force field, methodology, and parameter mapping, please see Refs. [15, 10].

4.5.2 The *CellSim3D* software

CellSim3D allows for simulations of fully 3-dimensional as well as 2-dimensional cellular systems using single consumer-grade Nvidia GPUs; the code is currently limited to Nvidia GPUs since it is written in CUDA. The code is open source and available at `https://github.com/SoftSimu/CellSim3D`, it is compatible with CUDA 5.0 and later. As for its performance, even an older generation GPU such as a GTX 970 or GTX 980 can easily simulate systems up to 100,000 cells. A modern Nvidia RTX 3080 increases the number to about 1,000,000 and a multi-GPU version is currently being developed. The simulation setup is done using a standard JSON file The simulator stores the outputs as both ASCII and binary files. For efficient and consistent Input/Output, the next edition of the software will include the HDF5 format [275].

The integrator is based on the work of Besold *et al.* [224] who developed a modified velocity-Verlet integrator for Dissipative Particle Dynamics simulations [224, 276]. The algorithm is described in Ref. [10]. For cell geometry, currently, the simulator is compatible only with the C180 fullerene geometry. Future updates will provide more options for selecting the geometry.

4.5.3 Analysis methods

The interface local width function, $w(l,t)$, is defined as the standard deviation of the front height, $h(x,t)$, over a length scale l at time t as [6]

$$w(l,t) = \left\{ \frac{1}{N} \sum_{i=1}^{N} [h_i(t) - \langle h_i \rangle_l]^2 \right\}_{\mathrm{L}}^{\frac{1}{2}}, \tag{4.15}$$

For small length scales the width function behaves as follows

$$w(l,t) \sim l^{\alpha_{\mathrm{loc}}} \tag{4.16}$$

where α_{loc} is the local roughness exponent. By replacing l with the system size L, the value of $w(L,t)$ for $t \ll t_s$, where t_s is the roughness saturation time, is expected to increase as

$$w(L,t) \sim t^{\beta} \tag{4.17}$$

where β is the growth exponent [6]. We supplement the universality class analysis by an examination of the structure factor, $S(k,t)$, of the interface,

$$S(k,t) = \langle \hat{h}(k,t)\hat{h}(-k,t) \rangle, \tag{4.18}$$

The linear interface roughness, $w(t)$, follows the power-law t^{β} with $\beta^{\mathrm{weak}} = 0.28 \pm 0.01$, for weak adhesion and $\beta^{\mathrm{strong}} = 0.25 \pm 0.02$, for strong adhesion, Fig. 4.5. The local roughness exponents, α_{loc}, are within the same range for different adhesion strengths in the case of linear interface: $\alpha_{\mathrm{loc}}^{\mathrm{weak}} = 0.59 \pm 0.01$ for weak adhesion and $\alpha_{\mathrm{loc}}^{\mathrm{strong}} = 0.62 \pm 0.02$ for strong adhesion, Fig. 4.6, The global roughness exponent, α_{glob}, of the linear growing interface was calculated via structure factor analysis, $\alpha_{\mathrm{glob}}^{\mathrm{weak}} = 0.75 \pm 0.04$ and $\alpha_{\mathrm{glob}}^{\mathrm{strong}} = 0.52 \pm 0.02$, Fig. 4.7. The width functions of the circular interface versus time t^{β} are displayed in Fig. 4.8: $\beta^{\text{weak}} = 0.40 \pm 0.04$ for weak adhesion and $\beta^{\text{strong}} = 0.42 \pm 0.06$ for strong adhesion. The local roughness exponents, α_{loc}, for circular interface are $\alpha_{\text{loc}}^{\text{weak}} = 0.66 \pm 0.01$ for weak adhesion and $\alpha_{\text{loc}}^{\text{strong}} = 0.7 \pm 0.01$ for strong adhesion, Fig. 4.9. Finally, For circular interfaces, we find $\alpha_{\text{glob}}^{\text{weak}} = 0.95 \pm 0.04$ and $\alpha_{\text{glob}}^{\text{strong}} = 0.71 \pm 0.02$, Fig. 4.10.

4.5.4 Chi-squared test

For graphs in Figs. 4.3 and 4.4 of the manuscript, each point has a vertical error bar as each point was measured ten times for fixed values of l, t and k. Each time point is regarded as the reference set of values, x_{ref}, and the Chi-squared, $\tilde{\chi}^2$, is calculated as

$$\tilde{\chi}^2 = \sum_i \frac{(x_{\text{test},i} - x_{\text{ref},i})^2}{\sigma_{\text{ref},i}^2} \tag{4.19}$$

in order to see how well the other point in time x_{test} is explained by the reference set, the null hypothesis being that x_{test} is the same as x_{ref}. Numerically, the abscissa values for x_{ref} are binned and x_{test} is assigned to the corresponding bin if the bin exists (abscissa values of x_{test} outside the abscissa range of x_{ref} are discarded). Tables 4.2 to 4.9 show the results of the $\tilde{\chi}^2$ tests on the graphs in Figs. 4.3 and 4.4 of the manuscript. The tables also include the p-values, which show the probability of getting test results close to extremes of the results of the reference set of values under the null hypothesis. The null hypothesis is rejected and the test set and reference set are not the same if the p-values are close to zero.

4.5.5 Analyses on Brú's data set

Data from Fig. 3 of Brú *et al.* [13] was digitized with the WebPlotDigitizer program [277]. Figure 4.12 shows the result from using the Family-Vicsek relation to scale the width function by MBE (Fig. 4.12a) and KPZ (Fig. 4.12b) exponents. MBE exponents show a better collapse than KPZ exponents, as Brú *et al.* stated in their study. However, we cannot obtain a full collapse for the width functions at different times with MBE exponents, implying that the development dynamics of cell-colony interfaces do not perfectly fit into the MBE universality class. The similar conclusion can be made about Huergo *et al.* results [88, 89, 4]. Although they concluded that their data reveal a KPZ growth dynamics for cell-colony growth, their works do not exhibit a full width function or structure factor collapse [88, 89, 4].

Table 4.1: Each cell's mechanical properties are determined by the values indicated here. They are usually subtly altered to represent different types of cells. The mechanical properties of cells addressed in this work are listed in the table. The symbol † indicates units of Δt and $*$ units of mean time to cell division, which varies between cell types and is set to 1.0 in *CellSim3D*. For more details and their derivation, please see Refs. [10, 15]

Parameter	Notation	Sim. Units	SI Units	
Nodes per cell	N_c	180	-	
Node mass	m	0.04	40	fg
Bond stiffness	k^B	1000	100	$\frac{\mathrm{nN}}{\mu\mathrm{m}}$
Bond damping coefficient	γ_int	100	0.01	$\frac{\mathrm{g}}{\mathrm{s}}$
Minimum pressure	$(PS)_0$	50	0.5	$\frac{\mathrm{nN}}{\mu\mathrm{m}^2}$
Maximum pressure	$(PS)_\infty$	65	0.65	$\frac{\mathrm{nN}}{\mu\mathrm{m}^2}$
Pressure growth rate	$\Delta(PS)$	0.002	2.0×10^{-5}	$\frac{\mathrm{nN}}{\mu\mathrm{m}^2}$
Attraction stiffness	K^A	10-2000	1-200	$\frac{\mathrm{nN}}{\mu\mathrm{m}}$
Attraction range	R_0^A	0.3	3	μm
Repulsion stiffness	K^R	10×10^5	10×10^4	$\frac{\mathrm{nN}}{\mathrm{m}}$
Repulsion range	R_0^A	0.2	2	μm
Growth count interval	-	1000	†	
Inter-membrane friction	γ_ext	1	10	$\frac{\mu g}{s}$
Medium friction	γ_m	0.4	4	$\frac{\mu g}{s}$
Time step	Δt	1.0×10^{-4}	$*$	
Threshold division volume	V^div	2.9	2900	$\mu\mathrm{m}^3$

Table 4.2: Table shows the Chi-squared values, Eq. 4.19, (degrees of freedom) and p-values (goodness of fit) for the graphs in Fig. 3a, which provides data collapse of the structure factor with MBE scaling exponents for line growth at strong cell-cell adhesion at three different times. The large off diagonal chi-squared values and near-zero off diagonal p-values show that the curves in Fig. 3a at different times do not overlap with each other.

	reference series		
measurement	t = 30	t = 70	t = 200
t = 30	0.0000 (23) p = 1.000	177.93 (24) p = 0.000	487.96 (23) p = 0.000
t = 70	49.780 (22) p = 0.000238	0.000 (23) p = 1.000	79.686 (24) p = 0.000
t = 200	91.66 (22) p = 0.0000	33.599 (22) p = 0.0290	0.000 (23) p = 1.0000

Table 4.3: Table shows the Chi-squared values, Eq. 4.19, (degrees of freedom) and p-value (goodness of fit) for the graphs in Fig. 3b, which provides data collapse of the structure factor with KPZ scaling exponents for line growth at strong cell-cell adhesion at three different times. The low off diagonal chi-squared values and mid-range off diagonal p-values indicate that the curves in Fig. 3b at different times roughly overlap with each other.

	reference series		
measurement	t = 30	t = 70	t = 200
t = 30	0.000 (24) p = 1.000	18.6467 (21) p = 0.4797	23.6806 (21) p = 0.208692
t = 70	18.535 (22) p = 0.5522	0.000 (23) p = 1.000	15.658 (23) p = 0.7885
t = 200	19.066 (19) p = 0.3247	19.066 (22) p = 0.51755	0.0000 (24) P = 1.0000

Table 4.4: Table shows the Chi-squared values, Eq. 4.19, (degrees of freedom) and p-value (goodness of fit) for the graphs in Fig. 3c, which provides data collapse of the width function with MBE scaling exponents for line growth at strong cell-cell adhesion at three different times. The large off diagonal chi-squared values and zero off diagonal p-values show that the curves in Fig. 3c at different times do not overlap with each other.

	reference series		
measurement	t = 30	t = 70	t = 200
t = 30	0.0000 (34) p = 1.000	108.66 (34) p = 0.000	317.38 (33) p = 0.000
t = 70	385.57 (34) p = 0.000	0.000 (34) p = 1.000	193.75 (34) p = 0.000
t = 200	632.77 (32) p = 0.000	139.29 (34) p = 0.000	0.000 (34) p = 1.000

Table 4.5: Table shows the Chi-squared values, Eq. 4.19, (degrees of freedom) and p-value (goodness of fit) for the graphs in Fig. 3d, which provides data collapse of the width function with KPZ scaling exponents for line growth at strong cell-cell adhesion at three different times. The low off diagonal chi-squared values and near-one off diagonal p-values indicate that the curves in Fig. 3d at different times certainly overlap with each other.

	reference series		
measurement	t = 30	t = 70	t = 200
t = 30	0.0000 (34) p = 1.000	26.748 (29) p = 0.477	6.575 (26) p = 0.9998
t = 70	18.98 (33) p = 0.955	0.000 (34) p = 1.000	4.858 (30) p = 1.000
t = 200	16.54 (29) p = 0.942	23.45 (32) p = 0.796	0.000 (34) p = 1.000

Table 4.6: Table shows the Chi-squared values, Eq. 4.19, (degrees of freedom) and p-value (goodness of fit) for the graphs in Fig. 4a, which provides data collapse of the structure factor with MBE scaling exponents for the radially growing interface at weak cell-cell adhesion at three different times. The low off diagonal chi-squared values and mid-range off diagonal p-values indicate that the curves in Fig. 4a at different times roughly overlap with each other.

	reference series		
measurement	t = 40	t = 70	t = 100
t = 40	0.0000 (47) p = 1.000	36.495 (21) p = 0.00917	25.934 (22) p = 0.16801
t = 70	32.8570 (22) p = 0.0350	0.000 (47) p = 1.000	35.994 (22) p = 0.015407
t = 100	20.799 (20) p = 0.28969	23.2245 (20) p = 0.1821	0.000 (47) p = 1.000

Table 4.7: Table shows the Chi-squared values, Eq. 4.19, (degrees of freedom) and p-value (goodness of fit) for the graphs in Fig. 4b, which provides data collapse of the structure factor with KPZ scaling exponents for the radially growing interface at weak cell-cell adhesion at three different times. The large off diagonal chi-squared values and zero off diagonal p-values show that the curves in Fig. 4b at different times do not overlap with each other.

	reference series		
measurement	t = 40	t = 70	t = 100
t = 40	0.0000 (47) p = 1.000	198.89 (25) p = 0.0000	291.566 (25) p = 0.0000
t = 70	644.88 (24) p = 0.0000	0.000 (47) p = 1.000	134.148(26) p = 0.0000
t = 100	1663.32 (23) p = 0.0000	573.74 (24) p = 0.0000	0.000 (47) p = 1.000

Table 4.8: Table shows the Chi-squared values, Eq. 4.19, (degrees of freedom) and p-value (goodness of fit) for the graphs in Fig. 4c, which provides data collapse of the width function with MBE scaling exponents for the radially growing interface at weak cell-cell adhesion at three different times. The low off diagonal chi-squared values and near-one off diagonal p-values indicate that the curves in Fig. 4c at different times certainly overlap with each other.

	reference series		
measurement	t = 40	t = 70	t = 100
t = 40	0.0000 (47) p = 1.000	17.25 (39) p = 0.9977	31.53 (37) p = 0.6364
t = 70	15.46 (40) p = 0.9996	0.000 (47) p = 1.000	31.073 (41) p = 0.8132
t = 100	27.988 (37) p = 0.7940	37.84 (43) p = 0.6118	0.000 (47) p = 1.000

Table 4.9: Table shows the Chi-squared values, Eq. 4.19, (degrees of freedom) and p-value (goodness of fit) for the graphs in Fig. 4d, which provides data collapse of the width function with KPZ scaling exponents for the radially growing interface at weak cell-cell adhesion at three different times. The large off diagonal chi-squared values and zero off diagonal p-values show that the curves in Fig. 4d at different times do not overlap with each other.

	reference series		
measurement	t = 40	t = 70	t = 100
t = 40	0.0000(47) p = 1.000	1203(45) p = 0.000	2044(44) p = 0.000
t = 70	1141(47) p = 0.0000	0.000(47) p = 1.000	664(46) p = 0.000
t = 100	3201(46) p = 0.000	652(47) p = 0.000	0.000(47) p = 1.000

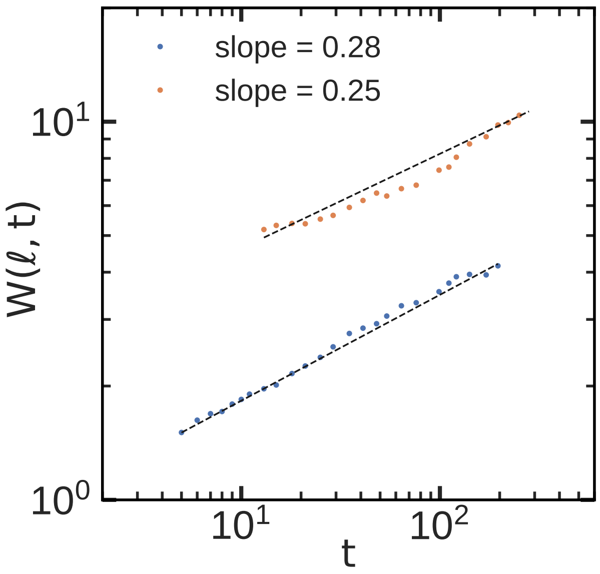

Figure 4.5: Log-log plot of the colony interface width vs growth time of the linear interface for different adhesion strength, 10 (blue) and 2,000 (orange). Growth exponents are $\beta^{\text{weak}} = 0.28 \pm 0.01$ and $\beta^{\text{strong}} = 0.25 \pm 0.02$, respectively. For units, see Table 4.1.

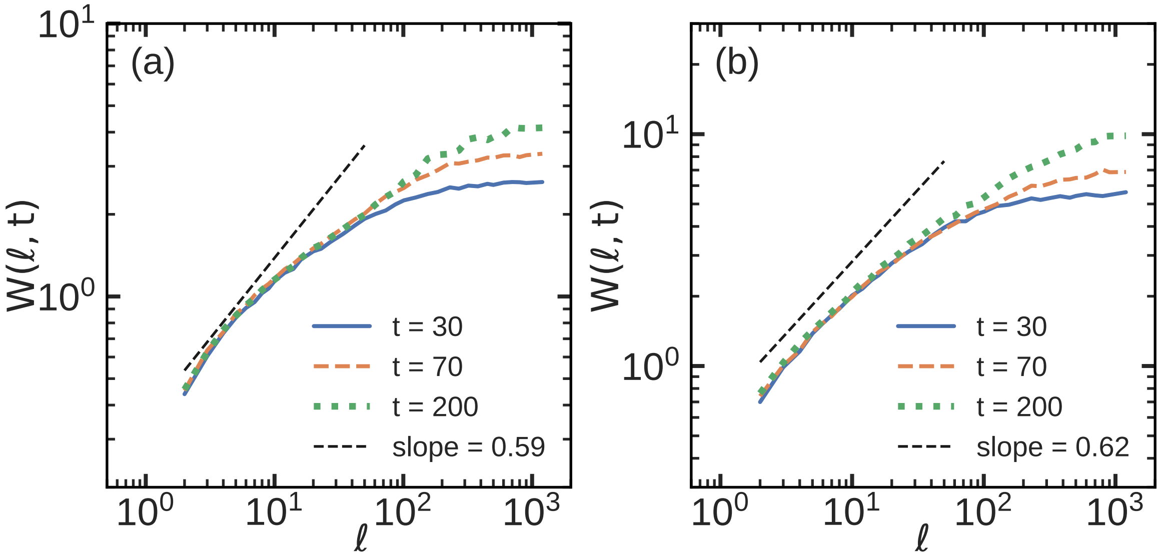

Figure 4.6: Log-log plot of the colony interface width of the linear interface vs length l at three different times. (a) Weak adhesion strength (10) with $\alpha_{\text{loc}}^{\text{weak}} = 0.59 \pm 0.01$ (b) strong adhesion strength (2,000) with $\alpha_{\text{loc}}^{\text{strong}} = 0.62 \pm 0.02$. For units, see Table 4.1.

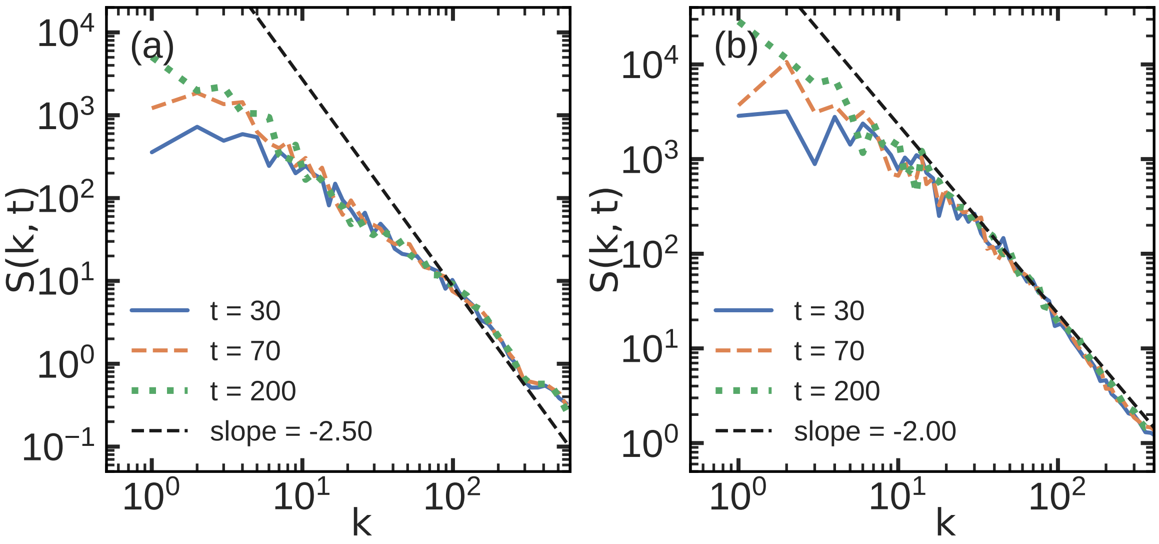

Figure 4.7: Log-Log plot of the structure factor at three different times for linear expanding interface. (a) weak adhesion strength (10) with $\alpha_{\text{glob}}^{\text{weak}} = 0.75 \pm 0.04$. (b) strong adhesion strength (2, 000) with $\alpha_{\text{glob}}^{\text{strong}} = 0.52 \pm 0.02$. For units, see Table 4.1.

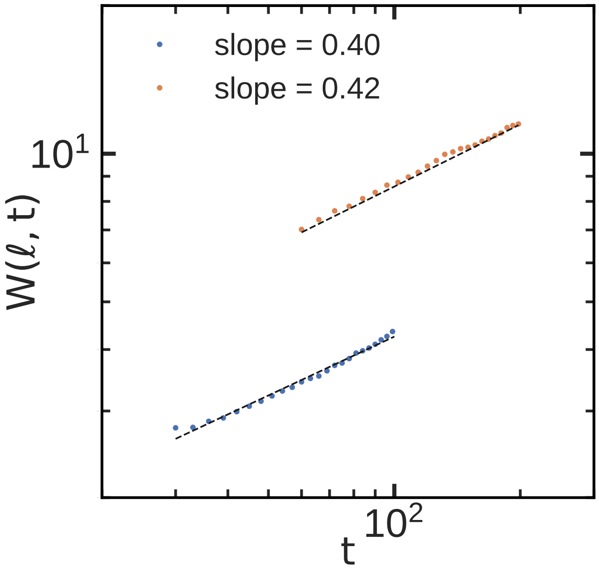

Figure 4.8: Log-log plot of the colony interface width vs growth time of the radially expanding interface for different adhesion strength, 10 (blue) and 2, 000 (orange). Growth exponents are $\beta^{\text{weak}} = 0.40 \pm 0.04$ and $\beta^{\text{strong}} = 0.42 \pm 0.06$, respectively.

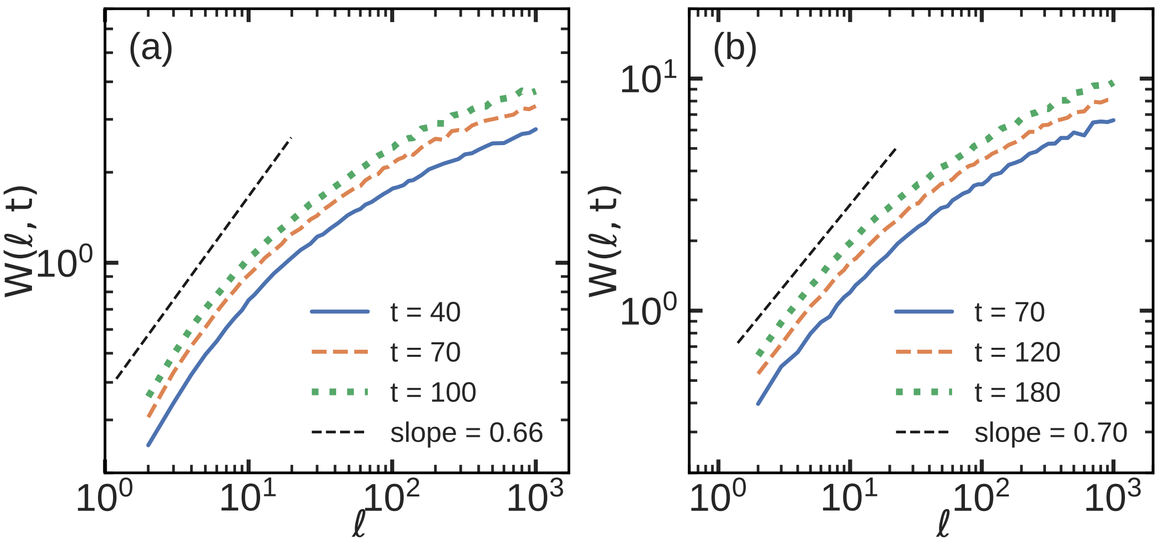

Figure 4.9: Log-log plot of the colony interface width of the radially expanding interface vs length l at different times. (a) Weak adhesion strength (10) with slope $\alpha_{\text{loc}}^{\text{weak}} = 0.66 \pm 0.01$, and (b) strong adhesion strength (2,000) with slope $\alpha_{\text{loc}}^{\text{strong}} = 0.70 \pm 0.01$. For units, see Table 4.1.

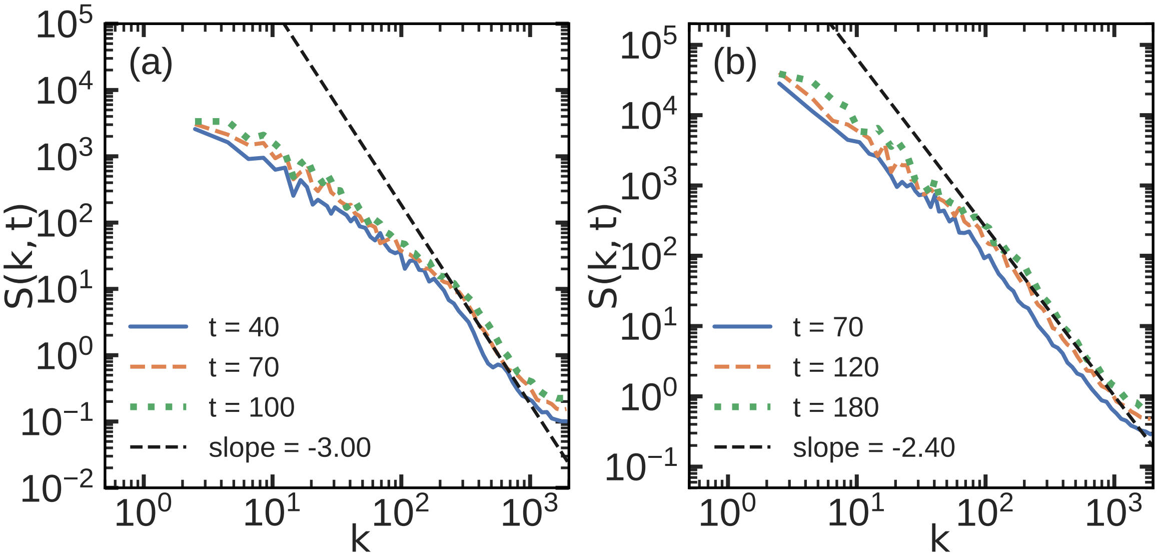

Figure 4.10: Log-log plot of the structure factor at three different times for the radially expanding interface. (a) Weak adhesion strength (10) with $\alpha_{\text{glob}}^{\text{weak}} = 0.95 \pm 0.04$, and (b) strong adhesion strength (2000) with $\alpha_{\text{glob}}^{\text{strong}} = 0.71 \pm 0.02$.

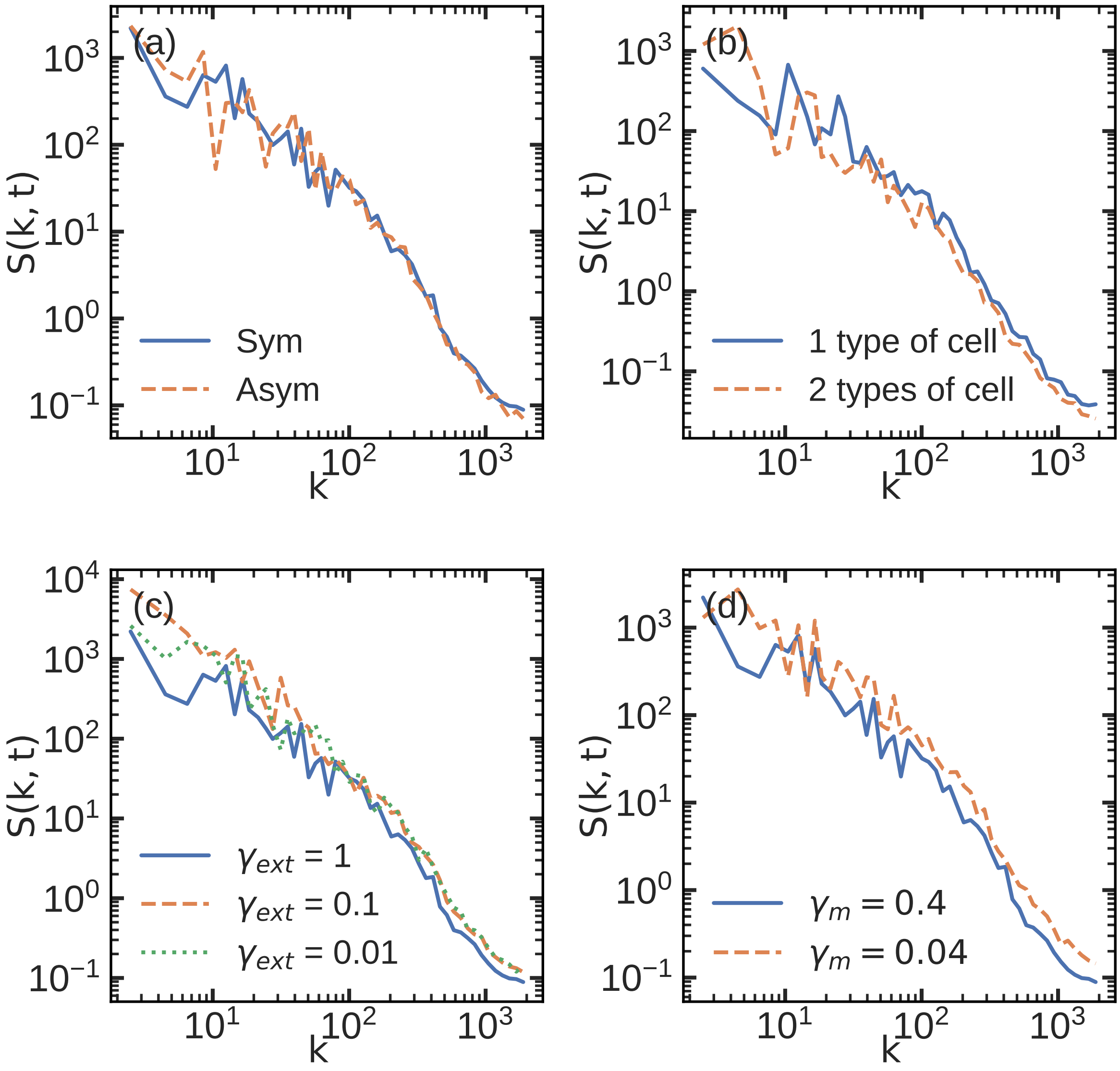

Figure 4.11: Log-Log plot of the structure factor of radially expanding interfaces for (a) The division plane is sampled from a unit circle in the epithelial plane, and can yield two symmetric or asymmetric daughter cells in size. (b) The cell population can contain only one type of cell or two types of cells with different stiffness interacting with each others. (c) different friction coefficients for cell-cell interaction, and (d) different medium friction forces. For units, see Table 4.1.

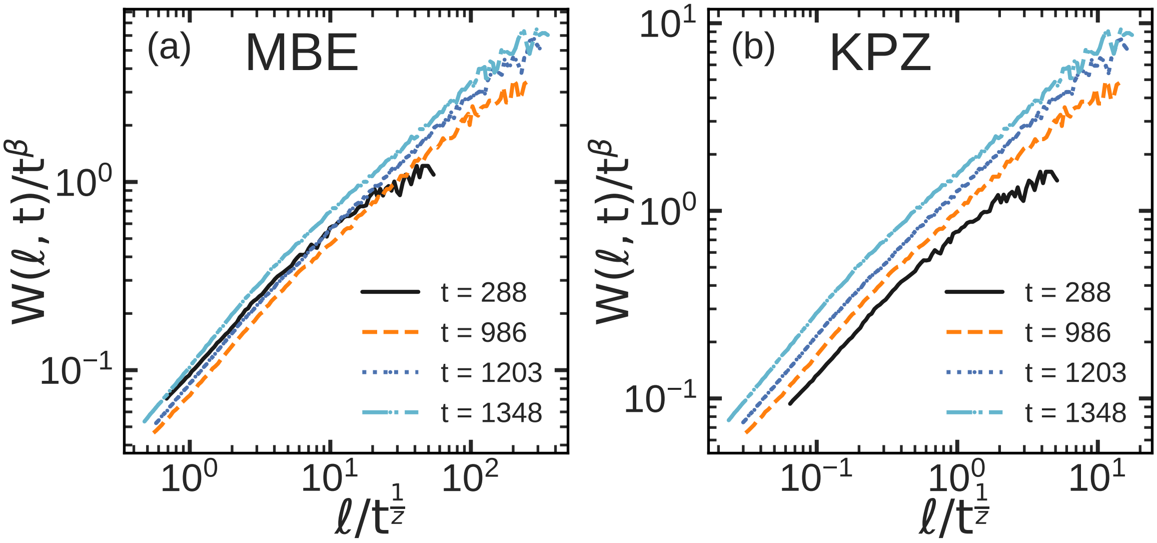

Figure 4.12: (a) Data collapse using Family-Vicsek relation for width functions digitized from Fig. 3 from Brú *et al.* [13], at different times with (a) MBE exponents, $\beta = \frac{3}{8}$ and $z = 4$, and (b) KPZ exponents, $\beta = \frac{1}{3}$ and $z = \frac{3}{2}$.

Chapter 5

Effect of substrate heterogeneity and topology on epithelial tissue growth dynamics

The contents of this chapter have been submitted with the following citation: M. Mazarei, J. Åström, J. Westerholm, and M. Karttunen, *Effect of substrate heterogeneity and topology on epithelial tissue growth dynamics*, Physical Review E, EC12566, 2023, Submitted.

5.1 Introduction

Understanding the role of mechanobiological phenomena in complex biological processes such as wound healing, tumor growth, and morphogenesis necessitates the study of the physical interactions between cells and their environments. *In vivo*, heterogeneities of different types are always present. One of the prime examples is the extracellular matrix (ECM) that typically provides support for cells and is a key factor for cell adhesion and the differentiation of cells [278, 181]. Heterogeneities can also be produced by the addition of pharmacological agents or (gelly) materials, such as methylcellulose, or by changing the nutrient concentration, as well as by other means [83, 279, 253]. The presence of heterogeneities, or disorder in physical terms, often influences biochemical and biomechanical parameters, such as cell-cell interactions, the rate of cell division, and the average cell size and shape, and thus alters cell mobility, colony spreading, and the roughness of the colony interface [83, 279]. In addition, the situation can be even more complex such as in the epithelial-to-mesenchymal and mesenchymal-to-epithelial transitions during which the whole cellular environment undergoes fundamental and complex changes [280].

Tumor growth, and therapy to prevent it, may be characterized as cellular processes involving molecular inter- and intracellular control [84]. Cell migration continually responds to the mechanical stresses from neighboring cells and the ECM [281]. Mathematical and computer models are increasingly being used to examine and measure the influence of different biophysical parameters on biological processes such as nonequilibrium pattern generation in biological growth [257, 282, 283, 246, 279].

The spreading of a cellular colony, e.g., tumor, healthy or bacterial, can be seen as the propagation of an elastic interface in the presence of a pinning potential that arises from the surrounding environment. Analogous phenomena occur in diverse systems including vortex motion in type-II superconductors [284], charge-density waves [285, 286], and fracture propagation [287]. For such systems, one typically distinguishes between strong and weak pinning. In the former case, the pinning energy (per impurity) is much larger than the elastic energy leading to local energy minimization while in the weak pinning regime the opposite is true and the interface adjusts collectively.

When the interface has adjusted to the disorder and is not moving, it is in the pinned phase. When a driving force is applied and it exceeds a threshold force, F_c, the interface undergoes a depinning transition and enters the moving phase. The size of the advancing regions is then characterised by a correlation length (ξ) which diverges upon approaching the critical force from above, $\xi = (F - F_c)^{-\nu}$, where ν denotes the correlation length exponent [288]. It is also common to differentiate between annealed and quenched disorder. In the latter, disorder is considered as stationary, that is, the motions of the pinning sites are much slower than any other relevant time scale in the system; in the annealed case this assumption no longer holds. In this study, only quenched disorder is considered. In addition, since here the driving force enters through cell division, we are not interested in the depinning transition itself.

Several dynamic universality classes have been proposed for interface growth. The Kardar-Parisi-Zhang (KPZ) dynamic universality class [249] describes the evolution of a surface using a continuous nonlinear stochastic differential equation

$$\partial_t h(x,t) = -\lambda\,[\partial_x h(x,t)]^2 + \nu\partial_x^2 h(x,t) + \eta(x,t), \tag{5.1}$$

where $h(x,t)$, or the height, is the distance from the ith point at the colony front to the baseline of the colony. Lateral growth normal to the interface, reflected in the quadratic term $-\lambda(\partial_x h)^2$, is a characteristic of the KPZ universality class. Surface tension is accounted for by the Laplacian term, $\nu\partial_x^2 h$, which tends to flatten the surface, and $\eta(x,t)$ is an uncorrelated Gaussian noise given by $\langle\eta(x,t)\rangle = 0$ and $\langle\eta(x,t)\eta(x',t')\rangle = 2D\delta(x-x')\delta(t-t')$.

In the quenched KPZ (qKPZ) equation the thermal noise in Eq. 5.1 is replaced by a position dependent noise, that is, $\eta(x,t)$ becomes $\eta(x,h)$ with $\langle\eta(x,h)\rangle = 0$ and $\langle\eta(x,h)\eta(x',h')\rangle = 2D\delta(x-x')\delta(h-h')$. Since thermal noise is usually present in experiments, the qKPZ equation can be extended to contain both quenched and thermal noise.

Dynamic scaling analysis provides powerful tools to classify growth. Dynamic critical exponents, namely the roughness (α), growth (β), and the dynamic exponent (z) can be determined from the time evolution of the front's roughness; the cell colony's front in this case [245, 246, 247, 76, 13, 87, 248, 88, 89]. In addition to the above, the dynamic exponent is related to the two other exponents via $z = \frac{\alpha}{\beta}$.

Distinct critical exponents and universality classes are described by different growth equations. For KPZ, the critical exponents are $\alpha^{\mathrm{KPZ}} = \frac{1}{2}$, $\beta^{\mathrm{KPZ}} = \frac{1}{3}$, and $z^{\mathrm{KPZ}} = \frac{3}{2}$ for one dimensional interfaces [5]. For the quenched KPZ equation, dynamic critical exponents haven been determined to be $\alpha^{\mathrm{qKPZ}} = \frac{3}{4}$, $\beta^{\mathrm{qKPZ}} = \frac{3}{5}$, and $z^{\mathrm{qKPZ}} = \frac{5}{4}$ [289]. The critical exponents of the linear molecular beam epitaxy (MBE) equation for a one-dimensional interface are $\alpha^{\mathrm{MBE}} = \frac{3}{2}$, $\beta^{\mathrm{MBE}} = \frac{3}{8}$, and $z^{\mathrm{MBE}} = 4.0$.

In one-dimensional quasilinear and quasicircular expanding interfaces, previous experimental research on cells grown on culture without quenched disorder have presented various scaling behaviors [87, 13, 88, 89, 4]. Brú *et al.* [13, 87] suggested that the development dynamics of both malignant and normal cell colonies are characterized exponents $\alpha = 1.5 \pm 0.15$, $\beta = 0.38 \pm 0.07$, and $z = 4 \pm 0.5$ that belong to the MBE universality class. They reported this for both *in vitro* and *in vivo* experiments. In contrast, however, Huergo *et al.* reported the exponents of $\alpha = 0.50 \pm 0.05$, $\beta = 0.32 \pm 0.04$ and $z = 1.56 \pm 0.1$ for interfacial growth of HeLa (cervix cancer) cell colonies *in vitro* [88, 89, 4]. Plant calli, *Brassica oleracea* and *Brassica rapa*, were studied by Galeano *et al.* who reported exponents inconsistent with both MBE and KPZ, $\alpha = 0.86 \pm 0.04$, and $z = 5.0$ [253].

Biological systems with substrate disorder appear in situations such as growing bacterial colonies on agar-containing media and in the development of bacterial biofilms. For *Escherichia coli* and *Bacillus subtilis* colonies, Vicsek *et al.* [82] found the roughness exponent $\alpha = 0.78 \pm 0.07$, which exceeds the KPZ value. Huergo *et al.* reported qKPZ-compatible exponents $\alpha = 0.63 \pm 0.04$, $\beta = 0.75 \pm 0.05$, and $z = 0.84 \pm 0.05$ for the development of quasilinear Vero cell colony fronts in culture media containing methylcellulose (MC) [83]. Santalla *et al.* conducted experiments at a high agar concentration regime and found branching interfaces whose scaling exponents were in complete disagreement with both the KPZ and qKPZ scaling exponents [254]. Rapin *et al.* studied the effects of pharmacological agents on the geometry and roughness dynamics of *in vitro* propagating Rat1 fibroblast cell interfaces and reported two separate scaling regimes, the first at the sub-cell level and the second at intermediate length scales of 2-10 cells [279].

Various theoretical and computational models have been developed to examine surface growth with quenched disorder. The directed percolation depinning model predicts α to be between 0.66 and 0.73, and $\beta = 0.68 \pm 0.04$ [290]. Models of self-organized growth have predicted $\beta = 0.9 \pm 0.1$ and $\alpha = 0.63 \pm 0.02$ [291], and a numerical study of an automaton model yielded $\alpha = 0.63 \pm 0.01$ and $\beta = 0.64 \pm 0.02$ [292]. Santalla and Ferreira incorporated nutrient diffusion to an off-lattice Eden model and reported a transition from a transient KPZ-like regime with $\beta = 0.34 \pm 0.01$ to an unstable growth regime with $\beta = 0.43 \pm 0.02$, with an intermediate transient regime belonging to the qKPZ universality class with $\beta = 0.633$ and the local roughness exponents ranging within $0.39 < \alpha_{\mathrm{loc}} < 0.67$ [92].

Further computational and theoretical studies have demonstrated the effects of cell-cell mechanical tensions, and nutrient concentration and distribution on the spatial structures with morphologies ranging from smooth to heavily fingered interfaces [293, 294]. Simulations of two-dimensional cellular colonies by Block *et al.*, showed KPZ-like dynamics for a class of cellular automata models over a broad range of parameters [77]. Azimzade *et al.* used the Fisher-Kolmogorov-Petrovsky-Piskunov (FKPP) equation to study the effect of the cellular environment's stiffness and spatial correlations on the morphology of the interface of growing tumors, and concluded that the KPZ equation cannot describe their tumor development model [91]. Bonachela *et al.* developed an off-lattice cell model with quenched disorder describing competition among bacterial cells for space and resources. They reported the exponents $\alpha = 0.68 \pm 0.05$, $\beta = 0.61 \pm 0.05$, and $z = 1.11 \pm 17$ for the moving regime [256]. Pinto *et al.* modified the self-propelled Voronoi model of Bi *et al.* [295] to study the effect of spatial disorder of the cell-substrate interaction, defined as having stiff cells in the tissue, on cell motility in a confluent tissue, reporting $\beta = 0.194. \pm 007$ [296]. In our previous work, we showed that a cell colony can show both KPZ- and MBE-like scaling dynamics depending on the strength of the cell-cell adhesion between the cells and the cell colony's geometry [14].

5.2 Methods

5.2.1 CELLSIM3D SIMULATOR AND MODEL

CELLSIM3D is a coarse-grained molecular dynamicsbased model of cellular dynamics with an emphasis on mechanobiological features of tissue growth [10]. The code is open source [297]. CELLSIM3D allows cellular growth to be modelled in two (epithelial growth) or three dimensions, and cells are modelled as three-dimensional objects consisting of a set of interconnected nodes. Here, the geometry and the nodes are those of a spherical C180 fullerene.

The CELLSIM3D force field consists of intra- and intercellular forces and a noise term (η),

$$m\mathbf{r} = \mathbf{F}^{\mathrm{B}} + \mathbf{F}^{\theta} + \mathbf{F}^{\mathrm{R}} + \mathbf{F}^{\mathrm{A}} + \mathbf{F}^{\mathrm{F,e}} + \mathbf{F}^{\mathrm{F,m}} + \mathbf{F}^{\mathrm{P}} + \eta. \tag{5.2}$$

The two intracellular forces on the surfaces of the cells are $\mathbf{F}^{\mathrm{B}}$, a damped harmonic oscillator force between the nearest neighboring nodes with a spring constant (k^{B}) and a friction coefficient (γ_{int}), and $\mathbf{F}^{\theta}$, the angle force which is a harmonic potential depending on the equilibrium angles between the nodes with a spring constant k^{θ}). The angle term preserves the cell's surface curvature. For simplicity, the spring constants for both the angle force and the damped spring force between the nodes are assumed to be constant over the cell surface.

Intercellular forces in CELLSIM3D consist of both cell-cell and cell-environment interactions. In cells, the cell-cell interactions are mainly caused by cell adhesion molecules (CAMs) [47, 269, 193]. Here, the intercellular forces are described by a repulsive force, $\mathbf{F}^{\mathrm{R}}$ and an attractive force, $\mathbf{F}^{\mathrm{A}}$, between two neighboring cells. In addition, the model also includes a friction force, $\mathbf{F}^{\mathrm{F}}$, between two cells that pass by each other. The repulsive and attractive forces between the cells are represented, respectively, by short-range harmonic potentials with distinct cutoffs R_0^{R}, R_0^{A}, and spring constants k^{A}, k^{R}. In this study, we assume that the adhesion molecules are distributed uniformly across the cell surface, and that the adhesion and repulsion spring constants (k^{A}, k^{R}) are identical for all nodes on the surface. The intermembrane friction force, $\mathbf{F}^{\mathrm{F,e}} = -\gamma_{\mathrm{ext}}\, \mathbf{v}_{ij}^{\tau_{\mathrm{m}}}$, is defined up to a cutoff range, R_0^{A}, between the nodes i and j on two separate cells as a function of the tangential relative velocity to the cell surfaces, $\mathbf{v}_{ij}^{\tau_{\mathrm{m}}}$. The intermembrane friction coefficient, γ_{ext}, is assumed to be constant across the cells.

The friction force, $\mathbf{F}^{\mathrm{F,m}} = -\gamma_{\mathrm{m}}\, \mathbf{v}$, approximates the interactions between the cell and its environment, and it is defined as a viscous drag force from a fluid medium. The growth force, $\mathbf{F}^{\mathrm{P}} = PS\hat{\mathbf{n}}$, is determined by the cell's internal pressure resulting from the osmotic pressure within the cell [47], where $\hat{\mathbf{n}}$ is an outward pointing normal to the surface of the cell and PS is the force due to a growing pressure inside the cell. This growing force compensates for the cell membrane elasticity modelled by harmonic potentials. Finally the noise term, η, is defined as a Gaussian white noise with $\langle \eta(x,t) \rangle = 0$ and $\langle \eta(x,t)\eta(x',t') \rangle = 2D\delta(t-t')\delta(x-x')$.

At each time step, the internal pressure increases by the growth rate $\mathit{\Delta}(PS)$, resulting in a gradual increase in the pressure force ($\mathbf{F}^{\mathrm{P}}$) and the cell volume. When the volume of the cell reaches a critical threshold, given by the parameter V_{div}, the cell divides into two daughter cells. The distinguishing characteristics of the cell division are the orientation and the location of the division plane. Cell division can be either symmetric or asymmetric, depending on the position of the division plan. In this study, we used symmetric cell division, in which the volumes of the daughter cells become half the volume of the parent cell, and the mechanical properties are a copy of the parent cell's properties. The division algorithm is accounts for the planar expansion of epithelial tissue: The division plane is selected by randomly sampling a vector from a circle in the plane defined by the vector normal to the epithelial plane. To prevent buckling during growth, three-dimensional cells are confined between two frictionless plates with repulsion in the direction normal to the plates [258, 14]. More details of the theoretical basis, the code implementation, and the mapping of the parameters can be found in Refs. [10, 14, 258]. Parameters for the simulations performed in this study are provided in Table 5.1.

Table 5.1: The parameters for the cells used in this study. These values are based on the HeLa (named after Henrietta Lacks [16]) cell properties. † indicates units of Δt and $*$ units of mean time to cell division, which varies between cell types and is set to 1.0 in CellSim3D.

Parameter	Notation	Sim. Units	SI Units	
Nodes per cell	N_c	180	-	
Node mass	m	0.04	40	fg
Bond stiffness	k^{B}	1000	100	nN/μm
Bond damping coefficient	γ_{int}	100	0.01	g/s
Minimum pressure	$(PS)_0$	50	0.5	nN/μm^2
Maximum pressure	$(PS)_\infty$	65	0.65	nN/μm^2
Pressure growth rate	$\Delta(PS)$	0.002	2.0×10^{-5}	nN/μm^2
Attraction stiffness	K^{A}	10-2000	1-200	nN/μm
Strong attraction stiffness	$K^{\mathrm{A}}_{\mathrm{strong}}$	2000	200	nN/μm
Weak attraction stiffness	$K^{\mathrm{A}}_{\mathrm{weak}}$	10	1	nN/μm
Attraction range	R^{A}_0	0.3	3	μm
Repulsion stiffness	K^{R}	10×10^5	10×10^4	nN/m
Repulsion range	R^{A}_0	0.2	2	μm
Growth count interval	-	1000	†	
Inter-membrane friction	γ_{ext}	1	10	μg$/s$
Medium friction	γ_{m}	0.4	4	μg$/s$
Time step	Δt	1.0×10^{-4}	$*$	
Threshold division volume	V^{div}	2.9	2900	μm^3

5.2.2 Disorder

Pinning impurities were randomly positioned (at time $t = 0$) as immobile cells that do not grow. They interact with regular cells via adhesion, repulsion, and friction, with the same strengths as the regular cells do. Importantly, when the adhesion interaction between the cells is strong, so is the interaction between the cells and the disorder. The same applies for the case of weak cell-cell interaction. The pinned cells maintain their spherical shapes and sizes throughout the simulation. For each simulated parameter set, ten independent simulations were performed for data averaging. The parameters for quenched disorder are shown in Table 5.2.

Table 5.2: The area density, $\frac{N}{A}$, for quenched disorder in SI units ($\frac{1}{\mu\text{m}^2}$) in the different configurations (linear and radial), and at different attraction stiffnesses ($\frac{\text{nN}}{\mu\text{m}}$). The parameters for the strong and weak cases are given in Table 5.1.

Attraction stiffness Configuration	1 (weak)	200 (strong)
Moving linear interface	0.0010	0.0003
Moving linear interface at high disorder density	0.0012	-
Moving radial interface	0.0008	0.000075
Pinned radial interface	0.0012	-

5.2.3 Colony configurations

Simulations of both linear and radial growth at strong and weak cell-cell adhesion strengths in the presence of quenched disorder were performed at both low and high disorder densities, see Table 5.1 for parameters and Table 5.2 for disorder area densities. The initial configuration of the linear interface was a line of 240 cells in a box of size $600 \times 1,000 \times 1.8$. For linear interfaces in the low disorder density regime at weak and strong cell-cell adhesion, 60,000 and 18,000 immobile cells were initially distributed at random in the box, while in the high disorder density regime at weak cell-cell adhesion, 72,000 immobile cells were randomly distributed in the box, see Table 5.2 for disorder area density. Figure 5.1 shows time evolution of a linear interface.

For radial growth, the initial configuration consisted of a single cell at the center of the box of size $800 \times 800 \times 1.8$. In the low disorder density regime at weak and strong cell-cell adhesion strengths, respectively, $51,200$ and $4,800$ immobile cells were initially distributed at random in the box. In the case of high disorder density at weak cell-cell adhesion strength, the box contained $77,400$ randomly distributed immobile cells, see Table 5.2. In the low disorder density regime, the colonies maintained their circular morphology with interface overhangs. In high disorder density regime, however, the cell colonies developed a chiral morphology with branched structures lacking circular interfaces for scaling analysis. Snapshots of circular colony expansion, interface evolution and chiral colony morphology at different times are shown in Fig. 5.2.

5.3 Analyses

5.3.1 Scaling analysis

Interface width

The standard deviation of the front height across a length scale l at time t can be used to define the interface's local width function, $w(l,t)$, which represents the fluctuation around the average height of the interface [6] as

$$w(l,t) = \left\{ \frac{1}{N} \sum_{i=1}^{N} [h_i(t) - \langle h_i \rangle_l]^2 \right\}_L^{\frac{1}{2}}, \tag{5.3}$$

where L is the the length of the growing front. For radial growth, the height, $h_i(t)$, is replaced by the distance $r_i(t)$ from the centre of mass of the cell colony. $\langle h_i \rangle_l$ is the local average of the subsets of arc length l, and $\{.\}_L$ is the overall average. The fluctuations cannot increase indefinitely, and there exists a saturation time, t_s.

For times greater than the saturation time $t \gg t_s$, when the local length l equals the total interface length L, the width function $w(L,t)$ represents the interface variance and increases

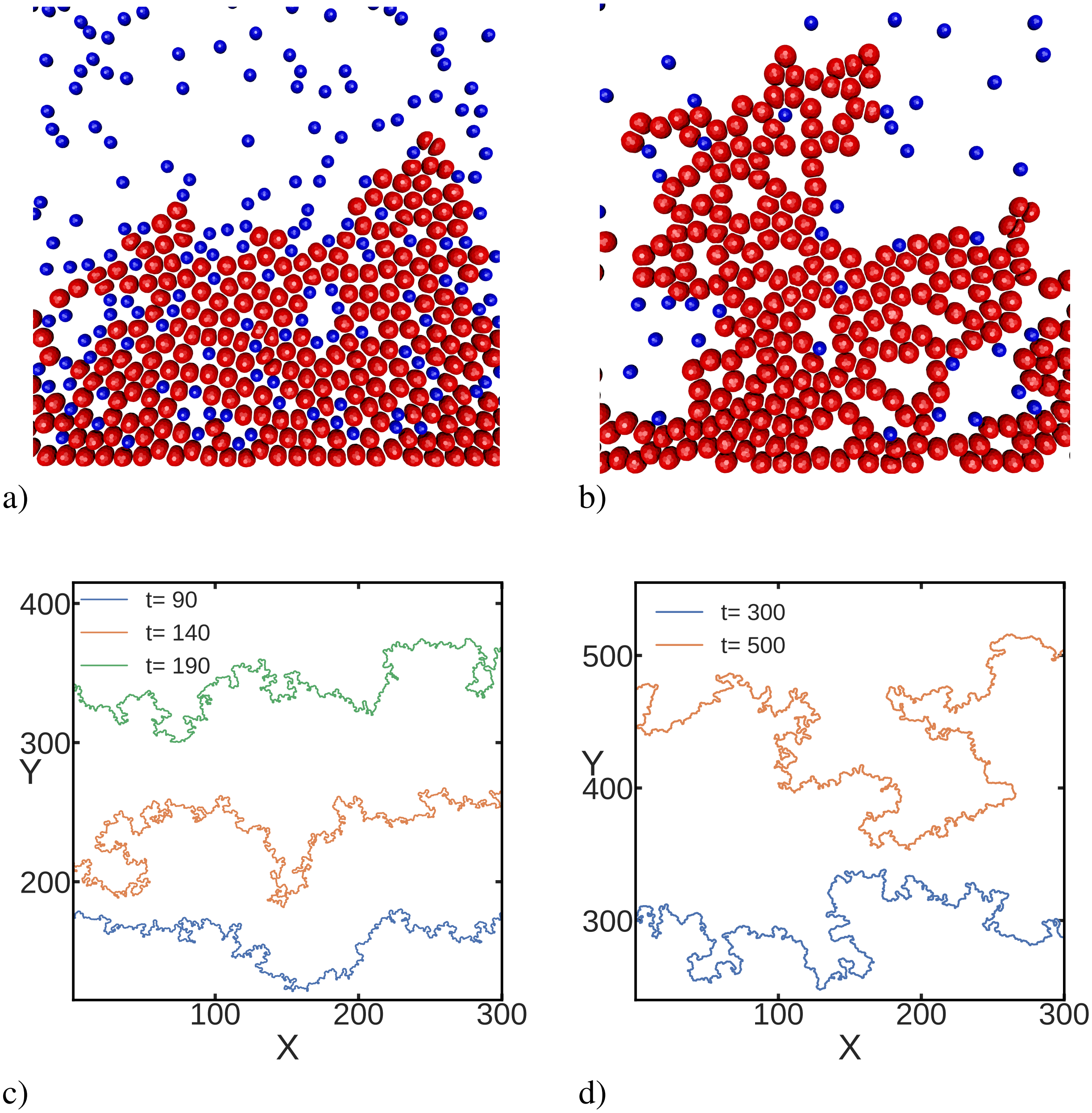

Figure 5.1: (a-b) Colony expansion (red cells) in a medium with quenched disorder (blue cells) with linear initial configuration. (a) At weak and (b) strong cell-cell adhesion strength. (c) Interface evolution at different times (d) at weak and (lower right) strong cell-cell adhesion strength. The scaling analysis was done using overhang-corrected interfaces [6]. For units, see Table 5.1.

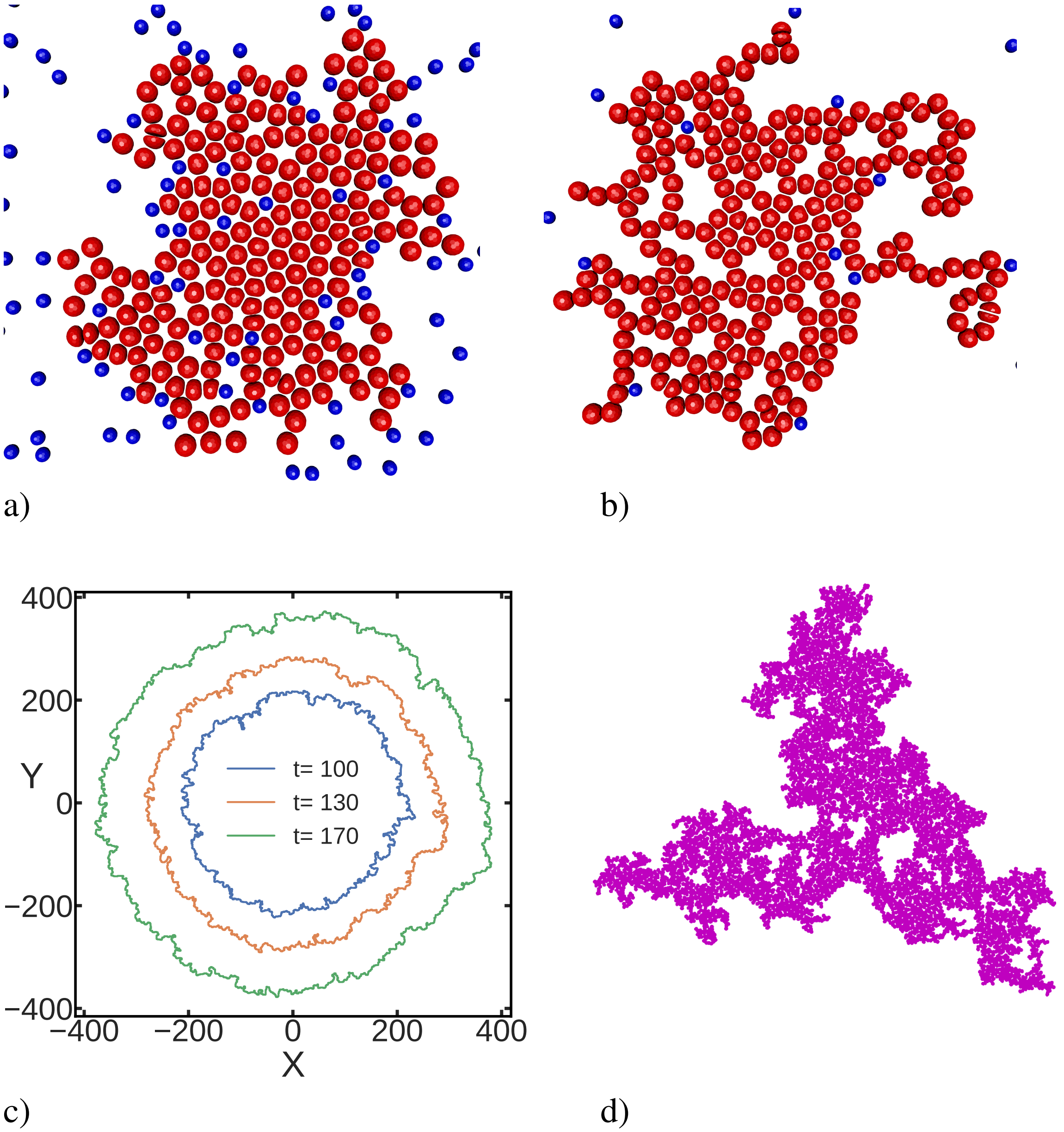

a)

b)

c)

d)

Figure 5.2: (a,b) Radially growing colony (red cells) in a medium with quenched disorder (blue cells). (a) At weak and (b) strong cell-cell adhesion strength. (c) Interface evolution at different times at weak cell-cell adhesion strength. The interface has overhangs, but the scaling analysis was done using overhang-corrected interfaces [6]. (d) Morphology for a system started with a single cell at the centre of a box on a substrate with a high density of quenched disorder at weak cell-cell adhesion strength. Due to the high disorder density, the morphology is not round but instead chiral with branched structures. Eventually the interface becomes pinned by the disorder and the growth stops. The final population of the cell colony consists of roughly 10,000 cells. For units, see Table 5.1.

with the interface length L according to $w(L,t) \sim L^{\alpha}$, where α is to referred as the global roughness exponent. For times smaller than the saturation time, the interface variance increases as $w(L,t) \sim t^{\beta}$, where β is the growth exponent.

For self-affine interfaces the width function $w(L,t)$ satisfies the Family-Vicsek dynamic scaling relation [117]. This scale invariant behavior implies that the total interface length, L, is the only characteristic length scale in the system, and that all length scales are subject to the same physics. However, for $t > t_{\rm s}$ the local width function $w(l,t)$ may increase as a function of the local length, l, with a local roughness exponent [6] $\alpha_{\rm loc}$ as

$$w(l,t) \sim l^{\alpha_{\rm loc}}. \tag{5.4}$$

The local roughness exponent may differ from the global roughness exponent and can also be derived from the power law behavior of the height-height correlation function, which is defined as

$$C(\ell,t) = \langle |h(x,t) - h(x+\ell,t)|^2 \rangle_{\rm x} \sim \ell^{2\zeta} \text{ for } \ell \ll \xi_{||}, \tag{5.5}$$

where $\xi_{||}$ is the parallel correlation length of the interface, and ℓ is the lateral distance between different points on the interface. The the height-height correlation function obeys the scaling ansatz [6]

$$C(\ell,t) \sim \ell^{2\zeta} c(\ell/t^{1/z^{\rm c}}), \tag{5.6}$$

where $c(x)$ is constant for $x \ll 1$ and $c(x) \sim x^{-2\zeta}$, for $x \gg 1$. In growth models with anomalous behavior, the global roughness (α) and dynamic exponents (z) calculated from the interface width function differ from ζ and $z^{\rm c}$ calculated from the height-height correlation function [298, 251]. In these models, the scaling function $c(x)$ can be different from constant for $x \ll 1$, and the scaling relation for the height-height correlation function becomes [298, 115]

$$C(\ell,t) \sim C(1,t)\ell^{2\zeta} c(\ell/\xi(t)), \tag{5.7}$$

where $\xi(t) = [t/C(1,t)]^{1/z^c}$. The average step height, $C(1,t)$, grows as

$$C(1,t) \sim t^{2\lambda}. \tag{5.8}$$

This modified scaling ansatz, Eq. 5.7, implies $\alpha = \zeta + \lambda z/2(1-\lambda)$ and $z = z^c/(1-\lambda)$ [115]. For $t \ll t_s$ the value of the local width function $w(l,t)$ increases with time with the growth exponent β as

$$w(l,t) \sim t^{\beta} \text{ for } t \ll t_s. \tag{5.9}$$

Structure factor

The above real-space analysis takes into account all wavelengths, including short ones, which indicates that finite-size effects can be expected. As a solution, the power-law behavior of the power spectrum of the height fluctuations where only long-wavelength modes contribute to the scaling behavior should be analyzed. To calculate the structure factor, $S(k,t) = \langle \hat{h}(k,t)\hat{h}(-k,t)\rangle$, the kth Fourier mode $\hat{h}(k,t)$ needs to be evaluated.

The Family-Vicsek scaling form of the structure factor can be then given as

$$S(k,t) = k^{-(2\alpha+1)} s(kt^{\frac{1}{z}}), \text{ where} \tag{5.10}$$

$$s(u = kt^{\frac{1}{z}}) = \begin{cases} \text{const} & \text{for } u \gg 1; \\ u^{2\alpha+1} & \text{for } u \ll 1. \end{cases} \tag{5.11}$$

Here, α is the global roughness exponent and $s(u = kt^{\frac{1}{z}})$ the scaling function. Systems with different local and global roughness exponents represent what is known as anomalous roughening [299]. This phenomenon has been observed in various growth models [300, 301, 302] and experiments [303, 304, 87]. Two known types of anomalous roughening are intrinsic anomalous roughening, where $\alpha_{\text{loc}} < 1$ and $\alpha > \alpha_{\text{loc}}$, and superroughening, where $\alpha > 1$ and

$\alpha_{\mathrm{loc}} = 1$ [305, 299]. In such systems the scaling function, $s(u)$, has the general form

$$s(u = kt^{\frac{1}{z}}) = \begin{cases} u^{2(\alpha-\alpha_{\mathrm{s}})} & \text{for } u \gg 1; \\ u^{2\alpha+1} & \text{for } u \ll 1, \end{cases} \tag{5.12}$$

where the spectral roughness exponent, α_{s}, is independent from the global roughness exponent. In system with intrinsic anomalous roughening, $\alpha_{\mathrm{s}} = \alpha_{\mathrm{loc}} < 1$, and α_{s} is different from global roughness exponent, α.

5.3.2 Chi-squared minimization

Chi-squared minimization was used to determine the slope and the y-intercept of the line that best fits the data. As every data point in our case was measured ten times, there is a standard error σ_i that can be associated with individual points in the graphs at different times or lengths. The model's prediction is a lin-lin or log-log straight line $f(x) = b + a\,x$ with parameters a and b. The Chi-squared function is calculated by summing the squares of the differences between the model's prediction and the observed data y_i, then dividing by the data's variance. It is defined as

$$\tilde{\chi}^2 = \sum_{i=1}^{N_{\mathrm{d}}} \frac{(y_i - f(x_i; a, b))^2}{\sigma_i^2}, \tag{5.13}$$

where N_{d} is the total number of data points. The optimal values for the model parameters a and b are obtained by minimization of the chi-squared function. Goodness of fit, the p-values, are calculated from the chi-squared probability function $Q(\chi^2|N_{\mathrm{d}} - 2)$ corresponding to the probability of accepting the null hypothesis of obtaining the same model parameters if the experiment was performed numerous times with identical setup. A p-value near unity indicates that the fit is good, whereas a small p-value indicates that the fit is poor.

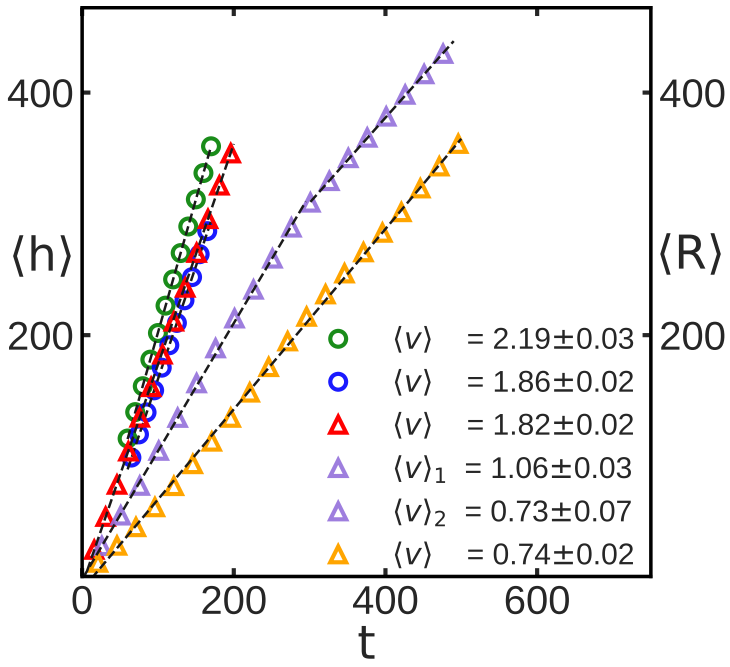

Figure 5.3: Interface velocity calculated from the time evolution of the mean colony radius ($\langle R \rangle$) and the mean interface height ($\langle h \rangle$) for radially (circles) and linearly (triangles) expanding interfaces, respectively. For units, see Table 5.1.

5.4 Results

Interface velocity

For both linear and radial colonies at low disorder densities, the interfaces move at a constant velocity and do not become pinned by disorder, Figure 5.3.

In the case of linear interface at weak cell-cell adhesion strength, the interface moves at the velocity of $\langle v \rangle = 1.82 \pm 0.02$. At strong cell-cell adhesion strength the velocity drops to $\langle v \rangle = 0.74 \pm 0.02$.

In radial interface growth, the velocities are higher, $\langle v \rangle = 2.19 \pm 0.03$ at weak cell-cell adhesion strength, and $\langle v \rangle = 1.86 \pm 0.02$ in the case of strong adhesion strength.

Two cases deserves special attention: First, in linear growth with weak cell-cell adhesion and high disorder density, the growth slows down and there is a crossover from $\langle v \rangle_1 = 1.06 \pm 0.03$ at short times to $\langle v \rangle_2 = 0.73 \pm 0.07$ at late times. Second, in the case of weak adhesion strength and high disorder density in circular expansion, the colonies develop a chiral morphology in which the branches proliferate and get pinned over time, preventing the definition of a circular interface and the evaluation of its velocity.

Fractal dimension

The fractal dimensions of interfaces were evaluated using the box-counting method, Fig. 5.4. As a general trend, the fractal dimensions of the linear interfaces are slightly larger compared to the circular ones. In addition, the fractal dimensions here are slightly higher than those in the absence of quenched disorder [14]. Table 5.3 lists the fractal dimensions in the current study, and several past experiments and simulations under different conditions.

The one outlier regarding the fractal dimension is the system that develops chiral morphology, that is, the circularly growing system with high disorder density. The result is $d_{\mathrm{f}} = 1.74 \pm 0.06$. This value is within the margin of error to computer simulations of the diffusion limited aggregation (DLA) fractal model with $d_{\mathrm{f}}^{\mathrm{DLA}} = 1.71$ [306, 307]. This chiral morphology has no well-defined interface but rather a branched structure, and it has been observed, for example, in bacterial growth on agar plates with a low nutrient concentration [308, 309, 310].

Roughness exponents for linear interfaces

The interface roughness, $w(l, t)$, was evaluated from Eq. 5.9. For linear interface growth with quenched disorder, increasing the cell-cell adhesion strength or the disorder density resulted in higher growth exponents (β) than in the absence of disorder, see Ref. [14] and Table 5.3. The local roughness exponents, α_{loc}, were obtained from Eq. 5.4. The exponents have the same value at weak adhesion strength both low and high disorder density. At strong adhesion strength and low disorder density, α_{loc} increases slightly, Table 5.3. These local roughness exponents are also less than what has been obtained from simulations without quenched disorder, see Ref. [14] and Table 5.3.

The global roughness exponents (α) were calculated via structure factor analysis, Eq. 5.11.

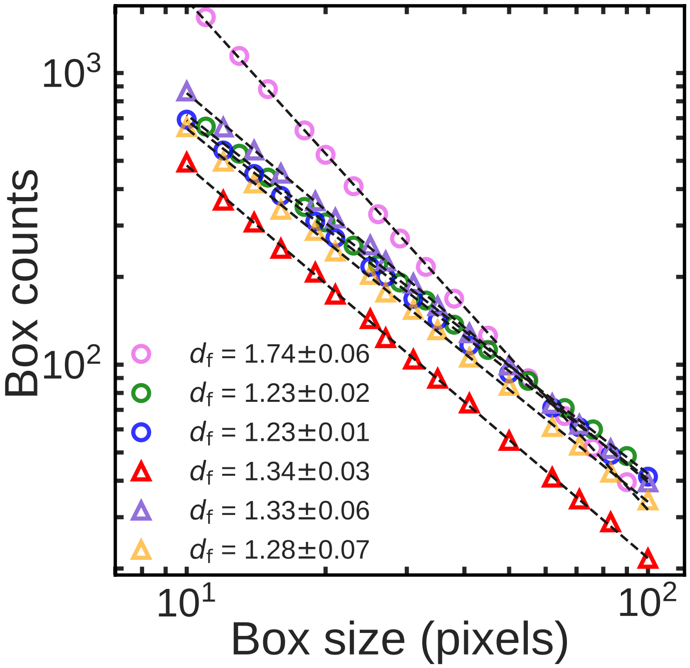

Figure 5.4: Fractal dimension (d_f) determined by plotting box counts vs. box size for the linear interface (triangles) 1) at weak (red triangles) and 2) at strong (orange triangles) adhesion strength, and 3) at weak cell-cell adhesion in high disorder density (purple triangle). For the radially expanding interface (circles) 1) at weak (green circles) and 2) strong (blue circles) cell-cell adhesion, and high disorder density (violet circles). The colony fractal dimension, (d_f^{col}), for colony expansion at weak cell-cell adhesion began with a single cell in the centre of a box on a substrate with a high density of quenched disorder. This system does not have a dense and round morphology, instead it forms slowly to a chiral morphology with branched structure until the colony interface becomes pinned with the disorder on the substrate. The colony fractal dimension is very close to the DLA fractal model, $d_f = 1.71$.

The results are shown in Fig. 5.5. As in the case of α_{loc}, the global roughness exponents have lower values than those from simulations without quenched disorder [14], see Table 5.3. The values are in the same range and independent of the adhesion strength and disorder concentration, whereas for linear colony growth in media without quenched disorder [14], the value of the global roughness exponent depends on the adhesion strength, see Table 5.3.

Figure 5.6 shows the correlation exponent (ζ) defined via Eq. 5.5. Interestingly, the exponent is the same in all cases for linear growth, independent of the disorder density or cell-cell adhesion, Table 5.3. The scaling regime, however, increases as cell-cell adhesion increases.

The correlation exponent was also determined in the absence of disorder based on the data from Ref. [14]. In that case, the correlation function shows a crossover between two exponents both at weak and strong cell-cell adhesion, Table 5.3. For shorter scales, the exponents are within the margin error to the value $\zeta^{\mathrm{weak}} = 0.53$ obtained in the presence of disorder. For longer scales, the exponent crosses over to about $\zeta \approx 0.32$.

The scaling exponents of linear interface growth at low disorder density at weak adhesion strengths are compatible with KPZ scaling exponents, whereas the global roughness exponent of linear interface growth at weak adhesion strengths in media without quenched disorder is greater than the KPZ global roughness exponent, see Table 5.3.

Roughness exponents for radial growth

Next, we determine the scaling exponents for radially expanding interfaces. As with linear interfaces, the presence of disorder leads to higher growth exponents (β) compared to the cases in the absence of disorder, Table 5.3. Similarly to linear colony growth, the local roughness exponents (α_{loc}) are in the same range, but somewhat smaller than without disorder [14], see Table 5.3.

The global roughness exponents (α) were calculated via structure factor analysis, Eq. 5.11. Similar to linearly expanding interfaces, for the radially expanding interface in media with quenched disorder, the global roughness exponents are in the same range and independent

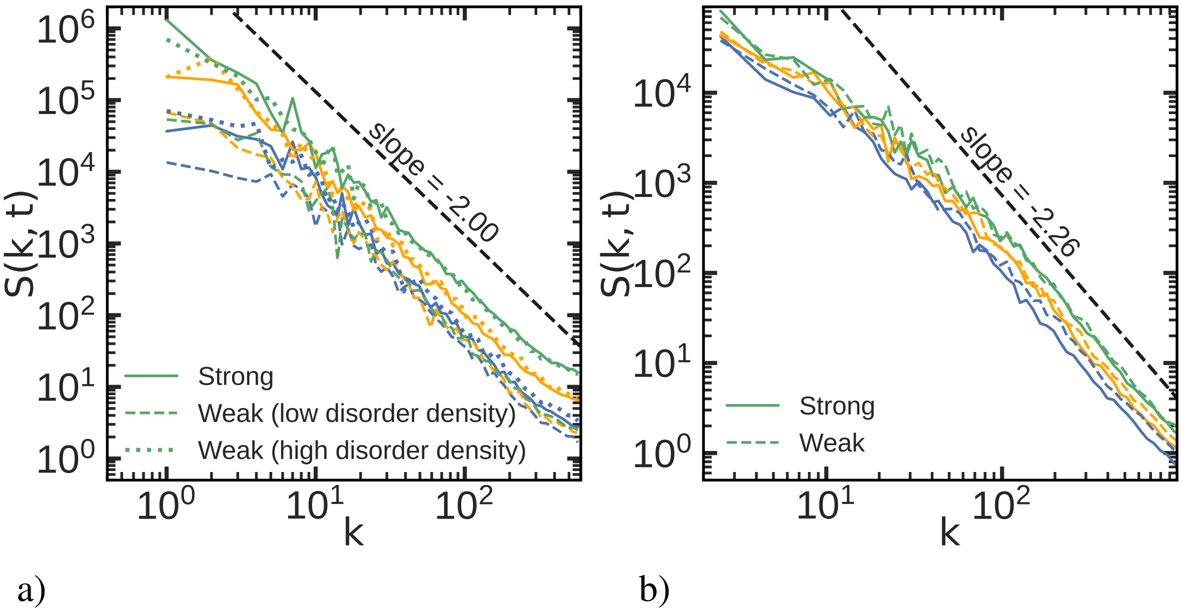

Figure 5.5: The structure factor (Eq. 5.10) measured at three different times, green: long time; orange: intermediate time; blue: short time, and different conditions (indicated by line type; legend). (a) For the linear interface: Solid lines: strong cell-cell adhesion and low disorder density; dashed lines: weak adhesion, low disorder density; dotted lines: weak adhesion, high disorder density. The black dashed line with a slope of = −2.0 is drawn to guide the eye. (b) for the radial interface at low disorder density: Solid lines: strong cell-cell adhesion; dashed lines: weak adhesion. The black dashed line with a slope of = −2.26 is drawn to guide the eye. The global roughening exponent for each case is reported in Table 5.3. For units, see Table 5.1.

Table 5.3: Interface fractal dimension (d_f), global (α) and local (α_loc) roughness exponents, correlation function exponent (ζ; Eq. 5.5), growth exponent (β), and average step height exponent (λ), in different configurations with different cell-cell adhesion stiffness strengths, and quenched disorder densities, see Tables 5.1 and 5.2. For the DLA-like chiral geometry, the fractal dimension is the colony fractal dimension. The exponents for the well-knows cases of KPZ, qKPZ and MBE for one-dimensional interfaces are also given for reference. $\dagger$ indicates experiments in heterogeneous media and $*$ indicates the crossover with two different regimes.

Configuration	Adhesion	d_f	α	α_loc	ζ	β	λ
Kardar-Parisi-Zhang (KPZ) [5]	-	-	1/2	1/2	-	1/3	-
quenched KPZ (qKPZ) [289]	-	-	3/4	3/4	-	3/5	-
Molecular beam epitaxy (MBE) [86]	-	-	3/2	1.0	-	3/8	-
linear interface at high disorder density	weak	1.33 ± 0.06	0.50 ± 0.03	0.53 ± 0.05	0.53 ± 0.01	0.49 ± 0.07	-
linear interface at low disorder density	weak	1.34 ± 0.03	0.52 ± 0.04	0.53 ± 0.02	0.53 ± 0.01	0.33 ± 0.08	-
linear interface	strong	1.28 ± 0.07	0.47 ± 0.07	0.55 ± 0.05	0.53 ± 0.01	0.67 ± 0.07	-
circular interface at high disorder density DLA-like chiral geometry	weak	1.74 ± 0.06	-	-	-	-	-
circular interface at low disorder density	weak	1.23 ± 0.02	0.64 ± 0.04	0.60 ± 0.02	0.58 ± 0.01	0.46 ± 0.13	-
circular interface	strong	1.23 ± 0.01	0.63 ± 0.04	0.62 ± 0.02	0.58 ± 0.01	0.47 ± 0.13	-
Mazarei *et al.* [14] (linear interface)	weak	1.22 ± 0.01	0.75 ± 0.04	0.59 ± 0.01	0.51 ± 0.01* 0.31 ± 0.03*	0.28 ± 0.01	0.02 ± 0.01
Mazarei *et al.* [14] (linear interface)	strong	1.26 ± 0.01	0.52 ± 0.02	0.62 ± 0.02	0.55 ± 0.01* 0.33 ± 0.04*	0.25 ± 0.02	0.01 ± 0.01
Mazarei *et al.* [14] (circular interface)	weak	1.13 ± 0.01	0.95 ± 0.04	0.66 ± 0.01	0.59 ± 0.01* 0.32 ± 0.01*	0.40 ± 0.04	0.37 ± 0.01
Mazarei *et al.* [14] (circular interface)	strong	1.21 ± 0.01	0.71 ± 0.02	0.70 ± 0.01	0.60 ± 0.01* 0.35 ± 0.01*	0.42 ± 0.06	0.47 ± 0.01
Bru *et al.* [13] (circular interface)	-	1.12−1.34 ± 0.03	1.5 ± 0.15	0.90 ± 0.10	-	0.38 ± 0.07	-
Huergo *et al.* [89] (circular & Vero Cells)	-	1.20 ± 0.05	0.5 ± 0.05	-	-	0.32 ± 0.04	-
Huergo *et al.* [4] (circular & HeLa Cells)	-	1.20 ± 0.05	0.5 ± 0.05	-	-	0.32 ± 0.04	-
Huergo *et al.*† [83] (linear & Vero Cells)	-	-	0.63 ± 0.03	-	-	0.75 ± 0.05	-
Vicsek *et al.*† [82] (linear interface)	-	-	0.78 ± 0.07	-	-	-	-
Galeano *et al.*† [253] (circular interface)	-	1.18 ± 0.02	0.86 ± 0.04	-	-	-	-
Rapin *et al.*† [279] (linear interface)	-	-	-	-	0.58* 0.13 − 0.25*	-	-

of the adhesion strengths, where, as previously mentioned, the global roughness exponent is dependent on the adhesion strength in the absence of quenched disorder, see Fig. 5.5 and Table 5.3.

The global roughness exponents in media with quenched disorder, similar to linearly expanding interfaces, are smaller than the global roughness exponents for the radially expanding interface in media without quenched disorder [14], see Table 5.3.

The correlation exponents (ζ) were obtained by determining the height-height correlation function, Eq. 5.5, shown in Fig. 5.6, and they have the same value at both strong and weak adhesion strengths, see Table 5.3. Figure 5.6 shows the height-height correlation functions for radially expanding interfaces in media without quenched disorder, and show a crossover with two different correlation exponents for both weak and strong cell-cell adhesion, see Table 5.3.

5.5 Discussion and conclusions

Comparison of the present data with previous results for epithelial tissue growth in media without quenched disorder [14] shows that quenched disorder can significantly alter the morphology of the interface and cell colony. It also affects cell motility and duplication rate in the colony, resulting in higher fractal dimensions and slower spreading rates. This is consistent with previous experiments for cell colony growth in plain and gel media [311, 83].

At the limit of high disorder concentration, colony growth exhibits branched chiral morphologies and the fractal dimension is quite close to the fractal dimension of clusters in diffusion-limited aggregation [306]. This has also been observed in bacterial growth on agar plates at low nutrient concentrations [308, 309, 310]. In the absence of quenched disorder, increasing adhesion strength affects the colony morphology and increases the interface fractal dimension [14]. Here, we have shown that the fractal dimension is independent of the cell-cell adhesion strength for colony expansion on heterogeneous substrates.

In the absence of disorder, adhesion strength is a crucial parameter that generates both KPZ and MBE-like scaling for colony expansion at strong and weak cell-cell adhesion strength, respectively [14]. Here, we have demonstrated that in the presence of quenched disorder, the local and global roughness exponent are independent of adhesion strength. This indicates that the effect of adhesion strength on interface roughness and morphology become insignificant on heterogeneous substrates. Disorder does, however, alter the growth exponent. The growth exponent for linear colony expansion at strong adhesion are within the margin of error of those obtained by Huergo *et al.* in experiments of linear interface expansion of Vero Cells in a gel medium [83]. However, in the case of the linear interface expansion at weak adhesion with both high and low disorder, the growth exponent is different from the one reported by Huergo *et al.*

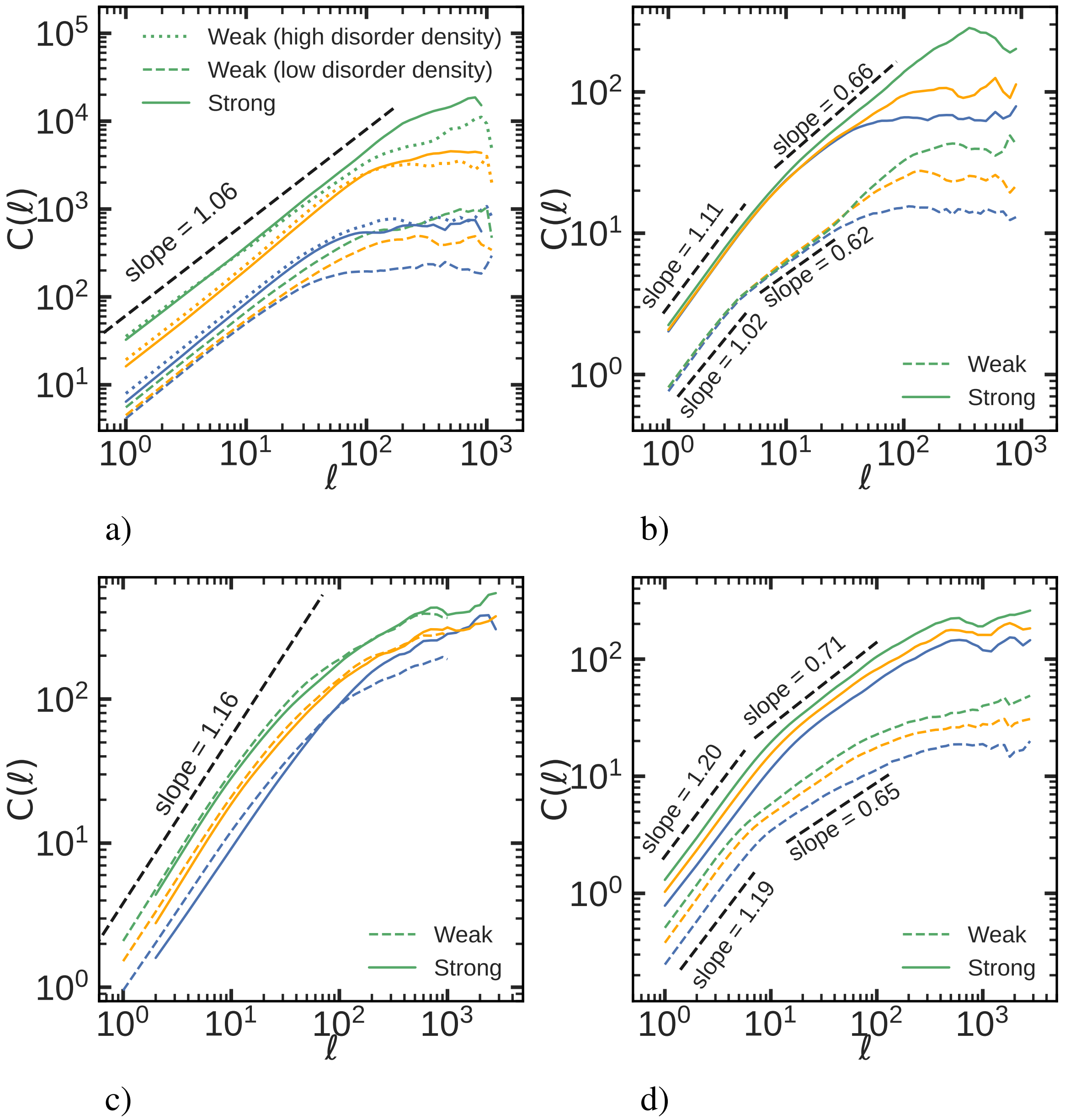

Figure 5.6: The height-height correlation function vs length (ℓ) for the linear interface in a medium (a) with quenched disorder (b) without quenched disorder, and for the radial interface in a medium (c) with quenched disorder (d) without quenched disorder at (green) long (orange) intermediate (blue) short time at different adhesion strengths and disorder densities: Solid lines: strong cell-cell adhesion and low disorder density; dashed lines: weak adhesion, low disorder density; dotted lines: weak adhesion, high disorder density. The correlation function exponents, ζ, are reported in the Table 5.3. For units, see Table 5.1.

At low disorder density and weak adhesion, colony expansion from a single line showed KPZ-like scaling. This is in contrast to the situation without disorder [14]. Although, increasing adhesion strength and disorder density does not affect the local and global roughness exponents, the higher disorder density leads to higher growth exponents and makes the scaling behavior of this configuration unclassified. The systems with radial growth at both weak and strong adhesion in media with low disorder density do not show any scaling universality class behavior. This is in contrast to the case of weak adhesion strength in the absence of disorder that displays MBE-like behavior [14]. These results indicate that the concepts of scaling behavior in characterizing cell colony growth should be used with caution due to sensitivity to parameters such as disorder concentration and cell-cell adhesion strengths.

The growth exponents for linear and radial interface growths differ for both strong and weak cell-cell adhesion. The fractal dimensions for radial interfaces are lower than the fractal dimensions for linear interfaces, and the local and global roughness exponents are greater for the radial interface than for the linear interface. The substrate topologies for linear and radial colony expansions are different. The radial configuration grows on a plane, whereas the linear configuration grows on a cylinder because of the periodicity in one direction. Both the plane and the cylinder have the same Gaussian curvature. However, the first homotopy groups of a plane and a cylinder are different, despite the fact that there is no local difference between the two. A continuous contraction to a point is possible for every closed loop in the plane, but only for some closed loops on the cylinder.

Independent of adhesion strength and geometries studied here, interface growth in media without quenched disorder does not belong to the superroughening or the intrinsic anomalous roughness subclasses reported in Refs. [305, 299, 87, 303, 300, 301]. The average step height exponent, λ, and the modified scaling ansatz for the height-height correlation function (Eq. 5.7) [115, 298], are also not applicable to the type of anomalous behavior in interface growth in media without quenched disorder. The results imply the existence of a new type of anomalous behavior, perhaps necessitating a new scaling ansatz for the interface width scaling relation.

Acknowledgments

MK thanks the Discovery and Canada Research Chairs Programs of the Natural Sciences and Engineering Research Council of Canada (NSERC) for financial support. MM thanks Western University's Science International Engagement Fund (SIEF) for travel support. Computational resources were provided by the Finnish Grid and Cloud Infrastructure FGCI, funded by the Academy of Finland, grant 304973.

Chapter 6

Conclusions and Future Work

6.1 Conclusions

In this thesis, we have studied the growth kinetics and interface roughness dynamics of cell population growth using a kinetic division model, *CellSim3D*, for deformable cells in medium with and without quenched disorder. *CellSim3D* is a 3D cell simulator utilized for studying cellular tissue mechanics. In the first version of the package [10], cells were modelled as mechanical objects that can have a symmetric random division and mechanical interaction with their environment within a box with rigid walls. The force field was composed of intramembrane forces, cell-cell adhesion and repulsion, cell-cell and cell-environment friction, internal pressure, and random forces for Brownian motion.

In this study, we have implemented several new features to the previous version of *CellSim3D*. In the current version of *CellSim3D*, the boundary conditions have been expanded to include periodic boundary conditions and Lees-Edwards boundary conditions, enabling the simulation of bulk systems in a simple shear flow. Additionally, the current version enables asymmetric division rule. The addition of this division rule to *CellSim3D* makes it permissible to have two daughter cells with different sizes after the cell division [312]. This type of cell division is essential for the differentiation of stem cells into cells with distinct mechanical properties, morphology, and biological function [209, 210, 211].

Apoptosis of cells has also been implemented in the current version of *CellSim3D*. It is modeled as a Poisson process in which the average interval between the events remains constant, and each cell undergoes apoptosis at a random time, regardless of preceding events. The latest version also offers bicellular tissue simulations in which cells can differ in cell-cell and cell-environment friction, size, internal pressure, growth rate, division threshold size, membrane stiffness, and apoptosis characteristics such as shrinking rate. Finally, cells can take ellipsoidal shapes in addition to the spherical shape that was the only option in the previous edition.

The current software version can operate on multiple GPUs with MPI communication between GPUs. The multi-GPU version allows us to boost throughput by performing several processes in parallel on multiple GPUs and by processing larger data volumes than a single GPU's memory can support. Both spatial domain decomposition and processor communication are based on the algorithm defined in Ref. [12]. Using OpenMPI libraries, a CUDA-aware MPI version of *CellSim3D* is also available. This version provides direct GPU-to-GPU communications made possible by the NVIDIA GPUDirect technology [236], reducing the data communication time among processors.

Decades have been devoted to the study of the interface roughness scaling of growing epithelial tissue, but the question of the universality of colonies' interface roughness scaling remains open. It is intriguing to speculate on what would happen to adaptive evolution if cell colony expansion dynamics were forced into a single dynamical universality class. The previous findings showed that nutrition, apoptosis, substrate heterogeneity, and mechanical stresses form a range of sources cause changes in both quantitative and qualitative tissue growth behaviors, see Refs. [32, 258, 52].

Different scaling phenomena, such as the Kardar-Parisi-Zhang (KPZ) and Molecular Beam Epitaxy (MBE) universality classes, and the complete absence of universality, have been reported in different research [87, 89, 4, 83, 254]. It is plausible to believe that the tissue's mechanical properties influence both the effectiveness of evolution and the adaptability of growth dynamics. In this thesis, we investigated the effect of mechanical parameters on the scaling behaviors of epithelial tissue growth and settled the apparent scaling disagreement in the previous experimental findings [87, 89, 4, 83].

We demonstrated that the interface roughness scales in the MBE-like universality class under the conditions of weak cell-cell adhesion and isotropic colony growth. Experimental studies by Brú *et al.* [13, 87] on the surface scaling of epithelial tumors *in vitro* and *in vivo* confirm this finding. In contrast, a KPZ-like scaling is observed in line configuration colonies with strong cell-cell adhesion. Experiments conducted by Huergo *et al.* confirm this finding [4, 88, 89].

Regardless of the growth scaling behavior, the fractal dimensions of the interface ranged between 1.13 and 1.26 in all of the examined examples of cell colony growth in medium without quenched disorder. This is consistent with earlier experimental studies on epithelial tissues [13, 88, 89, 4, 253]. However, for both circular and linear configurations, the interface fractal dimension was shown to be slightly higher under conditions of strong cell-cell adhesion. This is consistent with the findings of Torres Hoyos *et al.* [252], who discovered that malignant and invasive tumors with less cell-cell adhesion have a smaller fractal dimension than benign tumors with higher adhesion among cells.

All examples of radial expansion and line growth with varying adhesion parameters revealed linear expansion at a constant rate. In the experimental studies, Brú *et al.* [13] discovered that radially growing cell colonies initially develop exponentially and subsequently linearly with time. Similarly, Huergo *et al.* [89, 4] observed that once the cell population exceeds 700–1,000 cells, radially expanding colonies grow at a constant velocity, and the line configuration expansion is also governed by the law of constant velocity [88]. These findings directly contradict the Gomperzian model of cancer growth, see Ref. [262]. This suggests that cells are partially contact-inhibited and that the majority of activity occurs within a narrow strip along the interface. We also observed that increases in cell-cell adhesion decrease frontal velocities in both linear and radial configurations.

We observed that the cell-cell adhesion and the global roughness exponent have an inverse relationship. As adhesion strength increases, the exponent of global roughness decreases. Furthermore, we showed that the global roughness exponent is insensitive to changes in cell-medium friction, intermembrane friction, symmetric and asymmetric types of cell division, and having two different types of cells with different cell membrane stiffness in a radially expanding system.

In addition, the development of epithelial tissues in a medium with quenched disorder in both a linear and radial configuration was analyzed. We studied the situation where the disorder density is just below the critical density at which the interface becomes trapped by the disordered substrate. Under such circumstances, the velocity of the interface is constant from the beginning. In both linear and radial interface growth at both strong and weak adhesion strengths, the fractal dimension of the system in a medium with quenched disorder was greater than the fractal dimension of the interface in a medium without quenched disorder. We also found that, in contrast to colony growth in medium without quenched disorder, the fractal dimension of the colony interface does not increase when the strength of cell-cell adhesion is increased.

We found that both the local and global roughness exponents of radial and linear interfaces are smaller when quenched disorder is present than when it is not. We also found that in the presence of quenched disorder, the growth exponent is higher than in the absence of quenched disorder. The values of the local and global roughness exponents in colony expansion on a heterogeneous substrate are found to be unrelated to cell-cell adhesion strength, while the growth exponent is found to still be dependent on adhesion strength.

We also examined cell proliferation in radially expanding colonies in a disordered medium at weak cell-cell adhesion strength at high disorder density. At low disorder density, the colonies maintain their spherical shape, and the interface advances at a slow and steady rate. However, at high disorder density, the disordered substrate pins the interface. Under this condition, colonies form slowly into chiral morphologies with branching structures, and their colony fractal dimension values are in close accordance with simulations of the DLA fractal model [306], as observed by experimental studies of bacterial growth on agar plates under conditions of low nutrient concentration [313, 81, 93].

We discovered that the substrate topology influences both the interface roughness exponents and fractal dimension. The radial interface growth has higher local and global roughness exponents than the linear interface growth. The interface fractal dimension is smaller for the radial than the linear colony expansion. Due to periodicity in only one direction, the linear configuration expands along the surface of a cylinder, whereas the radial configuration expands on a flat plane. A plane and a cylinder have distinct first homotopy groups. Every closed loop in the plane can undergo a continuous contraction to a point, whereas only a subset of closed loops on the cylinder can continuously contract to a point.

Many studies have been conducted in recent decades to identify the fundamental characteristics of cell and tumor growth [13, 4, 314, 315, 316, 91]. Understanding the fundamental mechanisms of tumor growth is crucial for comprehending how tumors grow and spread, which aids in the development of novel diagnostic and treatment techniques. Previous experimental studies have reported different scaling universality classes, including KPZ and MBE, for tumor interface roughness [13, 87, 89, 4, 253]. In each of these universality classes, the underlying surface growth mechanism is distinct. We indicate that the underlying mechanism of surface growth in tumor progression cannot be described by a single scaling universality class and strongly depends on multiple factors, including cell-cell adhesion and substrate heterogeneity.

6.2 Future Work

6.2.1 Cell Division Rules

One of the important mechanism among the many ways multicellular organisms regulate the topology and geometry of their tissues is the orientation of cell division planes. The current version of *CellSim3D* uses a random direction chosen by sampling a unit vector from a sphere to find the normal vector to the cell division plane. In symmetric division, the plane of cell division crosses through the center of the mass of the cell; in asymmetric division, the plane is displaced from the center, causing the cell to divide into two different sizes. The division rule can also be done due to the geometrical rule where the division plane is along the shortest path [317], and the mechanical rule where the division plane is along the maximal tension axis [318].

In order to implement the geometrical hypothesis, we can use a method similar to the shortest path version of Errera's rule, picking the direction of division, $\vec{\mathbf{n}}$, based on how much it reduces the cell shape [215, 318],

$$\vec{\mathbf{n}}^t \mathbf{M}_C \vec{\mathbf{n}} = \min\{\vec{\mathbf{u}}^t \mathbf{M}_C \vec{\mathbf{u}}\}_{\|\vec{\mathbf{u}}\|=1}, \tag{6.1}$$

where $\mathbf{M}_C$ is the shape tensor of the cell. According to the mechanical hypothesis, the stress is maximum along the division direction, $\vec{\mathbf{n}}$, which follows the following condition:

$$\vec{\mathbf{n}}^t \mathbf{S}_C \vec{\mathbf{n}} = \max\{\vec{\mathbf{u}}^t \mathbf{S}_C \vec{\mathbf{u}}\}_{\|\vec{\mathbf{u}}\|=1}, \tag{6.2}$$

where $\mathbf{S}_C$ is the stress tensor derived from the energy density's functional derivative with respect to its strain [318].

6.2.2 Cell Polarity

In both the previous [10] and upgraded versions of *CellSim3D*, we assumed that cell adhesion molecules (CAMs) are always uniformly distributed over the cell surface. However, proteins and other biological components are not distributed equally throughout the surface of a polarized cell. Polarity in a cell determines the position and function of adhesion molecules [263, 264, 265]. Cell migration [319], differentiation [320], and maybe even division [321] are just a few of the processes that are affected by cell polarity. Polarized cells may exhibit directional differences in their mechanical properties and cell-cell interactions.

In cell models such as the Vertex model [78] and the Cellular Potts Model [322] the standard way to introduce polarity is to define a polarity vector $\hat{\mathbf{P}}$. In the current version of *CellSim3D*, the adhesion spring constant is represented as a constant across all cell nodes. Alternately, we can make it depend on the orientation of the node within the cell. Consequently, the spring constant k^A can be expressed as $k^{inter} = k^A(\hat{\mathbf{r}}_i \cdot \hat{\mathbf{P}}_m)$ for any r_i such that $\mathbf{r}_i = \mathbf{x}_i - \bar{\mathbf{x}}_m$, where $\bar{\mathbf{x}}_m$ is the center of mass of the cell m. Hence, intermembrane forces become attractive if they act in the direction of the polarity vector, and repulsive if they act in the opposite direction. Other parameters, such as the coefficients of intermembrane friction (γ_{int}), can also be extended in the same manner.

6.2.3 Multicellular Tissue Simulation

During embryonic development, biological tissue structures form as a result of complex multicellular processes. To know and understand how diverse multicellular behaviors affect the development of tissue morphology, it is necessary to model the mechanical interconnections between diverse cellular activities in multicellular tissues. An object-oriented version of *CellSim3D* is the simplest approach to simulating cells of varying types and characteristics. To ensure efficient object-oriented programming on the GPU without losing performance, various considerations are necessary.

On single instruction, multiple data (SIMD) architectures such as GPU, object-oriented programming can be slow due to inefficient memory access. The most time-consuming part of processing data is moving it into and out of vector registers. In this case, creating a database containing identical objects in the well-known Structure of Arrays (SOA) data layout will enhance memory access. As a result, all of a field's values can be stored in a single array. SOA is the usual data structure for GPU programmers to achieve optimal efficiency. There are a few libraries and prototypes that enable object-oriented programming on GPUs without losing performance, see Refs. [323, 324].

6.2.4 Surface Analysis

Single-cell or collective motion can regulate cellular migration, both of which are dependent on intercellular interactions and intracellular regulation. All of these processes contribute to the growth of biological matter, such as the expansion of tissues and the invasion of tumors. Using *CellSim3D*, we can examine how the mechanical properties of cells, as well as cell division and apoptosis, affect the dynamics and morphology of tissue growth and the tumors invasion. One-dimensional interface roughness is analyzed as a function of a group of these factors including, cell-cell adhesion and cell-cell friction. Furthermore, we can study the effect of other parameters, such as cell division, apoptosis rate, and cell shape, on tissue growth and interface roughness.

Scaling exponents for systems with $d > 1$ are frequently determined numerically due to intractable mathematical difficulties. *CellSim3D* is a three-dimensional model capable of representing three-dimensional tissues. As we did for the $1 + 1$ system, we can simulate a three-dimensional tissue to determine the roughness exponents and how they depend on mechanical parameters such as cell-cell adhesion and cell-environment friction and other parameters, such as cell division rules and cell division and apoptosis rates that influence tissue homeostatic pressure.

Bibliography

[1] M. Moradi and E. Nazockdast, “Cell nucleus as a microrheological probe to study the rheology of the cytoskeleton,” *Biophysical Journal*, vol. 120, no. 9, pp. 1542–1564, 2021.

[2] T. D. Pollard, W. C. Earnshaw, J. Lippincott-Schwartz, and G. Johnson, *Cell biology E-book*. Philadelphia, PA, USA, Elsevier, 2016.

[3] Wikipedia, “Apoptosis.” `https://es.wikipedia.org/wiki/Apoptosis`, accessed, Jan 10, 2023.

[4] M. A. C. Huergo, M. Pasquale, P. H. González, A. E. Bolzán, and A. J. Arvia, “Growth dynamics of cancer cell colonies and their comparison with noncancerous cells,” *Physical Review E*, vol. 85, no. 1, p. 011918, 2012.

[5] M. Kardar, G. Parisi, and Y.-C. Zhang, “Dynamic scaling of growing interfaces,” *Physical Review Letters*, vol. 56, no. 9, p. 889, 1986.

[6] A.-L. Barabási, H. E. Stanley, *et al.*, *Fractal concepts in surface growth*. Cambridge, UK, Cambridge University Press, 1995.

[7] M. J. Vold, “Computer simulation of floc formation in a colloidal suspension,” *Journal of Colloid Science*, vol. 18, no. 7, pp. 684–695, 1963.

[8] B. Costa, J. Euzébio, and F. A. Reis, “Finite-size effects on the growth models of das sarma and tamborenea and wolf and villain,” *Physica A: Statistical Mechanics and its Applications*, vol. 328, no. 1-2, pp. 193–204, 2003.

[9] S. Buldyrev, A.-L. Barabási, F. Caserta, S. Havlin, H. Stanley, and T. Vicsek, “Anomalous interface roughening in porous media: Experiment and model,” *Physical Review A*, vol. 45, no. 12, p. R8313, 1992.

[10] P. Madhikar, J. Åström, J. Westerholm, and M. Karttunen, “Cellsim3d: Gpu accelerated software for simulations of cellular growth and division in three dimensions,” *Computer Physics Communications*, vol. 232, pp. 206–213, 2018.

[11] A. Smith, M. A. Parkes, G. K. Atkin-Smith, R. Tixeira, and I. K. Poon, “Cell disassembly during apoptosis,” *WikiJournal of Medicine*, vol. 4, no. 1, pp. 1–3, 2017.

[12] S. Plimpton, “Fast parallel algorithms for short-range molecular dynamics,” *Journal of Computational Physics*, vol. 117, no. 1, pp. 1–19, 1995.

[13] A. Brú, S. Albertos, J. L. Subiza, J. L. García-Asenjo, and I. Brú, “The universal dynamics of tumor growth,” *Biophysical Journal*, vol. 85, no. 5, pp. 2948–2961, 2003.

[14] M. Mazarei, J. Åström, J. Westerholm, and M. Karttunen, “In silico testing of the universality of epithelial tissue growth,” *Physical Review E*, vol. 106, no. 6, p. L062402, 2022.

[15] A. Mkrtchyan, J. Åström, and M. Karttunen, “A new model for cell division and migration with spontaneous topology changes,” *Soft Matter*, vol. 10, no. 24, pp. 4332–4339, 2014.

[16] W. F. Scherer, J. T. Syverton, and G. O. Gey, “Studies on the propagation in vitro of poliomyelitis viruses. IV. Viral multiplication in a stable strain of human malignant ep-

ithelial cells (strain HeLa) derived from an epidermoid carcinoma of the cervix," *Journal of Experimental Medicine*, vol. 97, no. 5, pp. 695–710, 1953.

[17] B. Ji and G. Bao, "Cell and molecular biomechanics: perspectives and challenges," *Acta Mechanica Solida Sinica*, vol. 24, no. 1, pp. 27–51, 2011.

[18] K. Rosowski, "Introduction to cell mechanics and mechanobiology," *The Yale Journal of Biology and Medicine*, vol. 86, no. 3, p. 436, 2013.

[19] S. Kumar and V. M. Weaver, "Mechanics, malignancy, and metastasis: the force journey of a tumor cell," *Cancer and Metastasis Reviews*, vol. 28, pp. 113–127, 2009.

[20] T. Mammoto and D. E. Ingber, "Mechanical control of tissue and organ development," *Development*, vol. 137, no. 9, pp. 1407–1420, 2010.

[21] D. E. Jaalouk and J. Lammerding, "Mechanotransduction gone awry," *Nature Reviews Molecular Cell Biology*, vol. 10, no. 1, pp. 63–73, 2009.

[22] Y.-c. Fung, *Biomechanics: mechanical properties of living tissues*. New York, NY, USA, Springer Science & Business Media, 2013.

[23] Y. Fung, "Motion, flow, stress and growth," *Biomechanics. Springer–Verlag*, 1990.

[24] J. D. Humphrey, *Cardiovascular solid mechanics: cells, tissues, and organs*. New York, NY, USA, Springer Science & Business Media, 2013.

[25] D. Bray, *Cell movements: from molecules to motility*. New York, NY, USA, Garland Science, 2000.

[26] S. C. Cowin, "Tissue growth and remodeling," *Annu. Rev. Biomed. Eng.*, vol. 6, pp. 77–107, 2004.

[27] M. Dao, C. T. Lim, and S. Suresh, “Mechanics of the human red blood cell deformed by optical tweezers,” *Journal of the Mechanics and Physics of Solids*, vol. 51, no. 11-12, pp. 2259–2280, 2003.

[28] S. Suresh, “Biomechanics and biophysics of cancer cells,” *Acta biomaterialia*, vol. 3, no. 4, pp. 413–438, 2007.

[29] J. R. Lange and B. Fabry, “Cell and tissue mechanics in cell migration,” *Experimental Cell Research*, vol. 319, no. 16, pp. 2418–2423, 2013.

[30] J. H. Shawky and L. A. Davidson, “Tissue mechanics and adhesion during embryo development,” *Developmental Biology*, vol. 401, no. 1, pp. 152–164, 2015.

[31] A.-L. Routier-Kierzkowska, A. Weber, P. Kochova, D. Felekis, B. J. Nelson, C. Kuhlemeier, and R. S. Smith, “Cellular force microscopy for in vivo measurements of plant tissue mechanics,” *Plant Physiology*, vol. 158, no. 4, pp. 1514–1522, 2012.

[32] T. Lecuit and P.-F. Lenne, “Cell surface mechanics and the control of cell shape, tissue patterns and morphogenesis,” *Nature Reviews Molecular Cell Biology*, vol. 8, no. 8, pp. 633–644, 2007.

[33] K. Goodwin and C. M. Nelson, “Mechanics of development,” *Developmental Cell*, vol. 56, no. 2, pp. 240–250, 2021.

[34] M. Murrell, P. W. Oakes, M. Lenz, and M. L. Gardel, “Forcing cells into shape: the mechanics of actomyosin contractility,” *Nature Reviews Molecular Cell Biology*, vol. 16, no. 8, pp. 486–498, 2015.

[35] B. Alberts, D. Bray, K. Hopkin, A. D. Johnson, J. Lewis, M. Raff, K. Roberts, and P. Walter, *Essential cell biology*. New York, NY, USA, Garland Science, 2015.

[36] J. Lombard, “Once upon a time the cell membranes: 175 years of cell boundary research,” *Biology Direct*, vol. 9, no. 1, pp. 1–35, 2014.

[37] B. Martinac, Y. A. Nikolaev, G. Silvani, N. Bavi, V. Romanov, Y. Nakayama, A. D. Martinac, P. Rohde, O. Bavi, and C. D. Cox, "Cell membrane mechanics and mechanosensory transduction," *Current Topics in Membranes*, vol. 86, pp. 83–141, 2020.

[38] A. Janshoff, "Viscoelastic properties of epithelial cells," *Biochemical Society Transactions*, vol. 49, no. 6, pp. 2687–2695, 2021.

[39] M. Bezanilla, A. S. Gladfelter, D. R. Kovar, and W.-L. Lee, "Cytoskeletal dynamics: a view from the membrane," *Journal of Cell Biology*, vol. 209, no. 3, pp. 329–337, 2015.

[40] D. A. Fletcher and R. D. Mullins, "Cell mechanics and the cytoskeleton," *Nature*, vol. 463, no. 7280, pp. 485–492, 2010.

[41] E. Nogales, "Cytoskeleton in high resolution," *Nature Reviews Molecular Cell Biology*, vol. 19, no. 3, pp. 142–142, 2018.

[42] M. P. Murrell and M. L. Gardel, "F-actin buckling coordinates contractility and severing in a biomimetic actomyosin cortex," *Proceedings of the National Academy of Sciences*, vol. 109, no. 51, pp. 20820–20825, 2012.

[43] D. Boal and D. H. Boal, *Mechanics of the Cell.* Cambridge, UK, Cambridge University Press, 2012.

[44] Q. Wen and P. A. Janmey, "Polymer physics of the cytoskeleton," *Current Opinion in Solid State and Materials Science*, vol. 15, no. 5, pp. 177–182, 2011.

[45] J. Stricker, T. Falzone, and M. L. Gardel, "Mechanics of the f-actin cytoskeleton," *Journal of Biomechanics*, vol. 43, no. 1, pp. 9–14, 2010.

[46] K. M. Yamada and M. Sixt, "Mechanisms of 3d cell migration," *Nature Reviews Molecular Cell Biology*, vol. 20, no. 12, pp. 738–752, 2019.

[47] P. Murray, G. Frampton, and P. Nelson, "Cell adhesion molecules: Sticky moments in the clinic," *British Medical Journal*, vol. 319, no. 7206, pp. 332–334, 1999.

[48] M. Marin-Riera, M. Brun-Usan, R. Zimm, T. Välikangas, and I. Salazar-Ciudad, "Computational modeling of development by epithelia, mesenchyme and their interactions: a unified model," *Bioinformatics*, vol. 32, no. 2, pp. 219–225, 2016.

[49] C. Zhu, G. Bao, and N. Wang, "Cell mechanics: mechanical response, cell adhesion, and molecular deformation," *Annual Review of Biomedical Engineering*, vol. 2, no. 1, pp. 189–226, 2000.

[50] M. A. Wozniak, K. Modzelewska, L. Kwong, and P. J. Keely, "Focal adhesion regulation of cell behavior," *Biochimica et Biophysica Acta (BBA)-Molecular Cell Research*, vol. 1692, no. 2-3, pp. 103–119, 2004.

[51] M. Rauzi, P. Verant, T. Lecuit, and P.-F. Lenne, "Nature and anisotropy of cortical forces orienting drosophila tissue morphogenesis," *Nature Cell Biology*, vol. 10, no. 12, pp. 1401–1410, 2008.

[52] D. T. Tambe, C. Corey Hardin, T. E. Angelini, K. Rajendran, C. Y. Park, X. Serra-Picamal, E. H. Zhou, M. H. Zaman, J. P. Butler, D. A. Weitz, *et al.*, "Collective cell guidance by cooperative intercellular forces," *Nature Materials*, vol. 10, no. 6, pp. 469–475, 2011.

[53] L.-L. Pontani, I. Jorjadze, V. Viasnoff, and J. Brujic, "Biomimetic emulsions reveal the effect of mechanical forces on cell–cell adhesion," *Proceedings of the National Academy of Sciences*, vol. 109, no. 25, pp. 9839–9844, 2012.

[54] Z. Liu, J. L. Tan, D. M. Cohen, M. T. Yang, N. J. Sniadecki, S. A. Ruiz, C. M. Nelson, and C. S. Chen, "Mechanical tugging force regulates the size of cell–cell junctions," *Proceedings of the National Academy of Sciences*, vol. 107, no. 22, pp. 9944–9949, 2010.

[55] D. Sánchez-Gutiérrez, M. Tozluoglu, J. D. Barry, A. Pascual, Y. Mao, and L. M. Escudero, “Fundamental physical cellular constraints drive self-organization of tissues,” *The European Molecular Biology Organization Journal*, vol. 35, no. 1, pp. 77–88, 2016.

[56] G. A. Ateshian, B. Morrison III, J. W. Holmes, and C. T. Hung, “Mechanics of cell growth,” *Mechanics Research Communications*, vol. 42, pp. 118–125, 2012.

[57] L. A. Taber, “Biomechanics of growth, remodeling, and morphogenesis,” *Applied Mechanics Reviews*, vol. 48, no. 8, pp. 487–545, 1995.

[58] S. Inoué, “Cell division and the mitotic spindle,” *The Journal of Cell Biology*, vol. 91, no. 3, p. 131, 1981.

[59] L. L. Satterwhite and T. D. Pollard, “Cytokinesis,” *Current Opinion in Cell Biology*, vol. 4, no. 1, pp. 43–52, 1992.

[60] E. R. Angert, “Alternatives to binary fission in bacteria,” *Nature Reviews Microbiology*, vol. 3, no. 3, pp. 214–224, 2005.

[61] N. Kleckner, “Meiosis: how could it work?,” *Proceedings of the National Academy of Sciences*, vol. 93, no. 16, pp. 8167–8174, 1996.

[62] S. Elmore, “Apoptosis: a review of programmed cell death,” *Toxicologic Pathology*, vol. 35, no. 4, pp. 495–516, 2007.

[63] A. M. Jones, “Programmed cell death in development and defense,” *Plant Physiology*, vol. 125, no. 1, pp. 94–97, 2001.

[64] J. Tower, “Programmed cell death in aging,” *Ageing Research Reviews*, vol. 23, pp. 90–100, 2015.

[65] J. F. Kerr, C. M. Winterford, and B. V. Harmon, “Apoptosis. its significance in cancer and cancer therapy,” *Cancer*, vol. 73, no. 8, pp. 2013–2026, 1994.

[66] A. Ambrosini, M. Gracia, A. Proag, M. Rayer, B. Monier, and M. Suzanne, "Apoptotic forces in tissue morphogenesis," *Mechanisms of Development*, vol. 144, pp. 33–42, 2017.

[67] A. M. Green and N. D. Steinmetz, "Monitoring apoptosis in real time," *The Cancer Journal*, vol. 8, no. 2, pp. 82–92, 2002.

[68] G. Majno and I. Joris, "Apoptosis, oncosis, and necrosis. an overview of cell death.," *The American Journal of Pathology*, vol. 146, no. 1, p. 3, 1995.

[69] Y. Zhang, X. Chen, C. Gueydan, and J. Han, "Plasma membrane changes during programmed cell deaths," *Cell Research*, vol. 28, no. 1, pp. 9–21, 2018.

[70] F. Azuaje, "Computational discrete models of tissue growth and regeneration," *Briefings in Bioinformatics*, vol. 12, no. 1, pp. 64–77, 2011.

[71] J. Fisher and T. A. Henzinger, "Executable cell biology," *Nature Biotechnology*, vol. 25, no. 11, pp. 1239–1249, 2007.

[72] H. Kitano, "Computational systems biology," *Nature*, vol. 420, no. 6912, pp. 206–210, 2002.

[73] B. Aguda and A. Friedman, *Models of cellular regulation*. Oxford, UK, Oxford University Press, 2008.

[74] J. C. Sible and J. J. Tyson, "Mathematical modeling as a tool for investigating cell cycle control networks," *Methods*, vol. 41, no. 2, pp. 238–247, 2007.

[75] J. Wattis, B. O'Malley, H. Blackburn, L. Pickersgill, J. Panovska, H. Byrne, and K. Jackson, "Mathematical model for low density lipoprotein (ldl) endocytosis by hepatocytes," *Bulletin of Mathematical Biology*, vol. 70, pp. 2303–2333, 2008.

[76] M. Radszuweit, M. Block, J. Hengstler, E. Schöll, and D. Drasdo, “Comparing the growth kinetics of cell populations in two and three dimensions,” *Physical Review E*, vol. 79, no. 5, p. 051907, 2009.

[77] M. Block, E. Schöll, and D. Drasdo, “Classifying the expansion kinetics and critical surface dynamics of growing cell populations,” *Physical Review Letters*, vol. 99, no. 24, p. 248101, 2007.

[78] A. G. Fletcher, M. Osterfield, R. E. Baker, and S. Y. Shvartsman, “Vertex models of epithelial morphogenesis,” *Biophysical Journal*, vol. 106, no. 11, pp. 2291–2304, 2014.

[79] P. Van Liedekerke, M. Palm, N. Jagiella, and D. Drasdo, “Simulating tissue mechanics with agent-based models: concepts, perspectives and some novel results,” *Computational Particle Mechanics*, vol. 2, no. 4, pp. 401–444, 2015.

[80] A. Anderson and K. Rejniak, *Single-cell-based models in biology and medicine*. New York, NY, USA, Springer Science & Business Media, 2007.

[81] H. Fujikawa and M. Matsushita, “Fractal growth of bacillus subtilis on agar plates,” *Journal of the Physical Society of Japan*, vol. 58, no. 11, pp. 3875–3878, 1989.

[82] T. Vicsek, M. Cserző, and V. K. Horváth, “Self-affine growth of bacterial colonies,” *Physica A: Statistical Mechanics and its Applications*, vol. 167, no. 2, pp. 315–321, 1990.

[83] M. A. C. Huergo, N. E. Muzzio, M. A. Pasquale, P. P. González, A. E. Bolzán, and A. J. Arvia, “Dynamic scaling analysis of two-dimensional cell colony fronts in a gel medium: A biological system approaching a quenched kardar-parisi-zhang universality,” *Physical Review E*, vol. 90, no. 2, p. 022706, 2014.

[84] S. SenGupta, C. A. Parent, and J. E. Bear, “The principles of directed cell migration,” *Nature Reviews Molecular Cell Biology*, vol. 22, no. 8, pp. 529–547, 2021.

[85] S. F. Edwards and D. Wilkinson, "The surface statistics of a granular aggregate," *Proceedings of the Royal Society of London. A. Mathematical and Physical Sciences*, vol. 381, no. 1780, pp. 17–31, 1982.

[86] S. D. Sarma, S. Ghaisas, and J. Kim, "Kinetic super-roughening and anomalous dynamic scaling in nonequilibrium growth models," *Physical Review E*, vol. 49, no. 1, p. 122, 1994.

[87] A. Brú, J. M. Pastor, I. Fernaud, I. Brú, S. Melle, and C. Berenguer, "Super-rough dynamics on tumor growth," *Physical Review Letters*, vol. 81, no. 18, p. 4008, 1998.

[88] M. Huergo, M. Pasquale, A. Bolzán, A. Arvia, and P. González, "Morphology and dynamic scaling analysis of cell colonies with linear growth fronts," *Physical Review E*, vol. 82, no. 3, p. 031903, 2010.

[89] M. Huergo, M. Pasquale, P. González, A. Bolzán, and A. Arvia, "Dynamics and morphology characteristics of cell colonies with radially spreading growth fronts," *Physical Review E*, vol. 84, no. 2, p. 021917, 2011.

[90] J. Buceta and J. Galeano, "Comments on the article "the universal dynamics of tumor growth" by a. bru et al.," *Biophysical Journal*, vol. 88, no. 5, p. 3734, 2005.

[91] Y. Azimzade, A. A. Saberi, and M. Sahimi, "Effect of heterogeneity and spatial correlations on the structure of a tumor invasion front in cellular environments," *Physical Review E*, vol. 100, no. 6, p. 062409, 2019.

[92] S. N. Santalla and S. C. Ferreira, "Eden model with nonlocal growth rules and kinetic roughening in biological systems," *Physical Review E*, vol. 98, no. 2, p. 022405, 2018.

[93] M. Matsushita and H. Fujikawa, "Diffusion-limited growth in bacterial colony formation," *Physica A: Statistical Mechanics and its Applications*, vol. 168, no. 1, pp. 498–506, 1990.

[94] T. Hwa and M. Kardar, “Avalanches, hydrodynamics, and discharge events in models of sandpiles,” *Physical Review A*, vol. 45, no. 10, p. 7002, 1992.

[95] E. Hopf, “The partial differential equation u sub t+ uu sub x= mu sub xx,” tech. rep., INDIANA UNIV AT BLOOMINGTON, 1950.

[96] J. D. Cole, “On a quasi-linear parabolic equation occurring in aerodynamics,” *Quarterly of Applied Mathematics*, vol. 9, no. 3, pp. 225–236, 1951.

[97] M. Kardar, *Statistical physics of fields*. New York, NY, USA, Cambridge University Press, 2007.

[98] G. Da Prato and G. Da Prato, “The stochastic burgers equation,” *Kolmogorov Equations for Stochastic PDEs*, pp. 131–153, 2004.

[99] H. Bateman, “Some recent researches on the motion of fluids,” *Monthly Weather Review*, vol. 43, no. 4, pp. 163–170, 1915.

[100] L. Bertini, N. Cancrini, and G. Jona-Lasinio, “The stochastic burgers equation,” *Communications in Mathematical Physics*, vol. 165, no. 2, pp. 211–232, 1994.

[101] L. Braunstein, R. Buceta, A. Diaz-Sanchez, and N. Giovambattista, “A review of growing interfaces in quenched disordered media,” *Materials Instabilities*, pp. 281–303, 2000.

[102] F. D. Reis, “Depinning transitions in interface growth models,” *Brazilian Journal of Physics*, vol. 33, pp. 501–513, 2003.

[103] G. Parisi, “On surface growth in random media,” *Europhysics Letters*, vol. 17, no. 8, p. 673, 1992.

[104] Y. Imry and S.-k. Ma, “Random-field instability of the ordered state of continuous symmetry,” *Physical Review Letters*, vol. 35, no. 21, p. 1399, 1975.

[105] A. Dıaz-Sánchez, L. Braunstein, and R. Buceta, “Growing mechanisms in the qkpz equation aaand the dpd models,” *The European Physical Journal B-Condensed Matter and Complex Systems*, vol. 21, pp. 289–294, 2001.

[106] G. Blatter, M. V. Feigel’man, V. B. Geshkenbein, A. I. Larkin, and V. M. Vinokur, “Vortices in high-temperature superconductors,” *Reviews of Modern Physics*, vol. 66, no. 4, p. 1125, 1994.

[107] G. Grüner, “The dynamics of charge-density waves,” *Reviews of Modern Physics*, vol. 60, no. 4, p. 1129, 1988.

[108] F. Family, K. Chan, J. Amar, R. Jullien, J. Kertész, P. Meakin, and D. Wolf, “Surface disordering: growth, roughening and phase transitions,” *New York, NY, USA, Nova Science*, 1992.

[109] M. G. Lagally, *Kinetics of ordering and growth at surfaces*, vol. 239. New York, NY, USA, Springer Science & Business Media, 2012.

[110] D. A. Kessler, H. Levine, and L. M. Sander, “Molecular-beam epitaxial growth and surface diffusion,” *Physical Review Letters*, vol. 69, no. 1, p. 100, 1992.

[111] Z.-W. Lai and S. D. Sarma, “Kinetic growth with surface relaxation: Continuum versus atomistic models,” *Physical Review Letters*, vol. 66, no. 18, p. 2348, 1991.

[112] J. Villain, “Continuum models of crystal growth from atomic beams with and without desorption,” *Journal de physique I*, vol. 1, no. 1, pp. 19–42, 1991.

[113] D. Wolf and J. Villain, “Growth with surface diffusion,” *Europhysics Letters*, vol. 13, no. 5, p. 389, 1990.

[114] S. D. Sarma and P. Tamborenea, “A new universality class for kinetic growth: One-dimensional molecular-beam epitaxy,” *Physical Review Letters*, vol. 66, no. 3, p. 325, 1991.

[115] M. Kotrla and P. Šmilauer, "Nonuniversality in models of epitaxial growth," *Physical Review B*, vol. 53, no. 20, p. 13777, 1996.

[116] W. M. Tong and R. S. Williams, "Kinetics of surface growth: phenomenology, scaling, and mechanisms of smoothening and roughening," *Annual Review of Physical Chemistry*, vol. 45, no. 1, pp. 401–438, 1994.

[117] F. Family and T. Vicsek, "Scaling of the active zone in the eden process on percolation networks and the ballistic deposition model," *Journal of Physics A: Mathematical and General*, vol. 18, no. 2, p. L75, 1985.

[118] F. Family, "Dynamic scaling and phase transitions in interface growth," *Physica A: Statistical Mechanics and its Applications*, vol. 168, no. 1, pp. 561–580, 1990.

[119] J. M. López, M. Castro, and R. Gallego, "Scaling of local slopes, conservation laws, and anomalous roughening in surface growth," *Physical Review Letters*, vol. 94, no. 16, p. 166103, 2005.

[120] R. Baiod, D. Kessler, P. Ramanlal, L. Sander, and R. Savit, "Dynamical scaling of the surface of finite-density ballistic aggregation," *Physical Review A*, vol. 38, no. 7, p. 3672, 1988.

[121] P. Meakin, P. Ramanlal, L. M. Sander, and R. Ball, "Ballistic deposition on surfaces," *Physical Review A*, vol. 34, no. 6, p. 5091, 1986.

[122] E. Marinari, A. Pagnani, and G. Parisi, "Critical exponents of the kpz equation via multi-surface coding numerical simulations," *Journal of Physics A: Mathematical and General*, vol. 33, no. 46, p. 8181, 2000.

[123] L. Miettinen, M. Myllys, J. Merikoski, and J. Timonen, "Experimental determination of kpz height-fluctuation distributions," *The European Physical Journal B-Condensed Matter and Complex Systems*, vol. 46, pp. 55–60, 2005.

[124] U. C. Täuber, *Critical dynamics: a field theory approach to equilibrium and non-equilibrium scaling behavior*. New York, NY, US, Cambridge University Press, 2014.

[125] T. Ma and S. Wang, *Phase transition dynamics*. New York, NY, USA, Springer Science & Business Media, 2014.

[126] J. Cardy, *Scaling and renormalization in statistical physics*, vol. 5. New York, NY, USA, Cambridge University Press, 1996.

[127] D. J. Amit and V. Martin-Mayor, *Field theory, the renormalization group, and critical phenomena: graphs to computers*. Singapore, World Scientific Publishing Company, 2005.

[128] L. Onsager and S. Machlup, "Fluctuations and irreversible processes," *Physical Review*, vol. 91, no. 6, p. 1505, 1953.

[129] J. Hubbard, "Calculation of partition functions," *Physical Review Letters*, vol. 3, no. 2, p. 77, 1959.

[130] P. C. Martin, E. Siggia, and H. Rose, "Statistical dynamics of classical systems," *Physical Review A*, vol. 8, no. 1, p. 423, 1973.

[131] L. P. Kadanoff, "Scaling laws for ising models near t c," *Physics Physique Fizika*, vol. 2, no. 6, p. 263, 1966.

[132] M. Lässig, "On the renormalization of the kardar-parisi-zhang equation," *Nuclear Physics B*, vol. 448, no. 3, pp. 559–574, 1995.

[133] T. Sun and M. Plischke, "Renormalization group study of a driven continuum model for molecular beam epitaxy," *Physical Review Letters*, vol. 71, no. 19, p. 3174, 1993.

[134] I. Corwin, "The kardar–parisi–zhang equation and universality class," *Random Matrices: Theory and Applications*, vol. 1, no. 01, p. 1130001, 2012.

[135] K. Moser, J. Kertész, and D. E. Wolf, “Numerical solution of the kardar-parisi-zhang equation in one, two and three dimensions,” *Physica A: Statistical Mechanics and its Applications*, vol. 178, no. 2, pp. 215–226, 1991.

[136] M. Eden, “Proceedings of the fourth berkeley symposium on mathematical statistics and probability,” 1961.

[137] A. Barabasi, S. Buldyrev, S. Havlin, G. Huber, H. Stanley, and T. Vicsek, “Imbibition in porous media: experiment and theory,” *Nova Science, New York, 1992) p*, vol. 193, 1992.

[138] R. Bidaux and R. B. Pandey, “Driven diffusion of particles, first-passage front, and interface growth,” *Physical Review E*, vol. 48, no. 4, p. 2382, 1993.

[139] N. Martys, M. O. Robbins, and M. Cieplak, “Scaling relations for interface motion through disordered media: Application to two-dimensional fluid invasion,” *Physical Review B*, vol. 44, no. 22, p. 12294, 1991.

[140] C. Nolle, B. Koiller, N. Martys, and M. O. Robbins, “Morphology and dynamics of interfaces in random two-dimensional media,” *Physical Review Letters*, vol. 71, no. 13, p. 2074, 1993.

[141] J. Stokes, A. Kushnick, and M. O. Robbins, “Interface dynamics in porous media: A random-field description,” *Physical Review Letters*, vol. 60, no. 14, p. 1386, 1988.

[142] R. Jullien and R. Botet, “Scaling properties of the surface of the eden model in d= 2, 3, 4,” *Journal of Physics A: Mathematical and General*, vol. 18, no. 12, p. 2279, 1985.

[143] P. Meakin, R. Jullien, and R. Botet, “Large-scale numerical investigation of the surface of eden clusters,” *Europhysics Letters*, vol. 1, no. 12, p. 609, 1986.

[144] P. Freche, D. Stauffer, and H. Stanley, “Surface structure and anisotropy of eden clusters,” *Journal of Physics A: Mathematical and General*, vol. 18, no. 18, p. L1163, 1985.

[145] R. Hirsch and D. Wolf, "Anisotropy and scaling of eden clusters in two and three dimensions," *Journal of Physics A: Mathematical and General*, vol. 19, no. 5, p. L251, 1986.

[146] H. Kesten, *Percolation theory for mathematicians*, vol. 194. New York, NY, USA, Springer Science & Business Media, 1982.

[147] R. Jullien and R. Botet, "Surface thickness in the eden model," *Physical Review Letters*, vol. 54, no. 18, p. 2055, 1985.

[148] S. G. Alves, T. J. Oliveira, and S. C. Ferreira, "Universal fluctuations in radial growth models belonging to the kpz universality class," *Europhysics Letters*, vol. 96, no. 4, p. 48003, 2011.

[149] C. Wang, P. Liu, and J. Bassingthwaighte, "Off-lattice eden-c cluster growth model," *Journal of physics A: Mathematical and General*, vol. 28, no. 8, p. 2141, 1995.

[150] S. Ferreira and S. Alves, "Pitfalls in the determination of the universality class of radial clusters," *Journal of Statistical Mechanics: Theory and Experiment*, vol. 2006, no. 11, p. P11007, 2006.

[151] D. Wolf and J. Kertesz, "Surface width exponents for three-and four-dimensional eden growth," *Europhysics Letters*, vol. 4, no. 6, p. 651, 1987.

[152] J. Kertész and T. Vicsek, "Diffusion-limited aggregation and regular patterns: fluctuations versus anisotropy," *Journal of Physics A: Mathematical and General*, vol. 19, no. 5, p. L257, 1986.

[153] J. Nittmann and H. E. Stanley, "Tip splitting without interfacial tension and dendritic growth patterns arising from molecular anisotropy," *Nature*, vol. 321, no. 6071, pp. 663–668, 1986.

[154] J. Nittmann and H. E. Stanley, "Non-deterministic approach to anisotropic growth patterns with continuously tunable morphology: the fractal properties of some real snowflakes," *Journal of Physics A: Mathematical and General*, vol. 20, no. 17, p. L1185, 1987.

[155] J. Szép, J. Cserti, and J. Kertész, "Monte carlo approach to dendritic growth," *Journal of Physics A: Mathematical and General*, vol. 18, no. 8, p. L413, 1985.

[156] P. Šmilauer, M. R. Wilby, and D. D. Vvedensky, "Reentrant layer-by-layer growth: A numerical study," *Physical Review B*, vol. 47, no. 7, p. 4119, 1993.

[157] P. Tamborenea and S. D. Sarma, "Surface-diffusion-driven kinetic growth on one-dimensional substrates," *Physical Review E*, vol. 48, no. 4, p. 2575, 1993.

[158] M. Johnson, C. Orme, A. Hunt, D. Graff, J. Sudijono, L. Sander, and B. Orr, "Stable and unstable growth in molecular beam epitaxy," *Physical Review Letters*, vol. 72, no. 1, p. 116, 1994.

[159] S. Clarke and D. D. Vvedensky, "Origin of reflection high-energy electron-diffraction intensity oscillations during molecular-beam epitaxy: A computational modeling approach," *Physical Review Letters*, vol. 58, no. 21, p. 2235, 1987.

[160] S. D. Sarma, C. Lanczycki, S. Ghaisas, and J. Kim, "Defect formation and crossover behavior in the dynamic scaling properties of molecular-beam epitaxy," *Physical Review B*, vol. 49, no. 15, p. 10693, 1994.

[161] J. G. Amar, P.-M. Lam, and F. Family, "Groove instabilities in surface growth with diffusion," *Physical Review E*, vol. 47, no. 5, p. 3242, 1993.

[162] M. Plischke, J. D. Shore, M. Schroeder, M. Siegert, and D. E. Wolf, "Comment on "solid-on-solid rules and models for nonequilibrium growth in 2+ 1 dimensions"," *Physical Review Letters*, vol. 71, no. 15, p. 2509, 1993.

[163] M. Kotrla, A. Levi, and P. Šmilauer, “Roughness and nonlinearities in (2+ 1)-dimensional growth models with diffusion,” *Europhysics Letters*, vol. 20, no. 1, p. 25, 1992.

[164] P. Šmilauer and M. Kotrla, “Kinetic roughening in growth models with diffusion in higher dimensions,” *Europhysics Letters*, vol. 27, no. 4, p. 261, 1994.

[165] S. D. Sarma and S. Ghaisas, “Solid-on-solid rules and models for nonequilibrium growth in 2+ 1 dimensions,” *Physical Review Letters*, vol. 69, no. 26, p. 3762, 1992.

[166] L.-H. Tang and H. Leschhorn, “Pinning by directed percolation,” *Physical Review A*, vol. 45, no. 12, p. R8309, 1992.

[167] M. Patra, M. Karttunen, M. T. Hyvönen, E. Falck, P. Lindqvist, and I. Vattulainen, “Molecular dynamics simulations of lipid bilayers: major artifacts due to truncating electrostatic interactions,” *Biophysical Journal*, vol. 84, no. 6, pp. 3636–3645, 2003.

[168] A. Pérez, F. J. Luque, and M. Orozco, “Frontiers in molecular dynamics simulations of dna,” *Accounts of Chemical Research*, vol. 45, no. 2, pp. 196–205, 2012.

[169] J.-L. Barrat, J. Baschnagel, and A. Lyulin, “Molecular dynamics simulations of glassy polymers,” *Soft Matter*, vol. 6, no. 15, pp. 3430–3446, 2010.

[170] T. E. Cheatham III and P. A. Kollman, “Molecular dynamics simulation of nucleic acids,” *Annual Review of Physical Chemistry*, vol. 51, no. 1, pp. 435–471, 2000.

[171] M. Parrinello and A. Rahman, “Polymorphic transitions in single crystals: A new molecular dynamics method,” *Journal of Applied Physics*, vol. 52, no. 12, pp. 7182–7190, 1981.

[172] M. Parrinello and A. Rahman, “Crystal structure and pair potentials: A molecular-dynamics study,” *Physical Review Letters*, vol. 45, no. 14, p. 1196, 1980.

[173] J. Wong-Ekkabut and M. Karttunen, "The good, the bad and the user in soft matter simulations," *Biochimica et Biophysica Acta (BBA)-Biomembranes*, vol. 1858, no. 10, pp. 2529–2538, 2016.

[174] D. Frenkel and B. Smit, *Understanding molecular simulation: from algorithms to applications*, vol. 1. Amsterdam, NL, Elsevier, 2001.

[175] S. A. Hollingsworth and R. O. Dror, "Molecular dynamics simulation for all," *Neuron*, vol. 99, no. 6, pp. 1129–1143, 2018.

[176] E. Brini, E. A. Algaer, P. Ganguly, C. Li, F. Rodríguez-Ropero, and N. F. van der Vegt, "Systematic coarse-graining methods for soft matter simulations–a review," *Soft Matter*, vol. 9, no. 7, pp. 2108–2119, 2013.

[177] D. C. Rapaport and D. C. R. Rapaport, *The art of molecular dynamics simulation*. Cambridge, UK, Cambridge University Press, 2004.

[178] S. O. Nielsen, C. F. Lopez, G. Srinivas, and M. L. Klein, "Coarse grain models and the computer simulation of soft materials," *Journal of Physics: Condensed Matter*, vol. 16, no. 15, p. R481, 2004.

[179] B. G. Godard and C.-P. Heisenberg, "Cell division and tissue mechanics," *Current Opinion in Cell Biology*, vol. 60, pp. 114–120, 2019.

[180] R. G. Wells, "Tissue mechanics and fibrosis," *Biochimica et Biophysica Acta (BBA)-Molecular Basis of Disease*, vol. 1832, no. 7, pp. 884–890, 2013.

[181] C. Frantz, K. M. Stewart, and V. M. Weaver, "The extracellular matrix at a glance," *Journal of Cell Science*, vol. 123, no. 24, pp. 4195–4200, 2010.

[182] E. Moeendarbary and A. R. Harris, "Cell mechanics: principles, practices, and prospects," *Wiley Interdisciplinary Reviews: Systems Biology and Medicine*, vol. 6, no. 5, pp. 371–388, 2014.

[183] L. Petruzzelli, M. Takami, and H. D. Humes, “Structure and function of cell adhesion molecules,” *The American Journal of Medicine*, vol. 106, no. 4, pp. 467–476, 1999.

[184] C. G. dos Remedios and P. D. Moens, “Actin and the actomyosin interface: a review,” *Biochimica et Biophysica Acta (BBA)-Bioenergetics*, vol. 1228, no. 2-3, pp. 99–124, 1995.

[185] G. M. Edelman, “Cell adhesion molecules,” *Science*, vol. 219, no. 4584, pp. 450–457, 1983.

[186] F. M. Watt and H. Fujiwara, “Cell-extracellular matrix interactions in normal and diseased skin,” *Cold Spring Harbor Perspectives in Biology*, vol. 3, no. 4, p. a005124, 2011.

[187] A. Elosegui-Artola, “The extracellular matrix viscoelasticity as a regulator of cell and tissue dynamics,” *Current Opinion in Cell Biology*, vol. 72, pp. 10–18, 2021.

[188] O. Chaudhuri, J. Cooper-White, P. A. Janmey, D. J. Mooney, and V. B. Shenoy, “Effects of extracellular matrix viscoelasticity on cellular behaviour,” *Nature*, vol. 584, no. 7822, pp. 535–546, 2020.

[189] E. Evans and R. Hochmuth, “Membrane viscoelasticity,” *Biophysical Journal*, vol. 16, no. 1, pp. 1–11, 1976.

[190] P. Kunda, A. E. Pelling, T. Liu, and B. Baum, “Moesin controls cortical rigidity, cell rounding, and spindle morphogenesis during mitosis,” *Current Biology*, vol. 18, no. 2, pp. 91–101, 2008.

[191] P. Kunda and B. Baum, “The actin cytoskeleton in spindle assembly and positioning,” *Trends in Cell Biology*, vol. 19, no. 4, pp. 174–179, 2009.

[192] S. Carreno, I. Kouranti, E. S. Glusman, M. T. Fuller, A. Echard, and F. Payre, "Moesin and its activating kinase slik are required for cortical stability and microtubule organization in mitotic cells," *The Journal of Cell Biology*, vol. 180, no. 4, pp. 739–746, 2008.

[193] M. P. Stewart, J. Helenius, Y. Toyoda, S. P. Ramanathan, D. J. Muller, and A. A. Hyman, "Hydrostatic pressure and the actomyosin cortex drive mitotic cell rounding," *Nature*, vol. 469, no. 7329, pp. 226–230, 2011.

[194] S. W. Tait, G. Ichim, and D. R. Green, "Die another way–non-apoptotic mechanisms of cell death," *Journal of Cell Science*, vol. 127, no. 10, pp. 2135–2144, 2014.

[195] L. Galluzzi, I. Vitale, S. A. Aaronson, J. M. Abrams, D. Adam, P. Agostinis, E. S. Alnemri, L. Altucci, I. Amelio, D. W. Andrews, *et al.*, "Molecular mechanisms of cell death: recommendations of the nomenclature committee on cell death 2018," *Cell Death & Differentiation*, vol. 25, no. 3, pp. 486–541, 2018.

[196] C. D. Bortner and J. A. Cidlowski, "A necessary role for cell shrinkage in apoptosis," *Biochemical Pharmacology*, vol. 56, no. 12, pp. 1549–1559, 1998.

[197] D. Tomanek and N. Frederick, "Carbon fullerenes," *Retrieved From*, vol. 205, 2015.

[198] A. H. Francis, "An atlas of fullerenes by pw fowler (university of exeter), de manolopoulos (university of nottingham). oxford: New york. 1995. viii+ 392 pp. 98.00. isbn 0-19-855787-6.," 1996.

[199] H. Wadell, "Volume, shape, and roundness of quartz particles," *The Journal of Geology*, vol. 43, no. 3, pp. 250–280, 1935.

[200] C. Roubinet, P. T. Tran, and M. Piel, "Common mechanisms regulating cell cortex properties during cell division and cell migration," *Cytoskeleton*, vol. 69, no. 11, pp. 957–972, 2012.

[201] T. Strangeways, “Observations on the changes seen in living cells during growth and division,” *Proceedings of the Royal Society of London. Series B, Containing Papers of a Biological Character*, vol. 94, no. 658, pp. 137–141, 1922.

[202] L. P. Cramer and T. J. Mitchison, “Investigation of the mechanism of retraction of the cell margin and rearward flow of nodules during mitotic cell rounding.,” *Molecular Biology of the Cell*, vol. 8, no. 1, pp. 109–119, 1997.

[203] A. D. Theocharis, S. S. Skandalis, C. Gialeli, and N. K. Karamanos, “Extracellular matrix structure,” *Advanced Drug Delivery Reviews*, vol. 97, pp. 4–27, 2016.

[204] J. D. Humphrey, E. R. Dufresne, and M. A. Schwartz, “Mechanotransduction and extracellular matrix homeostasis,” *Nature Reviews Molecular Cell Biology*, vol. 15, no. 12, pp. 802–812, 2014.

[205] Z. Jahed, H. Shams, M. Mehrbod, and M. R. Mofrad, “Mechanotransduction pathways linking the extracellular matrix to the nucleus,” *International Review of Cell and Molecular Biology*, vol. 310, pp. 171–220, 2014.

[206] K. Jansen, P. Atherton, and C. Ballestrem, “Mechanotransduction at the cell-matrix interface,” in *Seminars in cell & Developmental Biology*, vol. 71, pp. 75–83, Elsevier, 2017.

[207] C. Cadart, E. Zlotek-Zlotkiewicz, M. Le Berre, M. Piel, and H. K. Matthews, “Exploring the function of cell shape and size during mitosis,” *Developmental Cell*, vol. 29, no. 2, pp. 159–169, 2014.

[208] J. C. Canman, L. A. Cameron, P. S. Maddox, A. Straight, J. S. Tirnauer, T. J. Mitchison, G. Fang, T. M. Kapoor, and E. Salmon, “Determining the position of the cell division plane,” *Nature*, vol. 424, no. 6952, pp. 1074–1078, 2003.

[209] E. Caussinus and C. Gonzalez, “Induction of tumor growth by altered stem-cell asymmetric division in drosophila melanogaster,” *Nature Genetics*, vol. 37, no. 10, pp. 1125–1129, 2005.

[210] C. Chen, J. M. Fingerhut, and Y. M. Yamashita, “The ins (ide) and outs (ide) of asymmetric stem cell division,” *Current Opinion in Cell Biology*, vol. 43, pp. 1–6, 2016.

[211] S. J. Morrison and J. Kimble, “Asymmetric and symmetric stem-cell divisions in development and cancer,” *Nature*, vol. 441, no. 7097, pp. 1068–1074, 2006.

[212] R. A. Green, E. Paluch, and K. Oegema, “Cytokinesis in animal cells,” *Annual review of cell and developmental biology*, vol. 28, pp. 29–58, 2012.

[213] L. J. Pillitteri, D. B. Sloan, N. L. Bogenschutz, and K. U. Torii, “Termination of asymmetric cell division and differentiation of stomata,” *Nature*, vol. 445, no. 7127, pp. 501–505, 2007.

[214] F. Bosveld, O. Markova, B. Guirao, C. Martin, Z. Wang, A. Pierre, M. Balakireva, I. Gaugue, A. Ainslie, N. Christophorou, *et al.*, “Epithelial tricellular junctions act as interphase cell shape sensors to orient mitosis,” *Nature*, vol. 530, no. 7591, pp. 495–498, 2016.

[215] P. Sahlin and H. Jönsson, “A modeling study on how cell division affects properties of epithelial tissues under isotropic growth,” *PloS One*, vol. 5, no. 7, p. e11750, 2010.

[216] P. Madhikar, *Molecular dynamics modelling of the mechanics of cells*. PhD thesis, Eindhoven University of Technology, 2019.

[217] J. F. Kerr, “A histochemical study of hypertrophy and ischaemic injury of rat liver with special reference to changes in lysosomes,” *The Journal of Pathology and Bacteriology*, vol. 90, no. 2, pp. 419–435, 1965.

[218] M. G. O'Rourke and K. A. Ellem, "John kerr and apoptosis," *Medical Journal of Australia*, vol. 173, no. 11-12, pp. 616–617, 2000.

[219] S. Raychaudhuri, "A minimal model of signaling network elucidates cell-to-cell stochastic variability in apoptosis," *PloS One*, vol. 5, no. 8, p. e11930, 2010.

[220] "Gnu general public license, version 2." `https://www.gnu.org/licenses/old-licenses/gpl-2.0.en.html`.

[221] NVIDIA, "Cuda toolkit documentation." `https://docs.nvidia.com/cuda/index.html`.

[222] T. Murtola, A. Bunker, I. Vattulainen, M. Deserno, and M. Karttunen, "Multiscale modeling of emergent materials: biological and soft matter," *Physical Chemistry Chemical Physics*, vol. 11, no. 12, pp. 1869–1892, 2009.

[223] R. D. Groot and P. B. Warren, "Dissipative particle dynamics: Bridging the gap between atomistic and mesoscopic simulation," *The Journal of Chemical Physics*, vol. 107, no. 11, pp. 4423–4435, 1997.

[224] G. Besold, I. Vattulainen, M. Karttunen, and J. M. Polson, "Towards better integrators for dissipative particle dynamics simulations," *Physical Review E*, vol. 62, no. 6, p. R7611, 2000.

[225] K. E. Novik and P. V. Coveney, "Finite-difference methods for simulation models incorporating nonconservative forces," *The Journal of Chemical Physics*, vol. 109, no. 18, pp. 7667–7677, 1998.

[226] J. Gibson, K. Chen, and S. Chynoweth, "The equilibrium of a velocity-verlet type algorithm for dpd with finite time steps," *International Journal of Modern Physics C*, vol. 10, no. 01, pp. 241–261, 1999.

[227] I. Pagonabarraga, M. Hagen, and D. Frenkel, “Self-consistent dissipative particle dynamics algorithm,” *Europhysics Letters*, vol. 42, no. 4, p. 377, 1998.

[228] I. Vattulainen, M. Karttunen, G. Besold, and J. M. Polson, “Integration schemes for dissipative particle dynamics simulations: From softly interacting systems towards hybrid models,” *The Journal of Chemical Physics*, vol. 116, no. 10, pp. 3967–3979, 2002.

[229] W. K. den Otter and J. Clarke, “A new algorithm for dissipative particle dynamics,” *Europhysics Letters*, vol. 53, no. 4, p. 426, 2001.

[230] T. Shardlow, “Splitting for dissipative particle dynamics,” *SIAM Journal on Scientific Computing*, vol. 24, no. 4, pp. 1267–1282, 2003.

[231] A. Johnson, J. Lewis, and B. ALBERTS, *Molecular biology of the cell.* New York, NY, USA, Garland Science, 2002.

[232] A. Lees and S. Edwards, “The computer study of transport processes under extreme conditions,” *Journal of Physics C: Solid State Physics*, vol. 5, no. 15, p. 1921, 1972.

[233] A. J. Wagner and I. Pagonabarraga, “Lees–edwards boundary conditions for lattice boltzmann,” *Journal of Statistical Physics*, vol. 107, no. 1, pp. 521–537, 2002.

[234] J. Glaser, T. D. Nguyen, J. A. Anderson, P. Lui, F. Spiga, J. A. Millan, D. C. Morse, and S. C. Glotzer, “Strong scaling of general-purpose molecular dynamics simulations on gpus,” *Computer Physics Communications*, vol. 192, pp. 97–107, 2015.

[235] Y.-L. Zhu, D. Pan, Z.-W. Li, H. Liu, H.-J. Qian, Y. Zhao, Z.-Y. Lu, and Z.-Y. Sun, “Employing multi-gpu power for molecular dynamics simulation: an extension of galamost,” *Molecular Physics*, vol. 116, no. 7-8, pp. 1065–1077, 2018.

[236] NVIDIA, “Remote direct memory access over converged ethernet documentation.” `https://www.ibm.com/docs/en/zos/2.4.0?topic=access-remote-direct-memory-over-converged-ethernet`.

[237] H. W. Jones Jr, “Record of the first physician to see henrietta lacks at the johns hopkins hospital: history of the beginning of the hela cell line,” *American Journal of Obstetrics and Gynecology*, vol. 176, no. 6, pp. s227–s228, 1997.

[238] L. Zhao, C. Kroenke, J. Song, D. Piwnica-Worms, J. Ackerman, and J. Neil, “Intracellular water-specific mr of microbead-adherent cells: the hela cell intracellular water exchange lifetime,” *NMR in Biomedicine*, vol. 21, no. 2, pp. 159–164, 2008.

[239] R. Milo, P. Jorgensen, U. Moran, G. Weber, and M. Springer, “Bionumbers—the database of key numbers in molecular and cell biology,” *Nucleic Acids Research*, vol. 38, no. suppl_1, pp. D750–D753, 2010.

[240] K. Park, J. Jang, D. Irimia, J. Sturgis, J. Lee, J. P. Robinson, M. Toner, and R. Bashir, “‘living cantilever arrays’ for characterization of mass of single live cells in fluids,” *Lab on a Chip*, vol. 8, no. 7, pp. 1034–1041, 2008.

[241] V. E. Foe and B. M. Alberts, “Studies of nuclear and cytoplasmic behaviour during the five mitotic cycles that precede gastrulation in drosophila embryogenesis,” *Journal of Cell Science*, vol. 61, no. 1, pp. 31–70, 1983.

[242] I. L. Cameron and R. C. Greulich, “Evidence for an essentially constant duration of dna synthesis in renewing epithelia of the adult mouse,” *The Journal of Cell Biology*, vol. 18, no. 1, pp. 31–40, 1963.

[243] O. Wartlick, P. Mumcu, A. Kicheva, T. Bittig, C. Seum, F. Jülicher, and M. Gonzalez-Gaitan, “Dynamics of dpp signaling and proliferation control,” *Science*, vol. 331, no. 6021, pp. 1154–1159, 2011.

[244] T. Lecuit and L. Le Goff, “Orchestrating size and shape during morphogenesis,” *Nature*, vol. 450, no. 7167, pp. 189–192, 2007.

[245] F. Costa, M. Campos, and M. da Silva, "The universal growth rate behavior and regime transition in adherent cell colonies," *Journal of Theoretical Biology*, vol. 387, pp. 181–188, 2015.

[246] J. Li, S. K. Schnyder, M. S. Turner, and R. Yamamoto, "Role of the cell cycle in collective cell dynamics," *Physical Review X*, vol. 11, no. 3, p. 031025, 2021.

[247] E. Khain and J. Straetmans, "Dynamics of an expanding cell monolayer," *Journal of Statistical Physics*, vol. 184, no. 2, pp. 1–13, 2021.

[248] A. Brú, S. Albertos, J. L. Subiza, J. L. Garcia-Asenjo, and I. Brú, "Reply to comments by Buceta and Galeano regarding the article "The Universal Dynamics of Tumor Growth"," *Biophysical Journal*, vol. 88, no. 5, pp. 3737–3738, 2005.

[249] M. Kardar, G. Parisi, and Y.-C. Zhang, "Dynamic scaling of growing interfaces," *Phys. Rev. Lett.*, vol. 56, no. 9, p. 889, 1986.

[250] D. A. Kessler, H. Levine, and L. M. Sander, "Molecular-beam epitaxial growth and surface diffusion," *Physical Review Letters*, vol. 69, no. 1, p. 100, 1992.

[251] S. D. Sarma, S. Ghaisas, and J. Kim, "Kinetic super-roughening and anomalous dynamic scaling in nonequilibrium growth models," *Physical Review E*, vol. 49, no. 1, p. 122, 1994.

[252] F. T. Hoyos, R. B. Navarro, J. V. Villadiego, and M. Guerrero-Martelo, "Geometrical study of astrocytomas through fractals and scaling analysis," *Applied Radiation and Isotopes*, vol. 141, pp. 250–256, 2018.

[253] J. Galeano, J. Buceta, K. Juarez, B. Pumarino, J. De La Torre, and J. Iriondo, "Dynamical scaling analysis of plant callus growth," *Europhysics Letters*, vol. 63, no. 1, p. 83, 2003.

[254] S. N. Santalla, J. Rodríguez-Laguna, J. P. Abad, I. Marín, M. del Mar Espinosa, J. Muñoz-García, L. Vázquez, and R. Cuerno, "Nonuniversality of front fluctuations for compact colonies of nonmotile bacteria," *Physical Review E*, vol. 98, no. 1, p. 012407, 2018.

[255] T. Vicsek, M. Cserző, and V. K. Horváth, "Self-affine growth of bacterial colonies," *Physica A*, vol. 167, no. 2, pp. 315–321, 1990.

[256] J. A. Bonachela, C. D. Nadell, J. B. Xavier, and S. A. Levin, "Universality in bacterial colonies," *Journal of Statistical Physics*, vol. 144, no. 2, pp. 303–315, 2011.

[257] A. Buttenschön and L. Edelstein-Keshet, "Bridging from single to collective cell migration: A review of models and links to experiments," *PLOS Computational Biology*, vol. 16, no. 12, p. e1008411, 2020.

[258] P. Madhikar, J. Åström, J. Westerholm, B. Baumeier, and M. Karttunen, "Coarse-grained modeling of cell division in 3d: influence of density, medium viscosity, and inter-membrane friction on cell growth and nearest neighbor distribution," *Soft Materials*, vol. 18, no. 2-3, pp. 150–162, 2020.

[259] P. Madhikar, J. Åström, B. Baumeier, and M. Karttunen, "Jamming and force distribution in growing epithelial tissue," *Physical Review Research*, vol. 3, no. 2, p. 023129, 2021.

[260] M. Plischke and Z. Rácz, "Dynamic scaling and the surface structure of eden clusters," *Physical Review A*, vol. 32, no. 6, p. 3825, 1985.

[261] D. Liu and M. Plischke, "Universality in two-and three-dimensional growth and deposition models," *Physical Review B*, vol. 38, no. 7, p. 4781, 1988.

[262] A. K. Laird, "Dynamics of tumour growth," *British Journal of Cancer*, vol. 18, no. 3, p. 490, 1964.

[263] D. G. Drubin and W. J. Nelson, “Origins of cell polarity,” *Cell*, vol. 84, no. 3, pp. 335–344, 1996.

[264] M. T. Butler and J. B. Wallingford, “Planar cell polarity in development and disease,” *Nature Reviews Molecular Cell Biology*, vol. 18, no. 6, pp. 375–388, 2017.

[265] J. P. Campanale, T. Y. Sun, and D. J. Montell, “Development and dynamics of cell polarity at a glance,” *Journal of Cell Science*, vol. 130, no. 7, pp. 1201–1207, 2017.

[266] F. van Roy and G. Berx, “The cell-cell adhesion molecule E-cadherin.,” *Cellular and Molecular Life Sciences*, vol. 65, pp. 3756–3788, 2008.

[267] M. P. Stemmler, “Cadherins in development and cancer,” *Molecular BioSystems*, vol. 4, no. 8, pp. 835–850, 2008.

[268] C. D. Buckley, G. E. Rainger, P. F. Bradfield, G. B. Nash, and D. L. Simmons, “Cell adhesion: More than just glue (review),” *Molecular Membrane Biology*, vol. 15, no. 4, pp. 167–176, 1998 Oct-Dec.

[269] G. M. Edelman and K. L. Crossin, “Cell Adhesion Molecules: Implications for a Molecular Histology,” *Annual Review of Biochemistry*, vol. 60, pp. 155–190, 1991.

[270] D. K. Schluter, I. Ramis-Conde, and M. A. J. Chaplain, “Multi-scale modelling of the dynamics of cell colonies: insights into cell-adhesion forces and cancer invasion from in silico simulations,” *Journal of the Royal Society Interface*, vol. 12, no. 103, pp. 20141080–20141080, 2014.

[271] S. van Helvert, C. Storm, and P. Friedl, “Mechanoreciprocity in cell migration,” *Nature Cell Biology*, vol. 20, no. 1, pp. 8–20, 2017.

[272] A. Mkrtchyan, *A Single Cell Based Model for Cell Divisions with Spontaneous Topology Changes*. PhD thesis, University of Western Ontario, 2013.

[273] J. Kimble and S. L. Crittenden, "Germline proliferation and its control," *WormBook: The Online Review of C. elegans Biology [Internet]*, 2005.

[274] Y. Imoto, Y. Yoshida, F. Yagisawa, H. Kuroiwa, and T. Kuroiwa, "The cell cycle, including the mitotic cycle and organelle division cycles, as revealed by cytological observations," *Journal of Electron Microscopy*, vol. 60, no. suppl_1, pp. S117–S136, 2011.

[275] T. H. Group, "Hierarchical Data Format, version 5." http://www.hdfgroup.org/HDF5/, 1997.

[276] P. Nikunen, M. Karttunen, and I. Vattulainen, "How would you integrate the equations of motion in dissipative particle dynamics simulations?," *Computer Physics Communications*, vol. 153, no. 3, pp. 407–423, 2003.

[277] A. Rohatgi, "Webplotdigitizer: Version 4.5," 2021.

[278] H. K. Kleinman, D. Philp, and M. P. Hoffman, "Role of the extracellular matrix in morphogenesis," *Current Opinion in Biotechnology*, vol. 14, no. 5, pp. 526–532, 2003.

[279] G. Rapin, N. Caballero, I. Gaponenko, B. Ziegler, A. Rawleigh, E. Moriggi, T. Giamarchi, S. A. Brown, and P. Paruch, "Roughness and dynamics of proliferating cell fronts as a probe of cell–cell interactions," *Scientific Reports*, vol. 11, no. 1, pp. 1–9, 2021.

[280] I. Pastushenko, A. Brisebarre, A. Sifrim, M. Fioramonti, T. Revenco, S. Boumahdi, A. Van Keymeulen, D. Brown, V. Moers, S. Lemaire, S. De Clercq, E. Minguijón, C. Balsat, Y. Sokolow, C. Dubois, F. De Cock, S. Scozzaro, F. Sopena, A. Lanas, N. D'Haene, I. Salmon, J.-C. Marine, T. Voet, P. A. Sotiropoulou, and C. Blanpain, "Identification of the tumour transition states occurring during EMT," *Nature*, vol. 556, pp. 463–468, Apr. 2018.

[281] G. Ventura and J. Sedzinski, “Emerging concepts on the mechanical interplay between migrating cells and microenvironment in vivo,” *Frontiers in Cell and Developmental Biology*, vol. 10, p. 961460, 2022.

[282] I. M. Wortel and J. Textor, “Artistoo, a library to build, share, and explore simulations of cells and tissues in the web browser,” *Elife*, vol. 10, p. e61288, 2021.

[283] R. Conradin, C. Coreixas, J. Latt, and B. Chopard, “Palacell2d: A framework for detailed tissue morphogenesis,” *Journal of Computational Science*, vol. 53, p. 101353, 2021.

[284] A. Larkin and Y. N. Ovchinnikov, “Pinning in type II superconductors,” *Journal of Low Temperature Physics*, vol. 34, no. 3, pp. 409–428, 1979.

[285] L. Balents and M. P. Fisher, “Temporal order in dirty driven periodic media,” *Physical Review Letters*, vol. 75, no. 23, p. 4270, 1995.

[286] M. Karttunen, M. Haataja, K. R. Elder, and M. Grant, “Defects, order, and hysteresis in driven charge-density waves,” *Physical Review Letters*, vol. 83, no. 17, pp. 3518–3521, 1999.

[287] J. Bouchaud, E. Bouchaud, G. Lapasset, and J. Planes, “Models of fractal cracks,” *Physical Review Letters*, vol. 71, no. 14, p. 2240, 1993.

[288] D. S. Fisher, “Threshold behavior of charge-density waves pinned by impurities,” *Physical Review Letters*, vol. 50, no. 19, pp. 1486–1489, 1983.

[289] Z. Csahók, K. Honda, E. Somfai, M. Vicsek, and T. Vicsek, “Dynamics of surface roughening in disordered media,” *Physica A*, vol. 200, no. 1-4, pp. 136–154, 1993.

[290] S. Buldyrev, A.-L. Barabási, F. Caserta, S. Havlin, H. Stanley, and T. Vicsek, “Anomalous interface roughening in porous media: Experiment and model,” *Physical Review A*, vol. 45, no. 12, p. R8313, 1992.

[291] K. Sneppen, “Self-organized pinning and interface growth in a random medium,” *Physical Review Letters*, vol. 69, no. 24, p. 3539, 1992.

[292] H. Leschhorn, “Anisotropic interface depinning: Numerical results,” *Physical Review E*, vol. 54, no. 2, p. 1313, 1996.

[293] E. Young, G. Melaugh, and R. J. Allen, “Pinning transition in biofilm structure driven by active layer dynamics,” *bioRxiv*, p. 2022.03.21.485164, 2022.

[294] X. Wang, H. A. Stone, and R. Golestanian, “Shape of the growing front of biofilms,” *New Journal of Physics*, vol. 19, no. 12, p. 125007, 2017.

[295] D. Bi, X. Yang, M. C. Marchetti, and M. L. Manning, “Motility-driven glass and jamming transitions in biological tissues,” *Physical Review X*, vol. 6, no. 2, p. 021011, 2016.

[296] D. E. P. Pinto, M. M. T. da Gama, and N. A. M. Araújo, “Cell motility in confluent tissues induced by substrate disorder,” *Physical Review Research*, vol. 4, no. 2, p. 023186, 2022.

[297] “Open source software at https://github.com/softsimu/cellsim3d.”

[298] M. Schroeder, M. Siegert, D. Wolf, J. Shore, and M. Plischke, “Scaling of growing surfaces with large local slopes,” *Europhysics Letters*, vol. 24, no. 7, p. 563, 1993.

[299] J. M. López, M. A. Rodriguez, and R. Cuerno, “Superroughening versus intrinsic anomalous scaling of surfaces,” *Physical Review E*, vol. 56, no. 4, p. 3993, 1997.

[300] J. Krug, “Turbulent interfaces,” *Physical Review Letters*, vol. 72, no. 18, p. 2907, 1994.

[301] J. M. López and M. A. Rodríguez, “Lack of self-affinity and anomalous roughening in growth processes,” *Physical Review E*, vol. 54, no. 3, p. R2189, 1996.

[302] S. D. Sarma, C. Lanczycki, R. Kotlyar, and S. Ghaisas, “Scale invariance and dynamical correlations in growth models of molecular beam epitaxy,” *Physical Review E*, vol. 53, no. 1, p. 359, 1996.

[303] H. Yang, G. Wang, and T. Lu, “Instability in low-temperature molecular-beam epitaxy growth of si/si (111),” *Physical Review Letters*, vol. 73, no. 17, p. 2348, 1994.

[304] J. M. Lopez and J. Schmittbuhl, “Anomalous scaling of fracture surfaces,” *Physical Review E*, vol. 57, no. 6, p. 6405, 1998.

[305] J. J. Ramasco, J. M. López, and M. A. Rodríguez, “Generic dynamic scaling in kinetic roughening,” *Physical Review Letters*, vol. 84, no. 10, p. 2199, 2000.

[306] T. Witten Jr and L. M. Sander, “Diffusion-limited aggregation, a kinetic critical phenomenon,” *Physical Review Letters*, vol. 47, no. 19, p. 1400, 1981.

[307] P. Meakin, “Diffusion-controlled cluster formation in 2—6-dimensional space,” *Physical Review A*, vol. 27, no. 3, p. 1495, 1983.

[308] E. Ben-Jacob, O. Shochet, A. Tenenbaum, I. Cohen, A. Czirók, and T. Vicsek, “Communication, regulation and control during complex patterning of bacterial colonies,” *Fractals*, vol. 2, no. 01, pp. 15–44, 1994.

[309] H. Fujikawa and M. Matsushita, “Fractal growth of bacillus subtilis on agar plates,” *Journal of the Physical Society of Japan*, vol. 58, no. 11, pp. 3875–3878, 1989.

[310] M. Matsushita and H. Fujikawa, “Diffusion-limited growth in bacterial colony formation,” *Physica A*, vol. 168, no. 1, pp. 498–506, 1990.

[311] N. E. Muzzio, M. A. Pasquale, M. A. C. Huergo, A. E. Bolzán, P. H. González, and A. J. Arvia, “Spatio-temporal morphology changes in and quenching effects on the 2d spreading dynamics of cell colonies in both plain and methylcellulose-containing culture media,” *Journal of Biological Physics*, vol. 42, no. 3, pp. 477–502, 2016.

[312] Y. N. Jan and L. Y. Jan, “Asymmetric cell division,” *Nature*, vol. 392, no. 6678, pp. 775–778, 1998.

[313] E. Ben-Jacob, O. Shochet, A. Tenenbaum, I. Cohen, A. Czirók, and T. Vicsek, “Communication, regulation and control during complex patterning of bacterial colonies,” *Fractals*, vol. 2, no. 01, pp. 15–44, 1994.

[314] E. Murray, “A two-dimensional growth process,” in *Proceedings of the Fourth Berkeley Symposium on Mathematical Statistics and Probability: Held at the Statistical Laboratory, University of California, June 20-July 30, 1960*, vol. 2, (Berkeley, CA), p. 223, 1960.

[315] S. Ferreira Jr, M. Martins, and M. Vilela, “Reaction-diffusion model for the growth of avascular tumor,” *Physical Review E*, vol. 65, no. 2, p. 021907, 2002.

[316] J. A. Sherratt and M. A. Chaplain, “A new mathematical model for avascular tumour growth,” *Journal of Mathematical Biology*, vol. 43, no. 4, pp. 291–312, 2001.

[317] S. Besson and J. Dumais, “Universal rule for the symmetric division of plant cells,” *Proceedings of the National Academy of Sciences*, vol. 108, no. 15, pp. 6294–6299, 2011.

[318] M. Louveaux, J.-D. Julien, V. Mirabet, A. Boudaoud, and O. Hamant, “Cell division plane orientation based on tensile stress in arabidopsis thaliana,” *Proceedings of the National Academy of Sciences*, vol. 113, no. 30, pp. E4294–E4303, 2016.

[319] A. Huttenlocher, “Cell polarization mechanisms during directed cell migration,” *Nature Cell Biology*, vol. 7, no. 4, pp. 336–337, 2005.

[320] Y. M. Elkouby and M. C. Mullins, “Coordination of cellular differentiation, polarity, mitosis and meiosis–new findings from early vertebrate oogenesis,” *Developmental Biology*, vol. 430, no. 2, pp. 275–287, 2017.

[321] Y.-N. Jan and L. Y. Jan, “Polarity in cell division: what frames thy fearful asymmetry?,” *Cell*, vol. 100, no. 6, pp. 599–602, 2000.

[322] K. Matsushita, “Cell-alignment patterns in the collective migration of cells with polarized adhesion,” *Physical Review E*, vol. 95, no. 3, p. 032415, 2017.

[323] M. Springer, “Memory-efficient object-oriented programming on gpus,” *arXiv preprint arXiv:1908.05845*, 2019.

[324] M. Springer and H. Masuhara, “Ikra-cpp: A c++/cuda dsl for object-oriented programming with structure-of-arrays layout,” in *Proceedings of the 2018 4th Workshop on Programming Models for SIMD/Vector Processing*, pp. 1–9, 2018.

Curriculum Vitae

Name:	Mahmood Mazarei
Post-Secondary Education and Degrees:	Sharif University of Technology Tehran, Iran 2008 - 2013 B.Sc., of Theoretical Physics
	Sharif University of Technology Tehran, Iran 2013 - 2015, M.Sc. of Theoretical Physics
	University of Western Ontario London, Canada 2019 - 2023 , Ph.D. of Theoretical Physics
Related Work Experience:	Teaching Assistant and Research Assistant The University of Western Ontario 2019 - 2023

Publications:

- Mazarei, M., Åström, J., Westerholm, J. and Karttunen, M., In silico testing of the universality of epithelial tissue growth. Physical Review E, 106(6), p.L062402, 2022.
- Rings, T., Mazarei, M., Akhshi, A., Geier, C., Tabar, M.R.R. and Lehnertz, K., Traceability and dynamical resistance of precursor of extreme events. Scientific reports, 9(1), p.1744, 2019.
- Hedayatifar, L., Irani, E., Mazarei, M., Rasti, S., Azar, Y.T., Rezakhani, A.T., Mashaghi,

A., Shayeganfar, F., Anvari, M., Heydari, T. and Tabar, A.R., Optical absorption and electronic spectra of chlorophylls a and b. RSC advances, 6(111), pp.109778-109785, 2016.